Study on functionalization and cytotoxicity of calcium and potassium ferrite nanoparticles

A THESIS

Submitted to the

FACULTY OF SCIENCE

THAPAR UNIVERSITY, PATIALA

for the degree of

Doctor of Philosophy

By

Lavanya Khanna

Regn. No. 900912025

School of Physics & Materials Science

Thapar University

Patiala - 147 004

INDIA

June 2014

DECLARATION

It is certified that the thesis is entirely my own and that the ideas and references cited herein have been duly acknowledged.

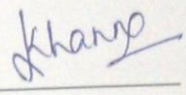

(Lavanya Khanna)

Attestation by supervisor

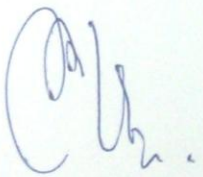

(Dr. N. K. Verma)

Senior Professor

School of Physics and Materials Science,

Thapar University,

Patiala – 147 004

India

CERTIFICATE

This is to certify that the thesis entitled, "**Study on functionalization and cytotoxicity of calcium and potassium ferrite nanoparticles**", submitted by **Ms. Lavanya Khanna** in the fulfillment of the requirement for the award of the degree of Doctor of Philosophy in the School of Physics and Materials Science, Thapar University, Patiala, is a record of candidate's own work carried out by her under my supervision and guidance. The matter presented in this thesis has not been submitted in part or full for the award of any degree in any other University or Institute.

Attestation by supervisor

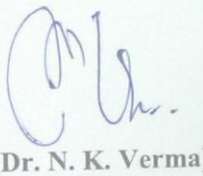

(Dr. N. K. Verma)

Senior Professor

School of Physics and Materials Science,

Thapar University,

Patiala – 147 004

India

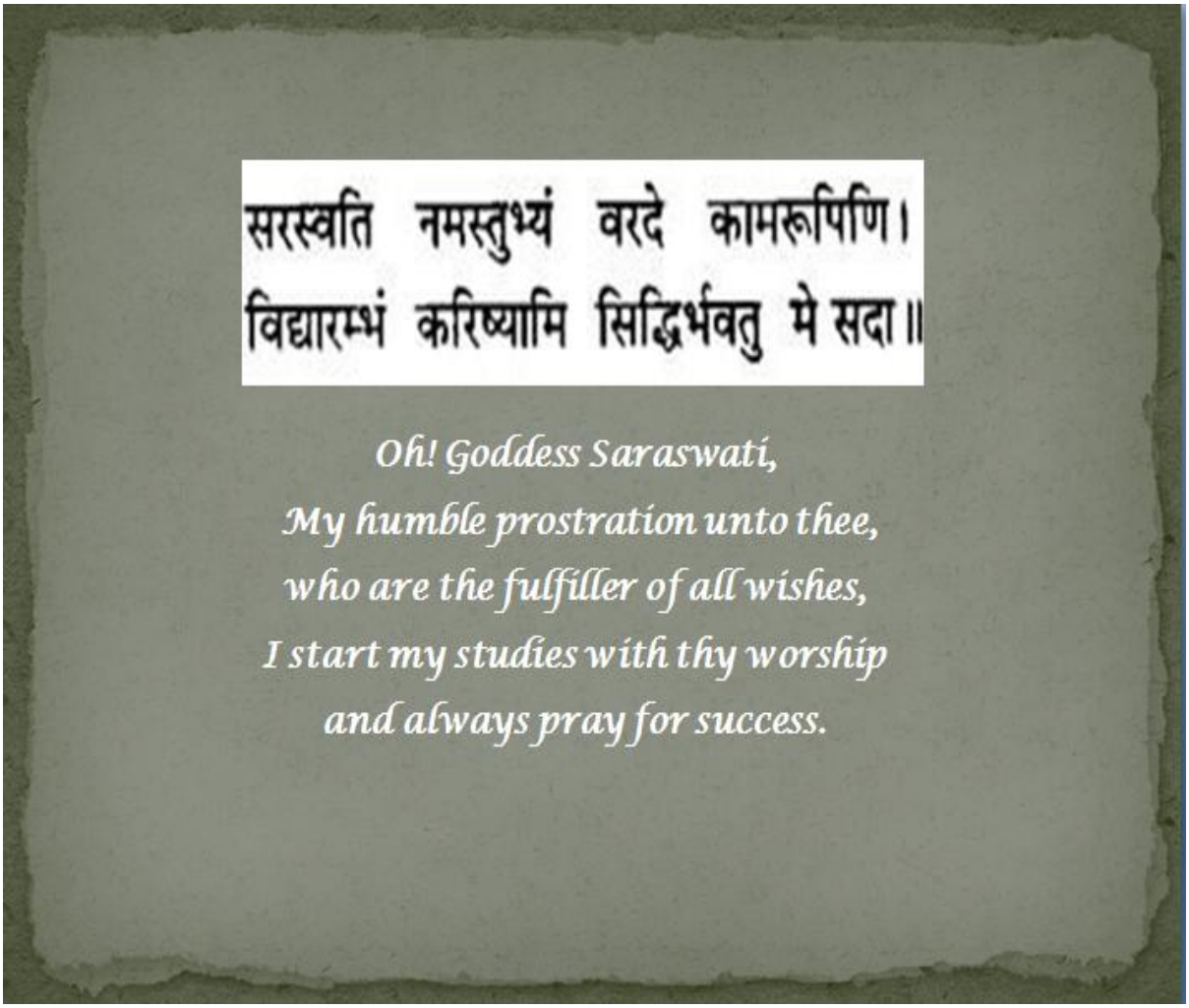
सरस्वति नमस्तुभ्यं वरदे कामरूपिणि।
विद्यारम्भं करिष्यामि सिद्धिर्भवतु मे सदा॥
Oh! Goddess Saraswati,
My humble prostration unto thee,
who are the fulfiller of all wishes,
I start my studies with thy worship
and always pray for success.

To

My Beloved Parents

Acknowledgement

I humbly fold my hands and bow in the supremacy of my maker for all HIS kindness that he has bestowed on me.

Foremost, I would like to express my profound gratitude to my supervisor and mentor, Dr. N. K. Verma who shared with me a lot of his expertise and research insight. He has guided me from the very early stage of this research as well as provided me with persistent encouragement and support throughout the work. His undying passion in science exceptionally inspired and enriched my growth as a student and as a researcher as well. His thoughtful advices, motivation to take every failure in a positive stride inspired me to work harder towards my goal. It served to give me a sense of direction during my PhD studies and helped me in completing my project in the present form. I also wish to extend my heartfelt gratitude to Mrs. (Dr.) Rama Verma for her motherly warmth and affection.

I am highly obliged to Department of Science & Technology, Government of India, New Delhi for awarding me INSPIRE Fellowship to pursue my doctoral work.

I wish to thank my doctoral committee members, Dr. Kulvir Singh, Professor & Head, School of Physics and Materials Science, Dr. B. N. Chudasama, Assistant Professor, School of Physics and Materials Science and Dr. Amjad Ali, Associate Professor, School of Chemistry and Biochemistry, for carefully scrutinizing the progress of my research work and providing me with all their encouraging words during the hour of need.

I am deeply thankful to Dr. K. K. Raina, Director, Thapar University and the entire faculty of School of Physics and Materials Science for all their heartening words and support.

Acknowledgement

I heartily acknowledge the helping nature of the non-teaching and secretarial staff for all their needful assistance.

I would like to record my gratitude towards my seniors and fellow research scholars, Dr. Sanjeev Kumar, Dr. Manveen Kaur, Mr. Gurmeet Singh Lotey, Mr. Jaspal Singh Patra, Ms. Gitanjali Dhir, Mrs. Kamaldeep and Ms. Imanpreet Kaur for their constant encouragement, love and support. They all in their own ways have been a vital part of this journey of mine and have contributed to the fulfilment of my research work. I deeply admire the support and care I received from Mrs. Supreet Gogna and Dr. Gudveen Sahwney. I am tempted to individually thank my friends and best pals Mrs. Harkiran Sembi, Mr. Jatinder Singh who have joined me in the discovery of what life is all about, how to make the best of it and cheering me during all low times. I am genuinely thankful to my brother, Mr. Jagpreet Singh Nanda for his immense support, care and encouragement.

Where would I be without my family? So, I cannot finish without saying how indebted I am to my family. My parents deserve a very special mention for their inseparable & ardent support, everlasting love and invariable prayers that they blessed me with. My father, Mr. C. M. Khanna, in the first place is the person, who explained to me the joy of intellectual pursuit and hard work ever since I was a child and my mother Mrs. Anita Khanna for all her love, motivation and affection. Every time I flinched, they stood by me as my pillars of strength and pulled me up in their own unique ways; this reassured my belief in myself. Words of wisdom that I get from them always guide me as my torch-bearers. They have always motivated and

Acknowledgement

Acknowledgement

inspired me to do my best in all matters of life and left no stone unturned to see me successful and happy. To them, I dedicate this thesis with all my love and respect - Mum, Dad. My siblings and their better-halves, Mrs. Divya Singh & Mr. Bikramjit Singh, Mrs. Bhumika Khanna & Mr. Pyush Khanna have been my best companions and best critics. They have always given me the most straight-forward, logical and practical dose of advice and showered their unending support, care and love on me. My two little angels, Anahat (niece) and Manit (nephew) are the ones I madly adore; their cute smiles brighten up my day.

A sincere gratitude to my grandmother, Mrs. Satya Kapoor and my aunt, Ms. Karuna Kapoor for all their unconditional love, support, care and blessings, at the time me and my family needed it the most.

Khanna

(Lavanya Khanna)

Contents

Contents

Contents

Chapter 3 - Calcium ferrite nanocomposites

Contents

Contents

List of Figures

List of Figures

List of Figures

List of Figures

List of Tables

List of Publications

I. Papers in SCI journals

1. Lavanya Khanna, N. K. Verma, Size-dependent magnetic properties of calcium ferrite nanoparticles, Journal of Magnetism and Magnetic Materials, 336 (2013) 1–7.

2. Lavanya Khanna, N. K. Verma, Silica/potassium ferrite nanocomposite: Structural, morphological, magnetic, thermal and in vitro cytotoxicity analysis, Materials Science and Engineering B, 178 (2013) 1230-1239.

3. Lavanya Khanna, N. K. Verma, PEG/$CaFe_2O_4$ nanocomposite: Structural, morphological, magnetic and thermal analyses, Physica B, 427 (2013) 68–75.

4. Lavanya Khanna, N. K. Verma, Synthesis, characterization and invitro cytotoxicity study of calcium ferrite nanoparticles, Materials Science in Semiconductor Processing, 16 (2013) 1842-1848.

5. Lavanya Khanna, N. K. Verma, Synthesis, characterization and biocompatibility of potassium ferrite nanoparticles, Journal of Materials Science and Technology, 30(1) (2014) 30-36.

6. Lavanya Khanna, N. K. Verma, Biocompatibility and superparamagnetism in novel silica/$CaFe_2O_4$ nanocomposite, Materials Letters, 128C (2014) 376-379.

7. Lavanya Khanna, N. K. Verma, Study on novel, superparamagnetic and biocompatible PEG/$KFeO_2$ nanocomposite, Journal of Applied Biomedicine (10.1016/j.jab.2014.05.003).

II. Papers in non-SCI journals

1. Lavanya Khanna, N. K. Verma, Synthesis and characterization of silica coated potassium ferrite nanoparticles, AIP Conf. Proc. 1536, 71-72.

2. Lavanya Khanna, N. K. Verma, Structural and morphological studies of PEG coated potassium ferrite nanoparticles, Excel India publisher, 2154-2159.

List of Publications

III. Conference presentations

1. Lavanya Khanna, N. K. Verma, $SiO_2/Ca_2Fe_2O_5$: A novel nanocomposite for biomedical applications, BIOSENSORS - 24th Anniversary World Congress on Biosensors, Melbourne, Australia, 2014.
2. Lavanya Khanna, N. K. Verma, Structural, morphological and magnetic studies of silica coated calcium ferrite nanorods, International conference on Nanotechnology in the service of Health, Environment & Society (NanoSciTech 2014), Panjab University, Chandigarh, February, 2014
3. Lavanya Khanna, N. K. Verma, Dose-dependent biocompatibility of PEG/Potassium ferrite nanocomposite, Emerging Horizons in Science & Technology, SGGSWU, Fatehgarh Sahib, January, 2014.
4. Lavanya Khanna, N. K. Verma, Structural and magnetic studies of calcium ferrite nanocomposite, Emerging Trends in Physics for Environmental Monitoring & Management (ETPEMM-12), Punjabi University, Patiala, December 2012.
5. Lavanya Khanna, N. K. Verma, Synthesis and characterization of potassium ferrite nanoparticles for bio-medical applications, 23rd Annual General Meeting of materials Research Society of India (MRSI), Thapar University, Patiala, February, 2012.
6. Lavanya Khanna, N. K. Verma, Synthesis and characterization of calcium ferrite nanoparticles for bio-medical applications, 4th Bangalore Nano Conference, December, 2011.
7. Lavanya Khanna, Nahar Singh, Umesh K. Tiwari, Inderpreet Kaur, N. K. Verma, Lalit M. Bharadwaj, Antibody immobilization on optical fiber for immunosensing applications, 14th Punjab Science Congress, SLIET, Longowal, February, 2011.
8. Lavanya Khanna, L. M. Bharadwaj, Inderpreet Kaur, N. K. Verma, Antibody detection using optical fiber long period grating immunosensor, International conference on Nanoscience and Technology, CSIO, Chandigarh, October, 2010.

Abstract

Magnetic nanoparticles (MNPs) have been comprehensively scrutinized for biomedical applications, where the quintessential requirements are that the particles must be nanosized, superparamagnetic and biocompatible. Going through the literature, one can observe that ferrites of Ni, Mn, Co, Zn have been investigated for various biomedical applications such as drug delivery, magnetic resonance imaging (MRI) and hyperthermia. Although they exhibit superior magnetic properties, their inherent toxicity elevates concerns on their use in biomedical applications and reduces their efficacy. Ferrites of calcium and potassium are expected to more biocompatible since both these elements are inherently non-toxic.

In addition to the above mentioned requisites, another factor that decides the effectiveness of MNPs is their ability to covalently bond to biological entities and agglomeration. These two factors decide the fate of MNPs and become the cause for inhibition of the specific property or application for which it was employed. Thus, making it indispensable to functionalize/coat the surface of MNPs with appropriate functional groups or stabilizers. The most widely employed stabilizers among organic polymers and inorganic material is polyethylene glycol (PEG) and silica, respectively. These have been used as the stabilizers in the present thesis.

In a nutshell, the present thesis attempts to introduce calcium ferrite nanoparticles and potassium ferrite nanoparticles along with their respective nanocomposites as novel, superparamagnetic and biocompatible materials for biomedical applications. Altogether, six combinations (bare $CaFe_2O_4$ NPs, PEG/$CaFe_2O_4$ NPs, silica/$CaFe_2O_4$ NPs, bare $KFeO_2$ NPs, PEG/$KFeO_2$ NPs, silica/$KFeO_2$ NPs) have been studied. Their structural, morphological, compositional and magnetic analyses have been done by X-ray Diffractometer (XRD), Scanning

electron microscope/Transmission electron microscope (SEM/TEM), Energy dispersive X-ray spectroscope (EDAX) and Vibrating sample magnetometer (VSM), respectively. Thermal (TGA/DTA) as well as FTIR analyses have also been carried out. In vitro cytotoxicity test on T cell lines (Jurkat cells), using 3-(4, 5-Dimethylthiazol-2-yl)-2, 5-diphenyltetrazolium bromide (MTT) assay have been performed in order to investigate their dose-dependent cytotoxicity.

Thesis Structure

In the present thesis, two materials viz. calcium ferrite nanoparticles ($CaFe_2O_4$ NPs) and potassium ferrite nanoparticles ($KFeO_2$ NPs) have been studied. Both these nanoparticles have been further coated with polyethylene glycol (PEG) and silica. Therefore, two sections (chapter 3 and chapter 4) have been prepared comprising of three combinations each. One is about bare $CaFe_2O_4$ NPs, PEG coated $CaFe_2O_4$ NPs and silica coated $CaFe_2O_4$ NPs. The other deals with bare $KFeO_2$ NPs, PEG coated $KFeO_2$ NPs and silica coated $KFeO_2$ NPs. The structural, morphological, thermal, FTIR, magnetic and cytotoxicity analyses of all the combinations mentioned above have been studied. Following is the chapter-wise description of the thesis.

Chapter 1 - Introduction

This chapter covers brief and selective introduction to nanotechnology highlighting the emergence of magnetic nanoparticles in bio-nanotechnology. The essential requirements related to this application have been discussed, covering the literature work reported so far. It also includes the insight and grounds on which the objectives for the present thesis were shaped.

Chapter 2 - Synthesis methods and characterization techniques

This chapter provides an overview of the synthesis methods used for preparing calcium ferrite nanoparticles and potassium ferrite nanoparticles. The synthesis procedures for the preparation of polyethylene glycol (PEG) and silica coated nanocomposites have also been discussed. The various characterization techniques such as X-ray diffraction (XRD), Scanning electron microscope (SEM), Transmission electron microscope (TEM), Energy dispersive X-ray spectroscope (EDAX), Thermal gravimetric analysis (TGA/DTA), Vibrating sample magnetometer (VSM), Fourier transform infrared spectroscope (FTIR), and 3-(4, 5-

Dimethylthiazol-2-yl)-2, 5-diphenyltetrazolium bromide (MTT) assay have been explained in detail. The working principle and instrumentation of all the techniques mentioned above have been covered.

Chapter 3 - Calcium ferrite nanocomposites

The present chapter includes the experimental procedures for synthesizing calcium ferrite nanoparticles and their surface coating with PEG and silica. Their structural, morphological, FTIR, thermal and magnetic properties along with cytotoxicity have been studied.

Chapter 4 - Potassium ferrite nanocomposites

The present chapter includes the experimental procedures for synthesizing potassium ferrite nanoparticles and their surface coating with PEG and silica. Their structural, morphological, FTIR, thermal and magnetic properties along with cytotoxicity have been studied.

Chapter 5 - Conclusions and future plan

This chapter summarises the conclusions of the research work presented in the thesis. Also, it gives an insight into the future possibilities for augmentation of the work.

Chapter – 1

INTRODUCTION

Chapter 1

The advent of nanotechnology has led to unprecedented development in all facets of science and technology. This chapter covers brief and selective introduction to nanotechnology highlighting the emergence of magnetic nanoparticles in bio-nanotechnology. The essential requirements related to this application have also been discussed.

1.1 Introduction

1.1.1 The nano-world

From the metering standpoint, a nanometer is a unit of length which equals to one billionth (10^{-9}) of a meter. In Greek, nano denotes "dwarf (very small)"; this is the common paradigm governing its definition in the scientific community. Nano-scale refers to the characteristic size of the materials in the range of 1-100 nm, a strand of human hair is approximately 75,000 to 1,00,000 nanometers in diameter [1]. Nanotechnology is about producing, manipulating and controlling things at nano-scale for diverse applications. Nanoscience is the related science that explains the fundamental relationships between physical properties and phenomena occurring at the nano dimension.

Reduction from macro to nano-scale is accompanied with size dependent phenomenon viz. increase in surface to volume ratio, discretization of energy bands, quantum confinement effects and activation of the surface atoms [2, 3]. These significantly change the mechanical,

electrical, optical and/or magnetic properties of the material, enabling the nanomaterials to behave differently from its bulk counterpart. These changes can be further harnessed for developing newer technologies or for augmentation of the existing ones. This makes nanotechnology a potential tool for revolutionising every facet of science and technology.

The fascination of nanotechnology stems from the fact that it encompasses all the sciences i.e. physics, chemistry or biology. The technique from one discipline can be synchronized with the techniques and expertise of other disciplines, thus enabling unique applications and challenges. This requires multi-disciplinary and trans-disciplinary efforts, thereby attracting the researchers worldwide to explore more into this field. This has led to synthesis of different nanomaterials and nanostructures.

1.1.2 Nanostructured materials

Nanostructured materials are those which have atleast one of their dimensions falling in the nano-scale [4]. Depending on it, nanostructures are classified as follows:

1. Zero-dimensional nanostructures− all the dimensions fall in the nanoscale such as nanoparticles, quantum dots. These include single crystal (nanocrystals), polycrystalline and amorphous particles with possible morphologies, such as spheres and cubes. Quantum dots are those nanoparticles in which the characteristic dimensions are so small that quantum effects become dominant [4].

2. One-dimensional nanostructures− one dimension falls in the nano-scale such as nanowires, nanorods.

3. Two-dimensional nanostructures− two dimensions fall in the nano-scale such as thin films, multi-layers.

1.1.3 Synthesis and processing of nanoparticles

Many techniques, including both top-down *(breaking larger blocks to smaller structures)* and bottom-up *(assembling small building blocks into larger structures)* approaches have been developed and applied for the synthesis of nanostructures. Top-down approaches includes high energy ball-milling, repeated quenching and lithography [4]. All these techniques suffer from one or other drawbacks which make it difficult to control and produce desired particle size, shape and distribution.

Bottom-up approaches such as chemical synthesis, self-assembly, laser-induced assembly are far more popular and widely employed [4, 5]. Among them, synthesis by homogeneous nucleation is one approach, wherein the size controlling fundamentals such as growth rates, concentration of growth species play a crucial role in obtaining the desired size, shape and distribution [4]. Metallic colloidal dispersion is another technique used for the synthesis of metallic nanoparticles, wherein parameters such as types of precursors, reduction reagents, control the reduction reactions, the initial nucleation and the subsequent growth of initial nuclei [4]. Sol-Gel process, co-precipitation are wet chemical routes for the synthesis of oxide nanoparticles. Kinetically controlled synthesis of nanoparticles is done by spatially confining the reaction (growth) using surfactants or block polymers, in microemulsion or micelles [4, 5]. Many techniques have been employed for obtaining different morphologies at nano level such as nanowires [6], nanocrystalline thin films [7, 8].

1.1.4 Applications of nanotechnology

Integration and utilization of nanotechnology in other sciences have resulted in wide applications ranging from electronics, materials science, data storage devices, band gap engineered quantum devices, temperature sensors, plasmon waveguides, photonic crystals, and biological systems to novel materials [9-11]. Undoubtedly, nanotechnology has embedded its roots in almost all the domains of the scientific community. Thus, it has proven to be a technology with a power to influence our lives to a greater extent.

Magnetic materials have been extensively explored in diverse and technological applications [12-15]. The amalgamation of nanotechnology with biology has given rise to the field of bio-nanotechnology, wherein magnetic nanoparticles (MNPs)/ nanocomposites, in particular, find wide applications in magnetic cell-separation of labelled cells and biological entities, therapeutic targeted drug and gene delivery vehicles, contrast enhancement agents in magnetic resonance imaging (MRI), magnetic bio-sensing, hyperthermia treatment; because of their non-toxic nature, distinct surface and magnetic properties [16-23].

1.2 Magnetic nanoparticles

MNPs as the name suggests, represent the class of materials which have dimensions in the nano-scale and can be controlled with an external magnetic field [4]. The magnetic properties are extremely sensitive to size, composition, and local atomic environment [3]. MNPs are widely used for biomedical applications due to its (i) non-toxicity (ii) biocompatibility and biodegradability (iii) injectability and (iv) high level accumulation in the target tissue [19]. There are certain limitations related with MNPs, these are discussed in detail in the next section.

1.2.1 Need of surface coatings on magnetic nanoparticles

Pertaining to the high surface energy and magnetic interactions of the magnetic nanoparticles, they have the tendency to agglomerate. When the nanoparticles agglomerate, they adsorb plasma proteins and are quickly cleared by the macrophages in the Reticuloendothelial system (RES, a part of the immune system of the human body) before reaching the target cells [18]. The body instead of allowing them to work efficiently recognizes them as a foreign entity and removes them. This reduces the circulation time of nanoparticles in the blood stream. The agglomeration results in clogging of the capillaries, this can be avoided by coating of the nanoparticle surface. Also, the surface inertness of nanoparticles restricts the number of molecules to be bio-conjugated with them [24, 25]. These two factors decide the fate of MNPs. These further become the cause for inhibition of the specific property or application for which it was employed. These two limitations can be reduced by functionalizing/coating the surface of MNPs with appropriate functional groups or stabilizers [25]. It should be taken well into care that the functionalization of MNPs not only must facilitate them for selective binding to biological entities but should also be non-toxic, hydrophilic *(Particles with hydrophobic surface are rapidly coated with plasma proteins (their hydrophobic surface leads to hydrophobic-hydrophobic interactions), this process is called opsonization. The opsonized particles are recognized by the RES and taken up by the phagocytic cells and macrophages of the RES and released out of the body. This encourages their rapid removal from blood circulation. However, particles with hydrophilic surface resist the plasma protein coating process. So, it is desirable that the superparamagnetic nanoparticles must be coated with a hydrophilic material in order to inhibit the opsonization process, also it has been reported that hydrophobic surface is more*

cytotoxic than hydrophilic group [26]), biocompatible, superparamagnetic and stable in aqueous suspensions [25]. The surface coatings (stabilizers) on the MNPs are required to:

(i) provide stabilization of MNPs against aggregation [27],

(ii) increase biocompatibility [22]

(iii) protect against corrosion [22]

(iv) evade Reticuloendothelial System (RES) [28]

(v) help in binding different biological ligands to the nanoparticle surface [29].

The nature of the coating and its consequent geometric arrangement determines the overall size and plays a vital role in biokinetics and biodistribution of nanoparticles in the body [19]. The strategic objective is to contour the properties of the non-toxic nanocomposite for optimal magnetic response within the biological size constraints.

In recent years, there has been an escalating interest in functionalizing/coating the surface of MNPs with inorganic/organic materials. The most widely employed stabilizers among organic polymers and inorganic material is polyethylene glycol (PEG) [30-41] and silica [42-54], respectively. These have been used as the stabilizers in the present thesis and are discussed in detail, below.

1.2.1.1 Polyethylene glycol

The term PEGylation is used specifically for attaching or coating the nanoparticle surface with PEG molecules through surface adsorption, covalent linkages or entrapment [31]. PEG is a polymer of ethylene oxide and water. It has the general formula - $H(OCH_2CH_2)$ nOH, where n is the average number of repeating (OCH_2CH_2) groups ranging between 4-180. It is typically a non-toxic, non-immunogenic, non-antigenic and protein resistant polymer, which is widely used

in the pharmaceutical field [32-35]. It is water soluble, inert in biological systems and does not influence cell viability [34, 35]. This makes it a widely acclaimed material for effective shielding of the surface charge of nanoparticles to disperse them, as it has uncharged hydrophilic residues and high surface mobility [31, 34, 36, 37]. PEGylated nanoparticles improve stealth properties unmatched by any other surface coating [38]. It serves as a protective layer that inhibits agglomeration of the particles, provides protection against corrosion, evades Reticuloendothelial System (RES), helps in binding various biological ligands to the nanoparticle surface and reduces the direct exposure of the ferrite surface to the biological environment, thereby enhancing the biocompatibility [33, 34].

1.2.1.2 Silica

Among inorganic materials, silica is the most preferred stabilizer. Silica is known to be biocompatible and chemically inert, so it does not affect the redox reaction at the core (ferrite) surface [42-44]. It eliminates protein adsorption and also facilitates the functioning of the nanocomposite in biological environment [42]. It screens the magnetic dipolar interaction between magnetic nanoparticles, thus preventing their aggregation; this favours their dispersion in liquid media. Also, it protects MNPs from leaching in an acidic environment. The existence of abundant silanol groups on the silica layer allows various functional groups for bio-conjugation to be activated on the coated surface [43]. Unlike polymers, it is not subject to microbial attack and it neither swells nor changes porosity in response to the environmental pH values [42]. Silica protects nanoparticles from acidic erosion. Correspondingly, the particle stability leads to reduced cytotoxicity [45].

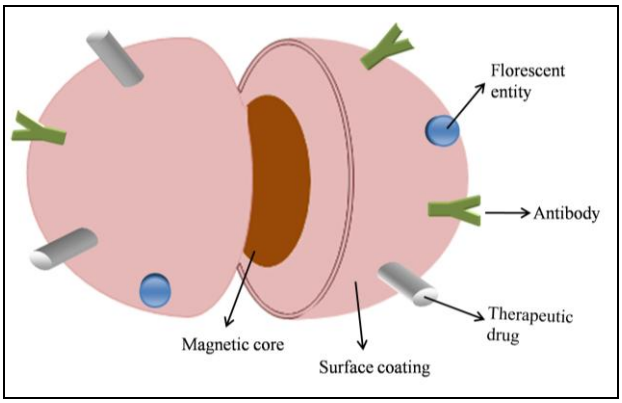

Figure 1.1 Magnetic nanocomposite with different bio-conjugations depending on the specific application

This results in the formation of magnetic nanocomposite that comprises of a magnetic core and a protective surface coating, which can be further modified with drug molecule, antibodies, florescent entities etc., depending on the specific application, as shown in fig. 1.1.

It is very essential that the so formed magnetic nanocomposite exhibits the following requirements for its effective working in biomedical applications.

1.2.2 Essential requirements

1.2.2.1 Nanosize

It is very essential that the tools used at the cellular level match the dimensions of that level, as one cannot use a human arm to treat hurt leg of an ant [20]. The overall size or hydrodynamic size of the nanocomposite is a major and primary parameter for an effective drug carrier, as, the magnetic properties, circulation profile in the blood vessel and clearance strongly depends on size [33]. Decuzzi et al. produced models suggesting that smaller sized spherical nanoparticles observed higher diffusion rates with increased concentration at the centre of a blood vessel, thus limiting interactions with endothelial cells (*The endothelium is the thin layer*

of cells that lines the interior surface of blood vessels, forming an interface between circulating blood in the lumen and the rest of the vessel wall. Endothelial cells line the entire circulatory system, from the heart to the smallest capillary) and prolonging the blood circulation time [33]. MNPs (size ranging from a few nanometres up to tens of nanometres) have dimensions smaller than or comparable to those of a cell (10-100 μm), a virus (20-450 nm), a protein (5-50 nm) or a gene (2 nm wide and 10-100 nm long), enabling them to penetrate smaller capillaries and get close to any biological entity or target site [21].

Following methodical administration, particles with diameters greater than 200 nm are usually mechanically filtered and sequestered by the spleen; eventually these are removed by the cells of phagocyte system, thus decreasing the blood circulation times. Also, the chances of larger particles clogging the small capillaries become significant [33, 54]. On the other hand, smaller particles with size less than 5 nm are quickly removed through extravasations and renal clearance. Therefore, particles ranging from 5-100 nm are optimal for intravenous injection owing to their most prolonged blood circulation times. Another advantage is that the particles within this size range are small enough both to escape Reticuloendothelial System (RES) of the body and penetrate the very small capillaries. This rules out the possibility of clogging the capillaries and offers the most effective distribution in the body. Also, they have higher effective surface areas (easier attachment of ligands), lower sedimentation rates (high stability) and improved tissular diffusion, so, the preferred size lies in the range of 5-100 nm [54].

1.2.2.2 Superparamagnetic behaviour

The other characteristic required is that the nanoparticles and nanocomposite must be superparamagnetic. Superparamagnetic properties arise from a finite-size effect [55]. This

appears in ferromagnetic or ferrimagnetic nanoparticles. In ferromagnetic materials, a long-range ordering phenomenon occurs due to dipole interaction. This makes the dipoles to line up in parallel orientation. Pertaining to energetic reasons, the size range of this parallel orientation is limited; these ranges are known as magnetic domains, usually they are smaller than the grain size. Magnetic domains, within a grain are separated by *Bloch* walls and the direction of magnetization is changed by moving the *Bloch* walls. Therefore, the existence of magnetic domains and *Bloch* walls make it easier to change the direction of magnetization. In general, a ferromagnetic material remains magnetized to some extent on removal of the magnetic field; this effect is called remanence and the magnetic field required to compensate remanence is called coercivity. The tendency of a material to memorize its magnetic history is called hysteresis.

Large magnetic nanoparticles are subdivided by *Bloch* walls into magnetic domains, as their sizes are energetically controlled, so remanence and coercivity are largely independent of the particle size. On reducing the particle size, no long range order exists in the material. When the particle size becomes smaller than the critical diameter, D_c, the particles consist of a single magnetic domain (Fig. 1.2). As the *Bloch* walls ease the change of magnetization, coercivity and remanence increases drastically; this is the particle size range for magnetic data storage. On further size-reduction, below superparamagnetic diameter, D_{sp}, coercivity and remanence rapidly approach to zero i.e. magnetization curve exhibits no hysteresis (fig. 1.2).

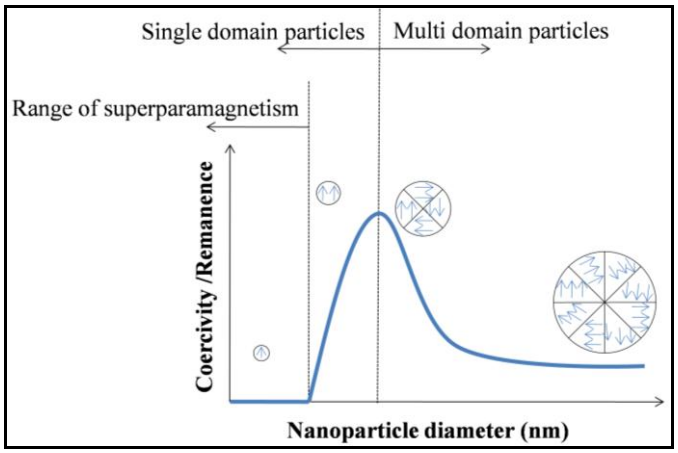

Figure 1.2 Coercivity/Remanence as a function of nanoparticle diameter [55]

In case of a single isolated magnetic nanoparticle, the condition leading to superparamagnetism is of typical thermal instability, given as

$$kT \geq Kv \tag{1.1}$$

where K is the constant of magnetic anisotropy, v is the volume of particle, Kv is the energy of magnetic anisotropy and kT is the thermal energy (k is the Boltzmann constant and T is the temperature). This phenomenon has been explained by magnetic anisotropy, which is an intrinsic property of any magnetic material and is independent of grain size. The energy required for magnetizing a ferro or ferrimagnetic crystal depends on the magnetic field direction relative to the orientation of the crystal, thus leading to “easy” and “hard” directions. These are the directions where the application of an external field easily magnetizes - the “easy” direction or to a lower magnetization - the “hard” direction. In superparamagnetic materials, the vector of magnetization fluctuates between the easy magnetic directions, overcoming the hard directions. Corresponding to easy axis, the magnetic moment usually has only two stable orientations,

separated by an energy barrier of height $\Delta E = Kv$. If $Kv \gg kT$, then moment cannot switch spontaneously, pertaining to permanent magnet. However, if the energy barrier is of the order of the thermal energy, $Kv \sim kT$ or less, then spontaneous switching can occur on the timescale of the experiment pertaining to superparamagnetic materials. The magneto-crystalline anisotropy originates from the coupling between electron spins and the angular momentum of the electron orbital (L-S coupling). Therefore, the superparamagnetic behaviour of a particle, which is directly related to its magneto-crystalline anisotropy, can be correlated to its L-S coupling as well [56, 57]. It is directly proportional to the volume of particles ($E_A = KV \sin^2\theta$), where, K is the magneto-crystalline anisotropy constant (related to the strength of the L-S coupling), V is the volume of the nanoparticle and θ is the angle between the magnetization direction and the easy axis of the nanoparticle. E_A serves as an energy barrier for blocking the flips of magnetic moments [56, 57].

The typical time between the thermally excited fluctuations, with frequency *f*, is called Néel relaxation time $\tau = (2\pi f)^{-1}$. In the absence of an external magnetic field, when the time taken for measuring the magnetization of the nanoparticles is much longer than the Néel relaxation time, the magnetization appears to be of average zero: pertaining to superparamagnetic state. In this state, an external magnetic field magnetizes the nanoparticles, similar to a paramagnet. However, their magnetic susceptibility is much larger than that of a paramagnet. When an assembly of superparamagnetic nanoparticles is subjected to an external magnetic field, their magnetic moments tend to align along the applied field, thus leading to a net magnetization. The magnetization curve so- obtained is a reversible S-shaped increasing function. Normally, above the Curie temperature, any ferromagnetic or ferrimagnetic material undergoes a transition to a

paramagnetic state, but superparamagnetism differs, as this occurs below the Curie temperature of the material.

The lack of remanent magnetization in superparamagnetic nanoparticles is attributed to the fact that each magnetized superparamagnetic domain readily jumps between two stable orientations which are separated by a small energy difference [55]. This energy difference is so small that thermal energy cancels the total magnetization. In case of superparamagnetic particles, thermal fluctuations are strong enough to spontaneously demagnetize a previously magnetized assembly. The superparamagnetic behavior is reflected in less squareness value, M_R/M_S ratio, where M_R, M_S are the remanent magnetization, saturation magnetization, respectively [17]. The squareness value for non-interacting superparamagnetic particles is 0.5 [58], in the case of interacting superparamagnetic particles the dipolar interactions reduce both the magnetic squareness (M_R/M_S ratio) and coercivity (H_C) values due to demagnetizing effect [58, 59]. Magnetic squareness value pertaining to superparamagnetic behaviour is 0.1, i.e. it loses greater than 90% of its magnetism when the applied magnetic field is removed [60].

Superparamagnetic nanoparticles become magnetic in the presence of an external magnet, but return to a nonmagnetic state on its removal. This circumvents their 'active' behavior in absence of the field and such behaviour is ideal for biomedical applications. Generally, a localized magnetic field gradient is used for attracting and retaining the nanoparticles to a selected site until the completion of the therapy, subsequently followed by their removal [28, 61]. The advantage of using superparamagnetic nanoparticles for this application is that as the magnetic field is applied, the triggering response for its planned action begins and it stops as soon as the magnetic field is removed. This enables effective control on their planned action and time of exposure.

1.2.2.3 Biocompatibility

Biocompatibility is yet another important feature that is highly required for biomedical applications. It is very essential that the synthesized nanomaterial/nanocomposite should be non-toxic for in vitro or in vivo applications.

To determine toxicity of nanoparticles, many cell viability assays such as Lactate dehydrogenase (LDH) [62], Cell counting Kit-8 (CCK8) [63], 3-(4,5-dimethylthiazol-2yl)-5-(3-carboxymethoxyphenyl)-2-(4-sulfophenyl)-2H tetrazolium, inner salt (MTS) [62, 64], Sulforhodamine B (SRB) [46], 3-(4, 5-Dimethylthiazol-2-yl)-2, 5-diphenyltetrazolium bromide, a tetrazole (MTT) [26, 47, 65-67] have been used, which measure the effect of nanoparticles' exposure on the cells. Among them, MTT assay is considered the ''gold standard'' for cytotoxicity [68]; this is recommended for fast and accurate determination of cytotoxic effects [66].

1.2.3 Magnetic nanoparticles/nanocomposites in biomedical applications

Iron oxide based nanomaterials have been extensively employed in biomedical field [24, 29, 35, 37, 45, 46]. Upon metabolism, iron ions are added to the body's iron stores and eventually incorporated by erythrocytes as haemoglobin, this allows their safe use for in vivo applications [69]. The cytotoxicity profile of PEG-coated superparamagnetic iron oxide nanoparticles (SPION) revealed no cytotoxic effect even at concentration of 1mg/ml, however, uncoated SPION showed significant loss in viability of about 25%-50% at concentration of 250µg/ml, the less cytotoxicity of PEG coated is attributed to high solubility of PEG in the cell membranes [36]. The cellular viability of magnetic, florescent, folic acid conjugated silica nanocomposite was found to be greater than 90% at the concentration of 70µg/ml [47]. A

comparison of MNPs and silica coated MNPs has been reported, a similar trend was observed, where the cell viability of silica coated samples was higher as compared to the uncoated samples [48].

Other than iron oxide, ferrites of Ni ($NiFe_2O_4$) [70, 26, 28], Mn ($MnFe_2O_4$) [67, 71], Co ($CoFe_2O_4$) [72, 73] and Zn ($ZnFe_2O_4$) [70] have also been investigated for biomedical applications. Dose-dependent cytotoxicity of metal ferrites (Ni, Mn, Co, Zn) have been reported [67, 70-72]. The cytotoxicity of $NiFe_2O_4$ (20-30 nm), $ZnFe_2O_4$ (15-30 nm) at 100 µg/ml showed viability of 77.6%, 59.4% and 70.5%, 52.4% for 24 h and 48 h, respectively [70]. The viability of $MnFe_2O_4$ nanowires at different concentrations was evaluated using MTT assay; at 100 µg/ml cell death and cell proliferation inhibition was observed [71]. $MnFe_2O_4$ nanoparticles were investigated for the MRI contrast agent applications wherein these exhibited ~70% cellular viability at 200 µg/ml [67]. The cellular viability of $CoFe_2O_4$ nanoparticles on HeLa cells was found to be ~80% at 20 µg/ml [72].

Even though the ferrites of Ni, Mn, Co, Zn metals exhibit superior magnetic property, the high inherent toxicity of these metals raises apprehensions and speculations on their efficacy for biomedical applications [22]. So, the need of the hour is to synthesize highly bio-favourable ferrites with no inherent toxicity threat so that even if leaching does occur the metal used should not cause any harm to the body. For this, calcium and potassium metals can be considered as good candidates, as both of them are inherently non-toxic.

The ferrites of calcium and potassium in bulk form have been reported. Calcium ferrite compounds so far have extensively been explored in the optical memory devices, steel making industry (as deoxidizer, desulfuration, and dephosphorization), pigment and absorbent of hydrogen sulfide (H_2S) [74-77]. Also, potassium and iron based compound in bulk form i.e.

potassium ferrate, has been studied for dyeing, waste-water purification and disinfection [78-81]. Ferrites of calcium and potassium in the nano-regime have not been explored much. Their superparamagnetism, functionalization and biocompatibility at nano-scale have also not been investigated.

In the present thesis, calcium ferrite and potassium ferrite nanoparticles have been synthesized. The synthesized nanoparticles were further coated with polyethylene glycol (PEG) and silica. The structural, morphological, FTIR, thermal, magnetic properties and biocompatibility of uncoated and coated nanoparticles have been investigated.

Chapter – 2

SYNTHESIS METHODS AND CHARACTERIZATION TECHNIQUES

Chapter 2

The first step towards realization of the various applications of nanomaterials is the synthesis of those nanomaterials. Synthesis involves meticulous effort and suitable variation of the experimental parameters for controlling size, shape, composition etc. The present chapter deals with the brief description of the synthesis methods and the various characterization techniques for investigating the structural, morphological, thermal and magnetic properties along with cytotoxicity of the synthesized nanoparticles and nanocomposites.

2.1 Synthesis methods

In the present thesis, syntheses of calcium ferrite nanoparticles and potassium ferrite nanoparticles were done by sol-gel method. Silica and polyethylene glycol (PEG) coating on the synthesized nanoparticles were done by stober method and hydrothermal method, respectively. Brief descriptions of all these methods are written below.

2.1.1 Sol-gel method

Sol-gel method has proved to be a versatile technology, as it used for producing wide variety of materials which have optical, electrical, mechanical, chemical, biological and biomedical applications [82]. Sol-gel technique has become very popular recently for biomedical applications due to their high chemical homogeneity, low processing temperature, and the

possibility of controlling size and morphology of particles [83]. This is a widely employed method for synthesizing nanomaterials.

A typical sol-gel method starts with a solution consisting of a source of metal compound, water as hydrolysis agent, alcohol as solvent and acid or base catalyst [82]. The solution undergoes hydrolysis and polycondensation, forming sol with fine particles dispersed in it. Hydrolysis is a chemical reaction in which hydroxyl groups get attached to metal atom by replacing the ligands in the precursor, thus forming M-OH bonds, where M stands for the required metal and in polycondensation, groups merge to form M-O-M bonds, while releasing water molecule and linking the clusters into chains and networks [84]. Further reaction connects the particles and solidifies the sol into a wet sol, in which water and solvents are still present. Usually, various shapes are formed during the transformation from sol to gel. Vaporization of water and solvents results in a dry gel and eventually the final product is obtained. Fig. 2.1 shows the schematic of the sol-gel method.

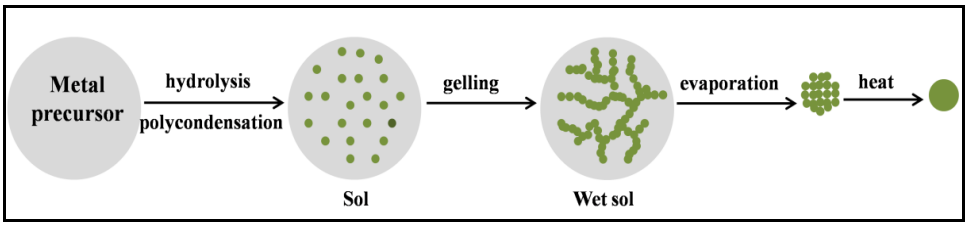

Figure 2.1 Schematic of sol-gel processing of materials [85]

The advantages of sol-gel method, in general are high purity, high homogeneity, low processing temperature and an environmental friendly process [82, 84].

2.1.2 Stober method

Stober method is a pioneering method for the synthesis of spherical and monodisperse silica nanoparticles from aqueous alcohol solutions of silicon alkoxides in the presence of ammonia as a catalyst [86, 87]. Tetraethyl orthosilicate (TEOS) is the source of silica used in this process. It is controlled by the relative contribution of nucleation and growth processes [88]. It is characterised by hydrolysis and condensation reactions, which provide precursor species and the necessary super-saturation for the formation of particles, respectively. It is during the hydrolysis reaction, that the ethoxy group of TEOS reacts with water molecule in order to form the intermediate [Si $(OR)_{4-x}$ $(OH)_x$, R = C_2H_5] with hydroxyl group substituting ethoxy groups [88]. Ammonia acts as a basic catalyst in this reaction wherein the hydrolysis reaction is initiated by the attack of hydroxyl anions on TEOS. In general, the hydrolysis reaction of TEOS produces the singly-hydrolyzed monomer - $(OR)_3Si(OH)$, Eq. 2.1 [88, 89].

$$Si(OR)_4 + xH_2O + NH_3 \rightarrow (^{-}O)_xSi(OR)_{4-x} + xROH + NH_4^{+} \quad (2.1)$$

After the hydrolysis reaction, the condensation reaction occurs immediately [88, 89]. In it the hydroxyl group of intermediate [Si $(OR)_{4-x}$ $(OH)_x$] reacts with either the ethoxy group of other TEOS (alcohol condensation) or the hydroxyl group of another hydrolysis intermediate (water condensation) to form Si-O-Si bridges, Eqs. (2.2) and (2.3). [88, 89]

$$Si(OR)_4 + (OH)Si(OR)_3 \rightarrow (OR)_3Si\text{-}O\text{-}Si(OR)_3 + ROH \quad (2.2)$$

$$(OR)_3Si(OH) + (OH)Si(OR)_3 \rightarrow (OR)_3Si\text{-}O\text{-}Si(OR)_3 + H_2O \quad (2.3)$$

It is well-observed that silanol groups are formed by hydrolysis and siloxane bridges are formed by condensation reaction [86]. This is the most widely employed method for surface coating of MNPs with silica.

2.1.3 Hydrothermal method

Hydrothermal synthesis is about reactions in aqueous media above 100°C, where reactants are dissolved in water and placed in a Teflon-lined stainless steel autoclave (fig. 2.2) and heated above the boiling point of water.

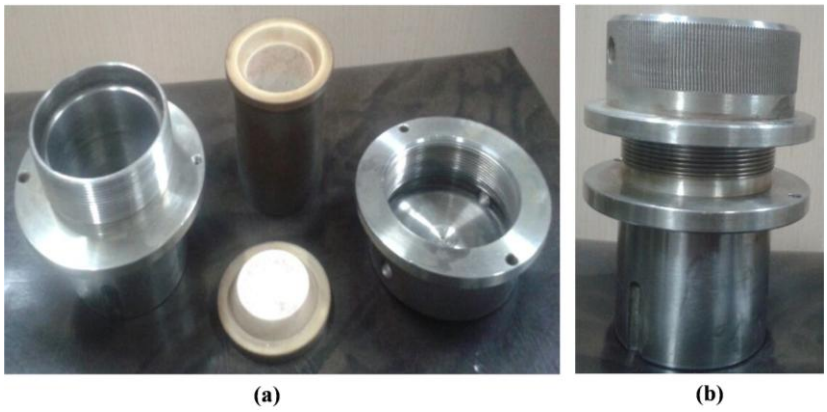

Figure 2.2 (a) Different parts of an autoclave (b) an assembled autoclave

The pressure achieved in the reaction vessel is adjusted by varying either the reaction temperature and/or empty space in the container. This method represents a special type of transport reaction which relies on the liquid-phase transport of reactants to nucleate the formation of the desired product [90]. Besides water for hydrothermal synthesis, liquid ammonia is also used. Ammonium ion has low boiling point so the reaction pressure is quite high [91].

The synthesized nanoparticles and nanocomposites were characterized by the following techniques.

2.2 Characterization techniques

2.2.1 X-ray diffraction

2.2.1.1 Introduction

Diffraction effects are observed when electromagnetic radiation strikes onto the periodic structures having geometrical variations at the wavelength-scale of the radiation used [92]. The inter-atomic distances in crystals and molecules amount to 0.15–0.4 nm which corresponds to the wavelength of X-rays with photon energies between 3 and 8 keV [92]. Accordingly, phenomena like constructive and destructive interference are apparently observed on exposure of the crystalline and molecular structures to X-rays. There are three different types of interaction in this energy range. In the first, electrons are activated from their bound atomic states in the process of photo-ionization. As energy and momentum get transferred from the incoming radiation to the excited electron; this makes photo-ionization to fall into the group of inelastic scattering processes. There occurs a second kind of inelastic scattering that the incoming X-ray beams may undergo; this is known as Compton scattering. During this process, energy is transferred to an electron which proceeds without releasing the electron from the atom. Finally, X-rays may be scattered elastically by electrons, this is called Thomson scattering. In this, the electron oscillates like a Hertz dipole with the frequency of the incoming beam, thus itself becoming a source of dipole radiation. The wavelength λ of X-rays is conserved for Thomson scattering unlike the two inelastic scattering processes mentioned above. Thomson scattering is used for structural investigations of the material. X-rays are used as a probe to investigate the internal structure of a material.

2.2.1.2 Instrumentation and working principle

In 1913, W. L. Bragg gave the theory of X-ray diffraction (XRD) [92]. The parallel planes of atoms reflect the incident beams of X-rays. The reflected rays interfere constructively and produce maximum intensity. The path difference between the reflected rays is $2d\sin\theta$, where d is the inter-planar spacing and θ is the angle between the incident beam and the crystal plane. The constructive interference occurs when $2d\sin\theta = n\lambda$, where n = 0, 1, 2...This is known as Bragg's law (fig. 2.3).

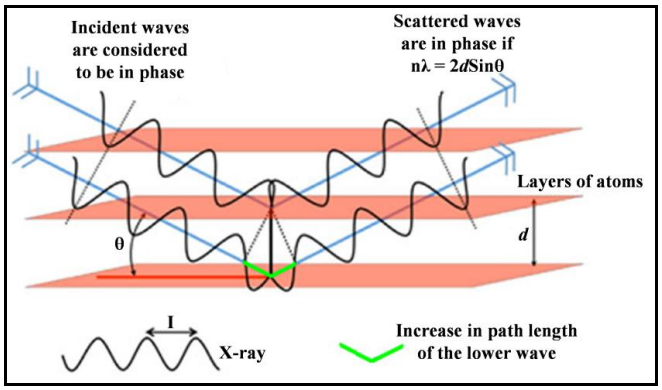

Figure 2.3 Bragg's Law [93]

It should be noted that the Bragg's reflection and diffraction pattern is possible as the inter-planar spacing is of the order of the wavelength of the X-rays. It cannot be observed with visible light as in it the above-mentioned condition is not satisfied.

X-ray diffractometers consist of three basic elements: X-ray tube, sample holder, and X-ray detector, as shown in fig. 2.4 [94]. X-rays are generated in a cathode ray tube by heating the filament to produce electrons; they are accelerated towards the target by applying a voltage. When these electrons obtain sufficient energy to displace inner shell electrons of the target material, characteristic X-ray spectra are produced. These spectra consist of several components,

the most common being K_α and K_β. The specific wavelengths obtained are characteristic of the target material (Cu, Fe, Mo, Cr). Filtering with the help of foils or using crystal monochrometers is necessary for producing monochromatic X-rays, as it is highly required for diffraction. Copper is the most commonly used target material for single-crystal diffraction, with CuK_α radiation = 1.5418 Å. These produced X-rays are collimated and directed onto the sample. On rotation of the sample and detector, intensity of the reflected X-rays is recorded. When the incident X-rays irradiating the sample satisfies the Bragg Equation, constructive interference takes place, leading to an increase in the peak intensity. A detector records and processes this X-ray signal and further converts it into a count rate which is then transferred to a computer.

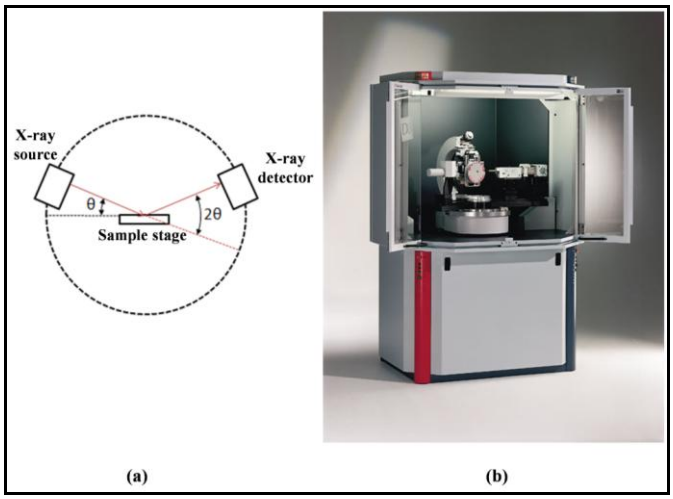

Figure 2.4 (a) Parts of X- ray Diffractometer [94] (b) Pictorial view of an X-ray diffractometer [95]

In an X-ray diffractometer, sample rotates in the path of the collimated X-ray beam at an angle θ while the X-ray detector is so mounted that it collects the diffracted X-rays at an angle of 2θ. *Goniometer* is the instrument used for measuring the angle and rotating the sample [94].

2.2.1.3 Sample preparation

Few gram of sample is taken and is ground to obtain a fine powder. It is then placed in the sample holder assuring a flat upper surface. The upper surface should be as smooth as possible for obtaining proper results.

2.2.1.4 Information from XRD

X-ray diffraction is most widely used in geology, environmental science, material science and engineering [95]. Following are some of its applications.

- To identify the unknown crystalline materials (e.g. minerals, inorganic compounds).
- To determine the structural information of crystalline materials.
- To determine unit cell dimensions.
- To determine the sample purity.

In the present thesis, the X-ray patterns of the synthesized nanoparticles and nanocomposites were recorded on X-ray diffraction (XRD, X'Pert PRO Panalytical MRD ML).

2.2.2 Scanning electron microscope

2.2.2.1 Introduction

Microscopy involves the study of objects that are too small to be examined by the unaided eye. It enables the investigation of specimens with a resolution down to the nanometer scale.

2.2.2.2 Instrumentation and working principle

Basically, electrons produced by an electron source are accelerated in a field gradient in vacuum. The beam passes through the assembly of electromagnetic lenses and is focused on the specimen to be investigated. This bombardment results in emission of different types of electrons generated from the specimen. Detector grabs the secondary electrons and constructs an image of the sample surface by comparing the intensity of these emitted secondary electrons to the primary electron beam [96, 97]. Finally the image is displayed on a monitor, as shown in fig. 2.5 [98].

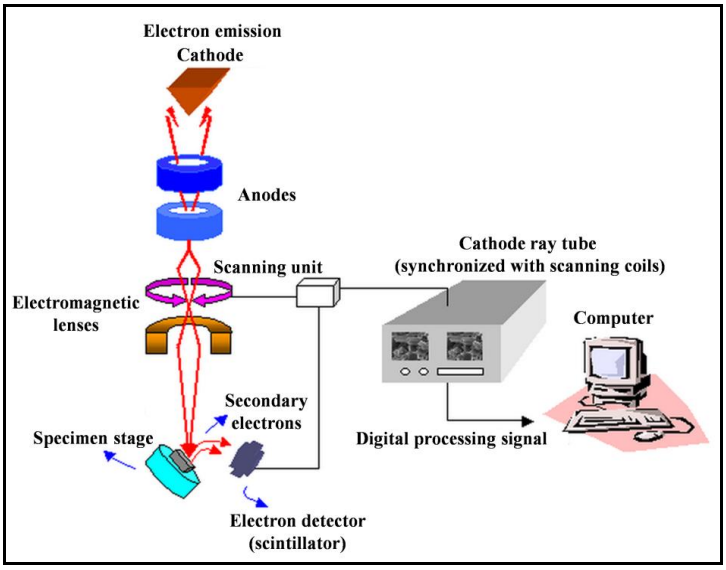

Figure 2.5 Working principle of a SEM [98]

The major components of SEM include seven primary operational systems: vacuum, beam generation, beam manipulation, beam interaction, detection, signal processing, display and record [98]. All these systems mutually work together to obtain the results and desired qualities of micrograph such as magnification, resolution, depth of field, contrast, and brightness. These systems have been discussed briefly, as follows [98].

a) Vacuum - The environment within the column is extremely critical for the proper functioning of an electron microscope. In absence of sufficient vacuum in SEM, electron beam can neither be generated nor controlled. Generally, the operating pressure of a SEM is about 10^{-4} - 10^{-6} Torr.

b) Electron Gun - It is the beam generation system of an electron microscope and is composed of three components: i) a filament or cathode made of tungsten wire, Lanthanum Hexaboride (LaB_6) crystal, or Cerium Hexaboride (CeB_6), ii) a grid cap (Wehnelt Cylinder) for controlling the flow of electrons (bias), and iii) a positive charged anode plate for attracting and accelerating the electrons down the column and further to the specimen.

c) Beam manipulation - Electrons generated by electron gun are accelerated by an electrostatic field, while in the rest parts of the SEM, the electrons are controlled by magnetic lenses. Electromagnetic lenses or condenser lenses are used to reduce the stray beam and control its size by making it as a fine spot. Other types of magnetic lenses are used for correcting astigmatism and alignment, as all electromagnetic lenses have spherical aberration (It is the inability of the lens to image the central and the peripheral portions of the electron beam at the same focal point). This affects the final resolution of micrograph; therefore the correcting lenses are highly required. As the beam moves through the final condenser lens, two sets of magnetic scanning coils move the beam in order to scan in both the X and Y directions. The scan pattern so-obtained is called a raster pattern and the coils used for obtaining the pattern are called raster coils.

d) Beam interaction - When the primary electron enters a specimen it probably travels some distance into the specimen before striking another particle. On striking an electron or a nucleus, etc., the primary electron continues on in a new trajectory; known as scattering. These scattering events are most interesting, as it is the components of the scattering events (not all events include electrons) that can be detected. When the primary beam hits the specimen, formation of a teardrop shaped reaction vessel occurs (Fig. 2.6). This is the place where all the scattering events take place. Small reaction vessels are likely to give better resolution, where large reaction vessels tend to provide more signals. The volume of a reaction vessel is dependent on the atomic density, topography of the specimen and the acceleration potential of the primary electron beam [98]. The scattering of primary beam gives rise to: i) Back-scattered electrons, ii) Secondary electrons, iii) X-rays, iv) Cathode luminescence, v) Specimen current, vi) transmitted electrons. These have been shown in fig. 2.6.

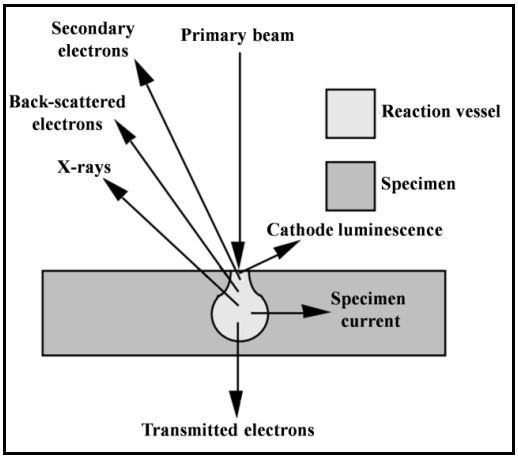

Figure 2.6 Types of signals in a SEM [97]

e) Detection - Different detectors are used for different types of signals generated. Most SEMs are equipped with an Everhart-Thornley (E-T) detector [99]. Topographical

information is primarily offered by the secondary electrons, so a secondary electron detector magnetically attracts the emitted secondary electrons by a potential and these are accelerated by scintillator. Hitting the scintillator causes the photons to be emitted which are amplified by a photomultiplier (PM) tube. The amount of amplification is decided by the PM voltage control (contrast control).

f) **Signal processing** - Signal processing begins with the amplifier and terminates with the image on the screen. The signal obtained in the SEM is converted to an image, which is further seen on a cathode ray tube (CRT). The screen of CRT comprises of a series of points termed as pixels. Pixels are just dot-like structures present on the screen of the shade of gray ranging from black to white. The PM Voltage (contrast control) regulates the amplification of the electrons obtained by the secondary or backscatter detector. The PM voltage controls the multiplication of the pixels by a given amount.

g) **Display and record -** Brightness, contrast, resolution, magnification, depth of field and noise are the factors that determine the quality of the micrograph. Brightness is the value of each individual pixel that composes the image. Higher the overall pixel value, brighter is the image obtained. Contrast is related to the difference between the lowest and the highest pixel value. By definition, resolution corresponds to the ability to distinguish between two points. Another factor i.e. magnification is a function of area scanned to the viewing size (CRT or Film), which is adjusted by two controls (i) the raster coils and (ii) position of the focal point of the primary beam as compared to the final lens. Another factor i.e Depth of field is a function of the distance of the specimen to the final lens. It is the region of acceptable sharpness in front of and

behind the point of focus. On adjusting the working distance by bringing the specimen closer to the final lens, less depth of field and greater resolution can be achieved. Lastly, noise corresponds to any level of brightness observed in a micrograph, white or black, which is not a result of the designed interaction of the beam with the specimen. By adjusting the above parameters, as desired by the user, the micrograph can be saved and recorded in the computer. Fig. 2.7 shows the pictorial view of a SEM.

Figure 2.7 Pictorial view of a SEM [100]

2.2.2.3 Sample preparation

The basic care pertaining to specimen preparation is to manipulate the specimen to the minimum, ensuring that the sample is of appropriate size, stable in the vacuum, electrically conductive, dry and possessing characteristics resembling its natural state [97]. Most metallic samples satisfy these conditions with little or no preparation, whereas, many other materials such

as ceramics, plastics, and minerals require to be coated with a conducting metal as gold. The powdered samples are adhered to the stub by double adhesive carbon tape and coated with gold.

2.2.2.4 Information from SEM

- SEM is a very essential research tool in the fields of nanotechnology, life science, medical, forensic science, metallurgy and industry-related fields.
- In addition to topographical, morphological and compositional information in the nano-dimension, it can detect and analyze surface fractures, provide information in microstructures, examine surface contaminations, reveal spatial variations in chemical compositions, provide qualitative chemical analyses and identify crystalline structures [101].

In the present thesis, SEM micrographs of the synthesized nanoparticles and nanocomposites were recorded on SEM: JSM, 6510 LV, JEOL, U.S.A, where the dried sample was first coated with gold using JEOL, JFC sputter coater.

2.2.3 Transmission electron microscope

2.2.3.1 Introduction

Transmission electron microscope (TEM) is another kind of research tool which works on the same principle as scanning electron microscope (SEM), where electrons are used for extracting morphological information of a material. In TEM, a fraction of the incident electron beam goes through the sample to be studied. The electrons interact with the sample and result in transmitted electrons, backscattered electrons, secondary electrons, coherent elastic scattered electrons, incoherent inelastic electrons, incoherent elastic forward scattered electrons,

characteristic, continuum X-rays and auger electrons, etc [102]. These interactions are further detected by different detectors, and finally the images are generated.

2.2.3.2 Instrumentation and working principle

A TEM is composed of four components: electron source, electromagnetic lens system, sample holder, and imaging system, as shown in fig. 2.8 [103].

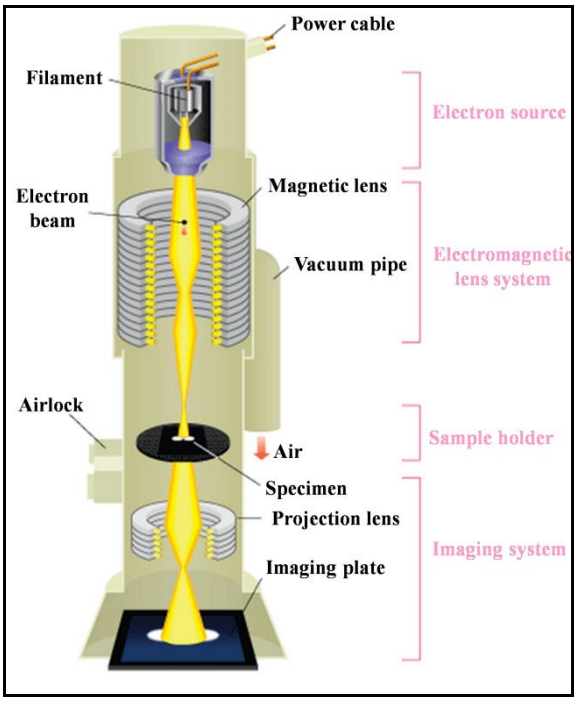

Figure 2.8 Schematic outline of a TEM [103]

The illumination system comprises of electron gun and condenser lenses; their role is to transfer the electrons from the source to the specimen [102]. The electron source consists of a cathode and an anode. Cathode is a tungsten filament which emits electrons on heating. The electron beam is accelerated towards the specimen by the positive anode. Electrons at the rim of the beam fall onto the anode while the others at the centre pass through the small hole of the anode [103]. The electron beam is accelerated to energy in the range 20 - 1000 keV in the

electron gun where the electron beam goes though a set of condenser lenses for producing a beam of electrons with desired diameter. Two principal modes are operated in the illumination system (i) parallel beam and (ii) convergent beam. The first mode is used largely for TEM imaging. The electron beam is tightly focused using electromagnetic lens and apertures. The system only allows electrons within a small energy range to pass through, so the electrons in the electron beam have a well-defined energy. It is used to restrict the electron beam and filter out unwanted electrons before hitting the specimen. The objective lens along with the specimen holder/stage system is the heart of TEM. This is the place where all of the beam-specimen interactions occur and the fundamental TEM operations takes place, namely, formation of the different images and diffraction patterns (DP) which are afterwards magnified for viewing and recording. It is the imaging system that uses numerous lenses for magnifying and focussing the image or DP produced by the objective lens on the viewing screen or computer display. These are then recorded on a conventional film situated either below or above the fluorescent screen, which glows on being hit by electrons. Image is formed in a way similar to photography. Fig. 2.9 shows the pictorial view of a TEM.

Figure 2.9 Pictorial view of a TEM [104]

TEM is majorly used to generate either a diffraction pattern of the specimen or for obtaining the quantitative information about the microstructure of the material in the form of several types of images.

2.2.3.3 Sample preparation

The powdered samples are ultrasonically dispersed in ethanol. A drop of this solution is spread on carbon coated copper grid to view images.

2.2.3.4 Information from TEM

- TEM provides topographical, morphological, size and crystalline information of the material.
- It is an essential research tool for viewing images of the nanomaterials. Also, it can be used to analyse the composition of the material. Regions with higher thickness or higher atomic numbers appear darker in the resulting image.
- Crystalline regions diffract parts of the beam. Instead of generating an image, the electron microscope also allows switching to the diffraction pattern of a specimen region at the same time.
- Selected area electron diffraction (SAED) allows the determination of the exact crystal type and lattice distances of a phase in a material.
- High Resolution Transmission Electron Microscopy (HRTEM) enables lattice fringe imaging which is directly related to the structure and revelation of defects and interfaces at atomic scale resolutions.

In the present thesis, TEM micrographs of the synthesized nanoparticles and nanocomposites were recorded on transmission electron microscope (TEM; Hitachi (H-7500)). SAED patterns and HRTEM images were obtained by High-resolution Transmission Electron Microscope (TEM-JEOL2100F).

2.2.4 Energy dispersive X-ray spectroscope

2.2.4.1 Introduction

X-rays are always produced during the measurement process in electron microscopy. A characteristic X-ray yields information about the chemical composition of the material [105]. By using energy dispersive X-ray spectroscopy, the quantification of elements can be obtained. Energy Dispersive X-ray Analysis (EDAX or EDS) technique is used for executing chemical analysis in combination with Scanning Electron Microscopy (SEM) and Transmission Electron Microscopy (TEM) and is not a surface science technique [105].

2.2.4.2 Instrumentation and working principle

EDAX makes use of the X-ray spectrum emitted by a solid sample bombarded with a focused electron beam to obtain a localized chemical analysis [106]. Fig. 2.10 shows the schematic representation of an EDAX and its associated electronics.

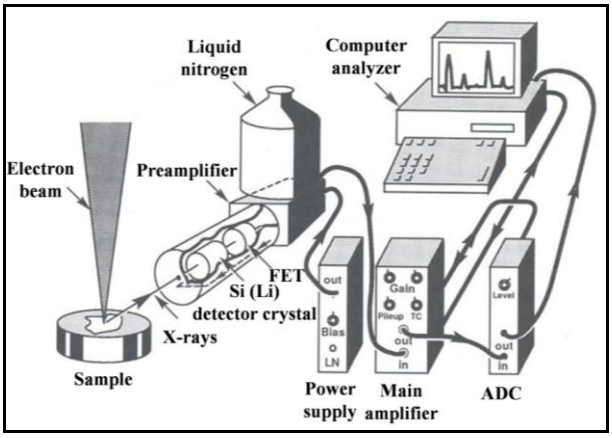

Figure 2.10 Schematic representations of an EDS and associated electronics [106]

An electron beam hits the surface of a conducting sample (SEM) or of a thin film (TEM). Typically, the energy of the beam lies in the range of 10-20 keV. This causes X-rays to be emitted depending on the irradiated material. All the elements from atomic number 4 (Be) to 92 (U) can be detected in principle, though not all instruments are equipped for 'light' elements (Z < 10) [107]. A Beryllium window is often used to protect the Si (Li) detector in the EDAX system. This detector needs to be operated at liquid nitrogen temperatures. Detectors as well as the preamplifier are cooled with liquid nitrogen in order to minimize electronic noise [107]. When an X-ray strikes the detector, it generates a photoelectron within the body of the Si. On travelling through the Si, this photoelectron generates electron-hole pairs. Strong electric field further attracts these generated electrons and holes to opposite ends of the detector. Charge-to-voltage converter (preamplifier) changes these to voltage pulse, which is further proportional to the energy of the X-ray. The amount of current pulse thus generated is dependent on the number of electron-hole pairs created and the energy of the incoming X-ray. Fig. 2.11 shows the pictorial view of an EDAX attached to SEM.

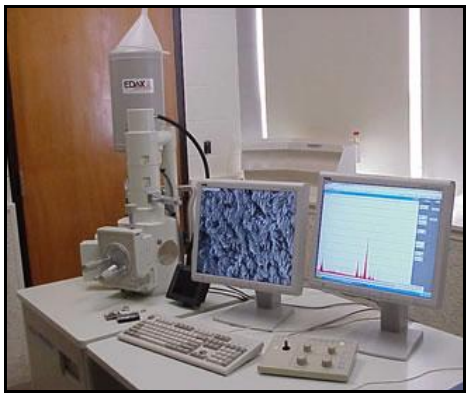

Figure 2.11 Pictorial view of an EDAX attached to SEM [108]

The absorption of the soft X-rays by Be excludes the detection of those elements with atomic number below that of 11 (Na). In windowless EDAX systems, although elements with less atomic number of 4 (Be) have been detected, but the problems get increasingly worse on further reduction. The intensity or area of a peak in an EDAX spectrum is relative to the concentration of the corresponding element in the material. In order to determine the elemental content, it is assumed that the electron-beam current is uniform throughout the specimen and electron channeling is evaded by avoiding strong diffraction conditions.

2.2.4.3 Sample preparation

The sample preparation is same as that of SEM. Finely ground powdered sample is placed on carbon double adhesive tape. The excess powder is removed. The sample is coated with gold and is used for analysis.

2.2.4.4 Information from EDAX/EDS

EDAX is a powerful research tool for contamination analysis and industrial forensic science investigations.

- The EDAX spectrum gives a quick compositional analysis.
- It provides the spatial distribution of elements through mapping from which the homogeneity of multi-phase systems can be ascertained.
- Analysis of the resulting X-ray energy spectrum at each position provides plots of the relative elemental concentration variance for each element as a function of those position-point values along the given path.

In the present thesis, the EDAX analysis of the synthesized nanoparticles and nanocomposites was done with energy-dispersive X-ray analysis (EDAX/EDS, Oxford).

2.2.5 Thermogravimetric and differential thermal analyzer

2.2.5.1 Introduction

Thermal analysis detects the inert-atomic and inter/intra-molecular interactions of a material relative to the temperature change [109]. Thermogravimetric analysis (TGA) uses heat to derive reactions and physical changes occurring in a material [110]. It provides quantitative measurement of mass change in a material associated with any transition, dehydration, oxidation or thermal degradation. TGA curves are characteristic for a given material owing to the distinctive reactions occurring over specific temperature ranges and heating rates. The changes in mass are representative of the thermodynamics and kinetics of the various chemical reactions [110]. In differential thermal analysis, the material and reference are subjected to undergo identical thermal cycles and the temperature difference is characteristic of exothermic or endothermic reactions in the material. DTA usually complements TGA with phase transition information.

2.2.5.2 Instrumentation and working principle

In TGA, mass of the material is measured as the function of time or temperature while the material is subjected to a controlled temperature, increasing or decreasing at a specific heating rate. As mass is a fundamental feature of a material, so any change in it is reflective of a chemical or compositional change. The derivative of the TG curve gives information about the point where weight loss is most apparent. The instrument used in thermogravimetry (TG) is called a thermobalance. The basic components are listed below and shown in fig. 2.12 [111, 112].

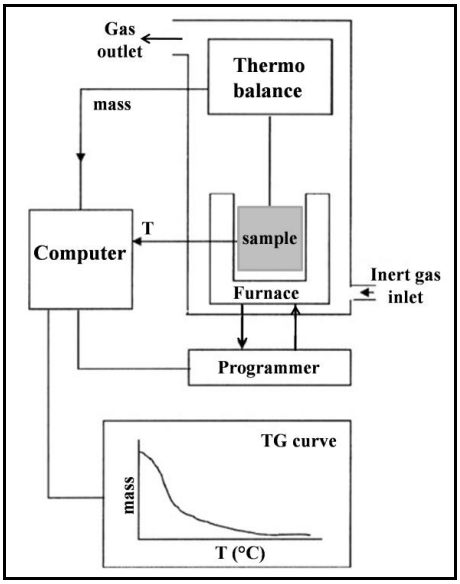

Figure 2.12 Schematic of a TGA [111]

a) **Balance -** The essential features of an automatic recording balance are accuracy, sensitivity, reproducibility, and capacity [111, 112]. Also, it should be of adequate range for automatic weight adjustment with high degree of mechanical and electrical stability, simple to operate, quick to weight changes and unaffected by vibrations [113]. Generally, recording balances are one of two types, null point

and deflection type. It is the null type balance which is more widely used. It incorporates a sensing element which detects deviations of the balance beam from its null position. A sensor detects the deviation and triggers a restoring force which brings the balance beam back to the null position. The restoring force is directly proportional to the mass change. Deflection balance involves the conversion of the balance beam deflection about the fulcrum into a suitable mass-change signal. Each of the balances used in TG instruments have measuring ranges from approximately 0.0001 mg to 1 g.

b) **Furnace and Control System -** The furnace and control system are designed to generate a continuous and linear heating rate, or maintain a steady state temperature for isothermal testing. Each model and manufacturer has a different set range of temperature. Temperature is measured using one or multiple thermocouples.

c) **Thermogravimetric Analysis -** Temperature is controlled or varied using a programmer with a dual thermocouple arrangement. The signal from the first thermocouple is used to stimulate the control system; the signal from the second thermocouple is used to record the temperature.

d) **Recorder -** X-Y recorders are commonly used for plotting sample mass directly against temperature. The instrument facilitates the microprocessor controlled operation and digital data acquisition on a computer.

The balance should be in a suitably enclosed system, in an inert atmosphere, so that the nature and pressure of the atmosphere surrounding the sample can be well-controlled. For

obtaining DTA curve, two cups are used, in one the reference material is put and in the second sample is used.

2.2.5.3 Sample preparation

Few milligram of sample is taken and is ground to obtain a fine powder to achieve greater contact area and better equilibrium conditions [113, 114]. The time at any temperature must be sufficiently long and heating rate should be slow in order to permit completeness of reactions. Fig. 2.13 shows the pictorial view of a TGA/DTA.

Figure 2.13 Pictorial view of a TGA/DTA [115]

2.2.5.4 Information from TGA/DTA

The TGA and DTA curves give the following information [113, 114].

- To determine changes in sample composition.
- To study thermal stability and material purity.
- To determine kinetic parameters for chemical reactions in the sample.

- To determine the energy changes corresponding to phase transition, oxidation, reduction etc. occurring in a material.

In the present thesis, the thermal analysis of the synthesized nanoparticles and nanocomposites was done with Differential Thermal Analyzer (DTA; Pyris 1 TGA, Perkin Elmer).

2.2.6 Fourier transform infrared spectroscope

2.2.6.1 Introduction

Fourier transform infrared (FTIR) spectroscopy depends on the fact that the most compounds whether organic or inorganic absorb light in the infra-red region of the electromagnetic spectrum. Infrared refers to that part of the electromagnetic spectrum which lies in between the visible and microwave regions [116]. The IR region is divided into three regions: near, mid and far IR. The mid IR region is of the greatest practical use to a chemist [117]. In terms of wavenumbers, the mid IR range extends from 4000 to 400 cm^{-1}. Infrared radiation is absorbed by the compounds and converted into energy of molecular vibrations.

2.2.6.2 The infrared absorption process

Infrared spectroscopy is a technique based on the vibrations of the atoms of a molecule [116-118]. An infrared spectrum is commonly obtained by passing infrared radiation through a sample and determining what fraction of the incident radiation is absorbed at a particular energy. The energy at which any peak in an absorption spectrum appears corresponds to the frequency of a vibration of a part of a sample molecule.

The adsorption of IR radiation is a quantized process. A molecule adsorbs only selected frequencies or energies of IR radiation. This adsorption corresponds to energy changes of the order of 8-40 kJ/mole [119]; this further encompasses the stretching and bending vibrational frequencies of the bonds in most of the covalent molecules. In this process, those frequencies of IR radiation which match the natural vibrational frequencies of the molecule are adsorbed and this further increases the amplitude of the vibrational motions of the bonds in that molecule. It should however be noted that not all bonds in a molecule absorb infrared energy, even if the frequency of the radiation matches precisely with that of the bond motion. Only the ones whose dipole moment changes as a function of time are capable of absorbing IR radiations. A bond must possess an electrical dipole varying at the same frequency as the incoming radiation for the energy to be transferred, making it an IR active molecule. The changing electrical dipole of the bond then couples with the sinusoidally changing electromagnetic field of the incoming radiation. This results in vibrational motion of the IR active molecule in stretching and bending modes. These are further classified as symmetric, anti-symmetric, scissoring, rocking, wagging and twisting modes corresponding to fundamental absorptions. When two vibrational frequencies couple, it gives rise to new frequency within the molecule and is called combination band. Since every type of bond has a unique vibrational frequency and also two same bonds in two different compounds are actually in two different environments, so no two molecules of different structure have exactly the same IR absorption spectrum. Therefore, IR spectrum of a molecule is similar to fingerprint of the humans.

The instrument that determines the absorption spectrum of a compound is called an infrared (IR) spectrometer or spectrophotometer. The two most commonly used IR spectrometers are dispersive and Fourier transform infrared (FTIR) spectrometers. Among

them, FTIR is the most widely used as it provides the spectrum much more rapidly than the dispersive spectrometer.

2.2.6.3 Instrumentation and working principle

A common FTIR spectrometer comprises of a source, interferometer, sample compartment, detector, amplifier, A/D convertor, and a computer, as shown in fig. 2.14 [119, 120]. The source generates IR radiation which passes through the sample in the Michelson interferometer and finally reaches the detector. Michelson interferometer (the core of FTIR spectrometers) splits one beam of light into two beams such that the paths of the two beams are different. The two beams get recombined and are conducted into the detector. The differences in the intensity of these two beams are measured as a function of the path difference, resulting in constructive or destructive interference.

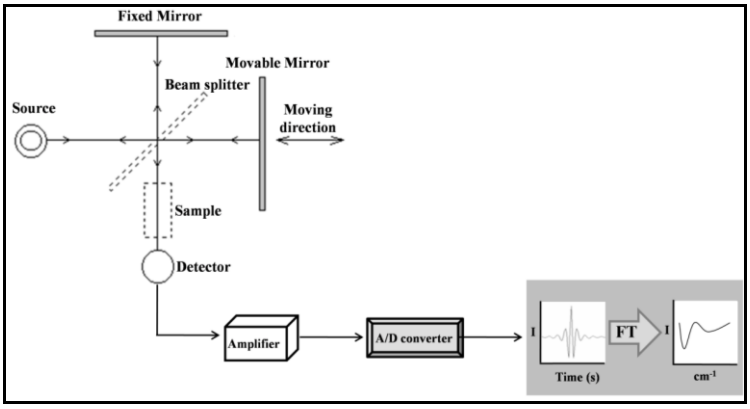

Figure 2.14 Schematic representation of a FTIR spectrometer [119, 120]

The signal, so obtained is amplified and converted to digital signal by the amplifier and A/D converter, respectively. The design of the optical pathway produces a pattern called an interferogram. The interferogram is typically a complex signal with wave-like pattern containing all the frequencies that make up the IR spectrum. It is essentially a plot of intensity versus time

(time domain). Eventually, the signal is transferred to a computer in which a mathematical operation called fourier transform is carried out. The time domain is fourier transformed to get the spectrum in the frequency domain. Fig. 2.15 shows the pictorial view of a FTIR spectrometer.

Figure 2.15 Pictorial view of a FTIR spectrometer

2.2.6.4 Sample preparation

The powdered sample is mixed with finely ground powdered potassium bromide and pressed under high pressure. Under pressure, potassium bromide melts and seals the compound into a matrix, thus forming KBr pellets. This pellet is inserted into the sample holder and the spectrum is obtained.

2.2.6.5 Information from FTIR

FTIR spectroscopy is an analytical tool and can be used for gathering the following information of a compound:

- To assess the purity of a compound along with its structural information.
- To confirm the formation of desired functional groups in a nanocomposite.
- To identify unknown compounds in a complex material.

In the present thesis, the FT-IR spectra (4000-400 cm^{-1}) of the synthesized nanoparticles and nanocomposites were recorded on Perkin Elmer Spectrum BX (II) and Perkin Elmer Model- RZX spectrophotometers.

2.2.7 Vibrating sample magnetometer

2.2.7.1 Introduction

Vibrating sample magnetometer (VSM) technique is one of the popular techniques for measuring the magnetic properties. It operates on Faraday's law of induction, which states that a changing magnetic field produces an electric field [121, 122]. This generated electric field can be measured, yielding information about the changing magnetic field and hence the magnetic properties of the material.

2.2.7.2 Instrumentation and working principle

VSM comprises of a water cooled electromagnet and a power supply for the generation of constant magnetic field and to magnetize the sample. The sample to be studied is first placed in a DC uniform magnetic field. Depending on the magnetic nature of the material, this constant applied magnetic field magnetizes the sample by aligning the magnetic domains or the individual magnetic spins. Sample is then placed in a sample holder rod which is attached to a vibration exciter (with an angle indicator); the end of it hangs down in between the pole pieces. The function of the exciter is to move the sample up and down at a set frequency. It consists of an angle indicator through which the sample rod can be rotated for obtaining the desired orientation of the sample w.r.t constant magnetic field. Knobs are also present for controlling x, y, and z positions of the sample. The sample is then vibrated along a certain axis, mainly z-axis with small amplitude. The motion of the sample causes a disturbance in the uniform field with the

same frequency as that of the sample vibration due to its magnetic dipole moment. This disturbance changes as a function of time and is converted to electrical voltage by a set of induction (pickup or sensor) coils, according to Faraday's law of induction. This corresponds to the magnetization of the sample at that magnetic field intensity. The pickup coils consist of 2 or 4 identical coils which have the same axis as that of the applied magnetic field. Their separation and geometry are calculated so that the sample displacement takes place in a constant field gradient (this is a purely fictitious field, as no current is fed to the coils) [122].

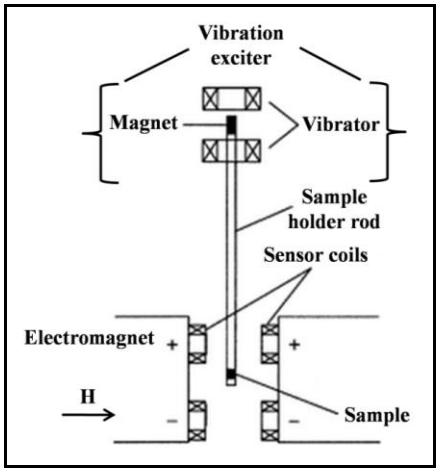

Figure 2.16 Block diagram depicting the working principle of a vibrating sample magnetometer [122]

The induced voltage is amplified and measured with a lock-in amplifier. It is tuned to pickup only signals at the vibrating frequency and practically rejects all the other frequencies. This eliminates noise from the environment. The final plot along with values of the magnetic parameters can be received on a computer interface. Fig. 2.16 shows the block diagram depicting the working principle of vibrating sample magnetometer [122]. Fig. 2.17 shows the pictorial view of a VSM.

Figure 2.17 Pictorial view of a VSM [123]

2.2.7.3 Sample preparation

For VSM characterization, powdered sample with weight 3 mg to 0.1 g is required for obtaining the results.

2.2.7.4 Information from VSM

- It is used to obtain the M-H curve of a material and to measure the magnetic parameters such as magnetic saturation, retentivity, coercivity and magnetic squareness.

In the present thesis, M-H curves of the synthesized nanoparticles and nanocomposites were recorded on VSM: Princeton Applied Research Model 151/155.

2.2.8 Cytotoxicity analysis

2.2.8.1 MTT assay

MTT (3-(4, 5-Dimethylthiazol-2-yl)-2, 5-diphenyltetrazolium bromide, a yellow tetrazole) assay is a laboratory test and standard colorimetric assay for measuring the activity of

enzymes. MTT is reduced to purple formazan in living cells by mitochondrial dehydrogenases, as shown in fig. 2.18 [124]. It is mainly used to determine cytotoxicity of potential medicinal agents and other toxic materials, since interaction of those agents with cells would result in cell toxicity and therefore metabolic dysfunction, leading to decreased performance in the assay.

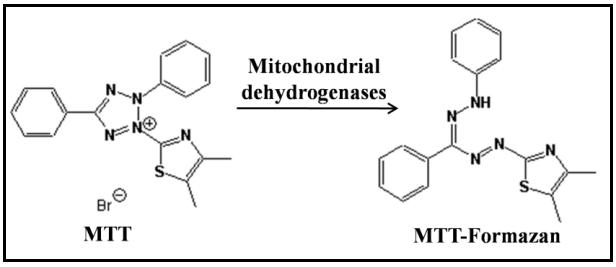

Figure 2.18 Metabolism of MTT-dye to MTT-formazan crystals by mitochondrial dehydrogenases of living cells [124]

Basically, MTT is a membrane permeable dye; it gets metabolized to dark-blue crystals of formazan owing to the mitochondrial dehydrogenases in living cells. These crystals are impermeable to cell membranes and have the tendency to accumulate in proliferating, undamaged cells. After the accumulation, occurs the lysis of the cell along with solubilization of the formazan crystals. Then, the optical density (OD) of the dye is quantified using a multiwell-spectrophotometer (ELISA reader) at 550 nm. The number of proliferating cells is directly proportional to the development of dark-blue crystals which is quantified by means of a standard calibration [124] and this is relative to the number of living cells.

Chapter – 3

CALCIUM FERRITE NANOCOMPOSITES

Chapter 3

In the present chapter, experimental procedures for synthesizing calcium ferrite nanoparticles and their surface coating with PEG and silica have been explained. Their structural, morphological, thermal and magnetic properties along with cytotoxicity have been discussed.

Following are the publications corresponding to calcium ferrite nanoparticles and nanocomposites. Some of the results have been discussed in the present chapter.

1. Lavanya Khanna, N. K. Verma, Size-dependent magnetic properties of calcium ferrite nanoparticles, Journal of Magnetism and Magnetic Materials, 336 (2013) 1–7.

2. Lavanya Khanna, N. K. Verma, PEG/$CaFe_2O_4$ nanocomposite: Structural, morphological, magnetic and thermal analyses, Physica B, 427 (2013) 68–75.

3. Lavanya Khanna, N. K. Verma, Synthesis, characterization and invitro cytotoxicity study of calcium ferrite nanoparticles, Materials Science in Semiconductor Processing, 16 (2013) 1842-1848.

4. Lavanya Khanna, N. K. Verma, Biocompatibility and superparamagnetism in novel silica/$CaFe_2O_4$ nanocomposite, Materials Letters, 128C (2014) 376-379.

3.1 Experimental procedure

3.1.1 Synthesis of calcium ferrite nanoparticles

Conventional sol–gel method was employed for the synthesis of calcium ferrite nanoparticles (Ca-ferrite NPs), as shown in fig. 3.1 [75]. Metallic citrate polymerization using ethylene glycol is the basis of this process [75].

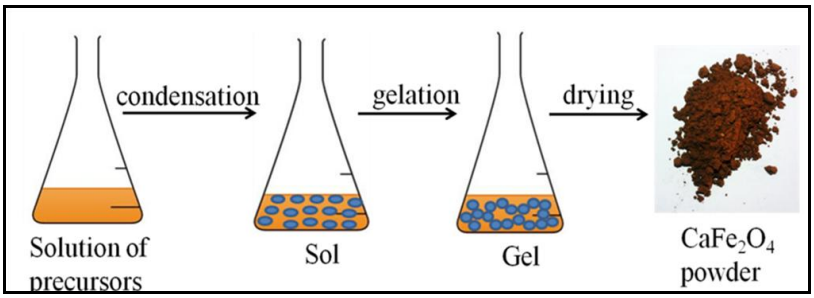

Figure 3.1 Schematic representation of synthesis of calcium ferrite nanoparticles

Briefly, 1M solution of calcium nitrate and 2M solution of ferric nitrate were mixed. Metal nitrates serve dual role of being a soluble cation source and the oxidant [125]. To this mixture, 2 M citric acid solution was added along with 5–7 ml of ethylene glycol. Citric acid provides fuel for the combustion, serves as a chelating agent to form complexes with metal ions and prevents the precipitation of hydroxilated compounds [125]. Also, it acts as non-polymeric filler for size modification and porosity control of nano powders [126]. Citric acid can be removed by either heat treatment or thermal decomposition, without affecting the properties of the material [126]. The solution was constantly magnetically stirred at 80–90°C. The viscous gel began frothing after the removal of water molecules from the mixture. During evaporation, the solution became viscous and finally formed a very viscous brown gel. On further heating dried gel was formed, it continued to burn in a self propagating combustion manner until all the

gel was completely converted to a brown coloured powder, which also indicated the completion of auto-ignition process. The decomposition reaction would not stop until the whole citrate complex was consumed. The formation of sol, gel, dried gel and finally powder, on heating and stirring was obtained. The obtained powder was thoroughly washed with ethanol by centrifugation at 2000 rpm; it was dried overnight in vacuum oven at 60ºC. The dried powder was grinded in pestle and mortar to obtain uniform fine powder. The dried powder was further calcined at 300°C (Ca3), 500°C (Ca5), 700°C (Ca7), and 900°C (Ca9), for 3 h each. Following is the chemical reaction:

$$9Ca(NO_3)_2.4H_2O + 18Fe(NO_3)_3.9H_2O + 20C_6H_8O_7.H_2O \rightarrow 9CaFe_2O_4 + 298H_2O + 120CO_2\,(g) + 36N_2\,(g)$$

3.1.2 Results and discussion

3.1.2.1 Structural analysis

The room temperature XRD patterns were collected on X-ray Diffractometer in the 2θ angle range of 10-70º.

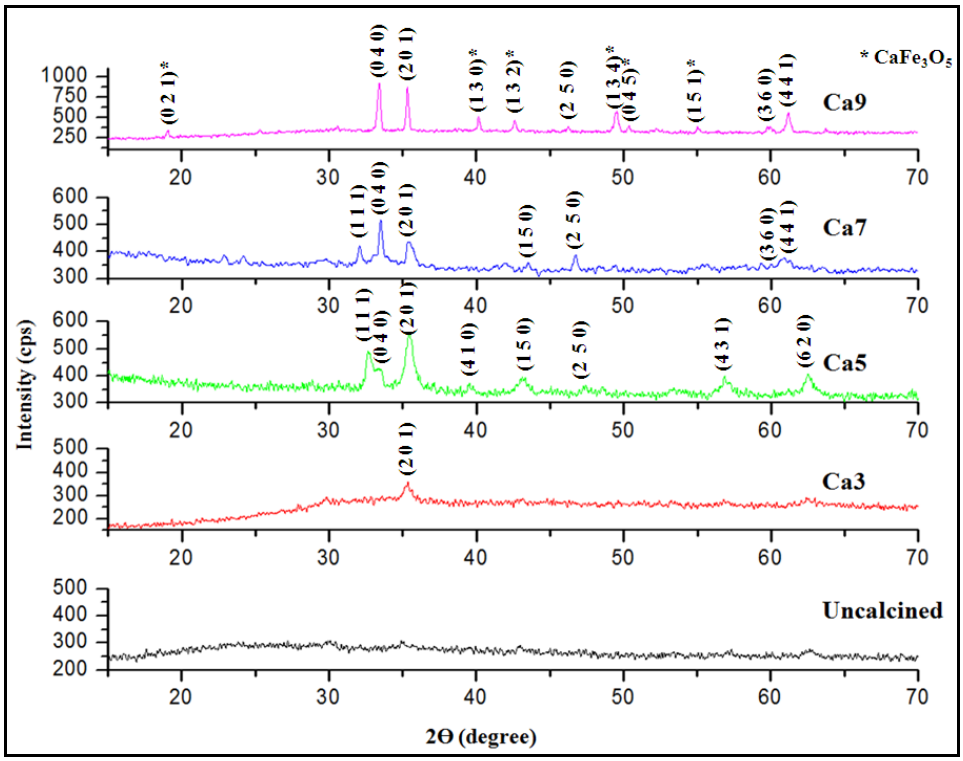

Figure 3.2 XRD patterns of uncalcined and calcined Ca-ferrite NPs

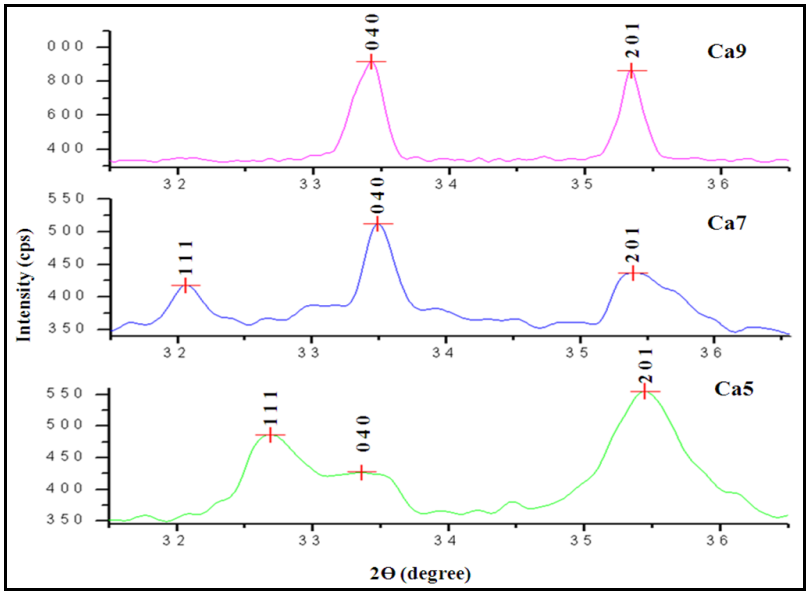

Figure 3.3 Enlarged XRD patterns of the calcined samples in the angle range of 30-40°

Fig. 3.2 shows the X-ray patterns of the uncalcined (as synthesized) and calcined nanoparticles (Ca3, Ca5, Ca7, Ca9). The uncalcined particles exhibited amorphous nature. No diffraction peaks were observed, depicting the lack of crystallinity in the uncalcined particles. Even on calcining at 300ºC, complete crystallinity was not obtained, as depicted by the X-ray pattern of Ca3 sample, only one peak at 35.3° was observed. The amorphous nature of uncalcined and Ca3 sample is also confirmed by the TEM micrograph in figs. 3.4(a, b) The XRD patterns of Ca5, Ca7, Ca9 showed that all the calcined samples are crystalline in nature. On calcining the nanoparticles at 500°C, spherical formation of nanoparticles was observed; this is also confirmed by the TEM micrograph in figs. 3.4(c, d). In the XRD pattern, all the peaks for Ca5 are well matched to the orthorhombic structure (space group: *Pnam* (62), JCPDS Card No. 72-1199) of $CaFe_2O_4$. Three prominent diffraction peaks at 32.1º, 33.4º and 35.4º corresponding to (1 1 1), (0 4 0) and (2 0 1) were observed. The crystallite size for the most intense peak (2 0 1) in Ca3 and Ca5 samples was calculated using Debye Scherrer formula, Eq. (3.1).

$$d = \frac{k\lambda}{\beta cos\theta} \tag{3.1}$$

where d is the crystallite size, k =0.9 is a correction factor, β is the full width half maximum (FWHM) of the most intense peak (2 0 1), λ is the wavelength of Cu target which is equal to 1.5406 Å and θ is the Bragg angle. The average crystallite size for Ca3 and Ca5 was calculated to be 11 nm and 13 nm, respectively. The increase in the calcination temperature resulted in increase in the size. Thermal annealing induces coalescence of small grains by grain boundary diffusion which causes grain growth and hence size of the nanoparticles increases [127]. Further, on increasing the calcination temperature to 700ºC, the morphology of the nanoparticles changed from spherical to capsule like. As observed in the TEM micrograph (fig.

3.5(a)), mixed morphology comprising of spherical nanoparticles as well as capsule were found to co-exist. The three prominent diffraction peaks at 32.1º, 33.4º and 35.4º corresponding to (1 1 1), (0 4 0) and (2 0 1), similar to the peaks in case of Ca5 were observed. Comparing the X-ray patterns for Ca5 and Ca7, as shown in fig. 3.3, it was observed that the peak corresponding to (1 1 1) gets shortened on increasing the temperature while the peak corresponding to (0 4 0) becomes sharper. This suggests that the preferred orientation for growth of the nanocapsules is along the (0 4 0) peak along b-axis. This can be considered as an intermediate state where the spherical particles (formed at 500°C) grow as capsules. The rise of (0 4 0) peak intensity with slight shift in position and variation in (2 0 1) peak can be attributed to better crystallinity with more relaxation caused by annealing and change in morphology, respectively.

Further calcination of the nanoparticles at 900ºC resulted in formation of nanocapsules; no spherical nanoparticles were formed at this temperature. In the XRD pattern, all the peaks for Ca9 are well matched to the orthorhombic structure (space group: *Pnam* (62), JCPDS Card No. 72-1199) of $CaFe_2O_4$. The additional peaks (marked as * in fig. 3.2) in the XRD pattern have been identified as $CaFe_3O_5$ with orthorhombic phase (space group: *Cmcm* (63), JCPDS Card No. 72-0890). The rise of (0 4 0) peak intensity and slight shift in its position can be attributed to better crystallinity with more relaxation. The X-ray pattern, in fig. 3.3 reveals that at 900°C, the peak corresponding to (1 1 1) completely disappeared and the peak corresponding to (0 4 0) became sharper and intense, suggesting that the growth of the particles is along b-axis. On increasing the calcination temperature, calcium ferrite crystallite gains enough energy and tends to orient themselves along (0 4 0) peak as it possesses highest atomic packing density and minimum surface energy, resulting in increased aspect ratio with temperature.

3.1.2.2 Morphological analysis

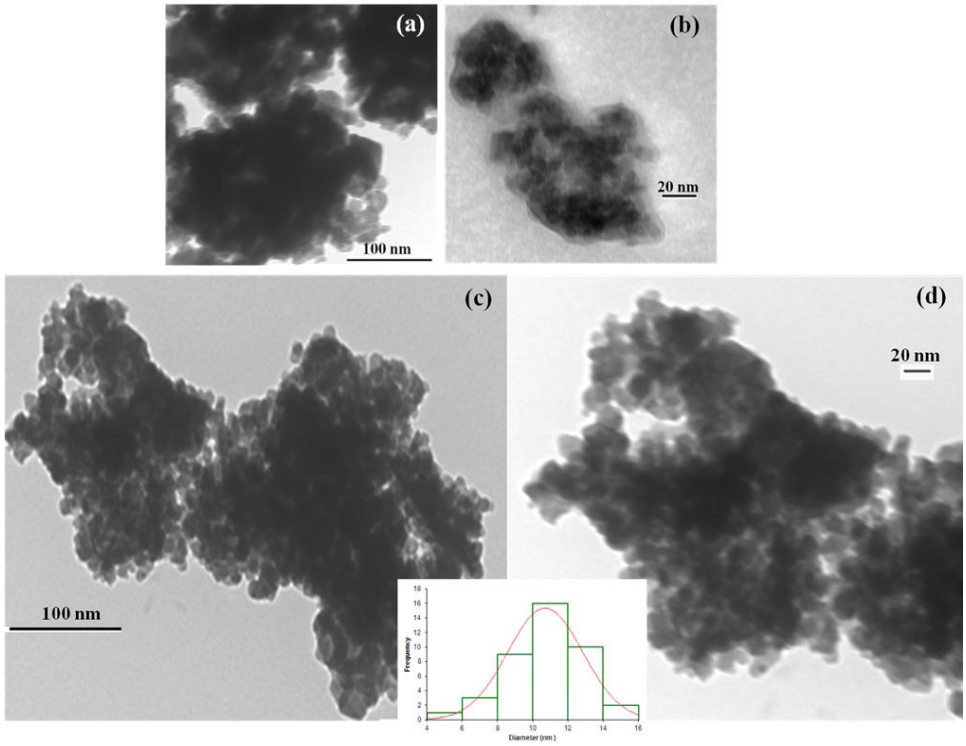

Figure 3.4 TEM micrograph of (a) uncalcined Ca-ferrite, calcined at (b) 300°C (c, d) 500°C

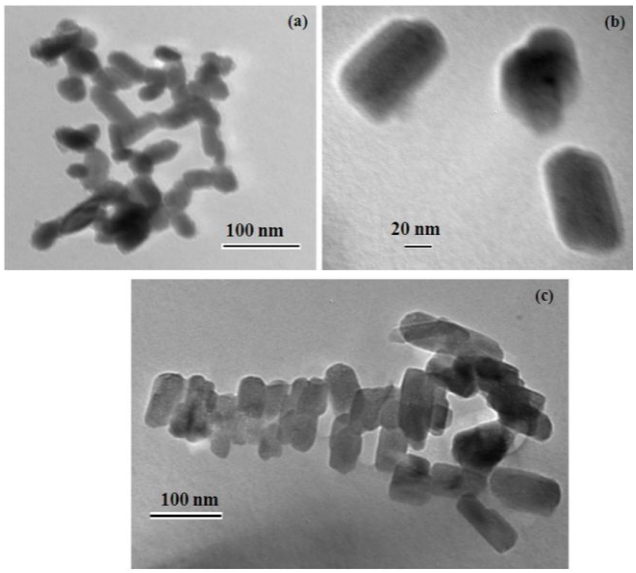

Figure 3.5 TEM micrograph of Ca-ferrite NPs calcined at (a) 700°C (b, c) 900°C

TEM micrographs of the uncalcined nanoparticles and nanoparticles calcined at 300°C exhibit an amorphous nature, as shown in figs. 3.4(a, b). The amorphous nature is also confirmed from the XRD pattern as discussed earlier. TEM micrographs in figs. 3.4(c, d), reveal that the synthesized Ca-ferrite NPs calcined at 500ºC are of spherical shape with diameter in the narrow size range of 4-16 nm, as depicted by the size distribution of the nanoparticles in the histogram. The magnetic interaction between the nanocrystallites and high surface energy of the nanoparticles renders them to be in agglomerated form. Fig. 3.5(a) shows the mixed morphology of spherical and capsule like formation, the growth of capsules from spherical morphology can be well observed, the mean width and mean length of capsules were found to 25 and 41 nm. TEM micrographs in figs. 3.5(b, c) illustrate the morphology of the synthesized Ca-ferrite NPs calcined at 900ºC to be like capsules, aptly referred to as nano-capsules. The mean width and mean length of nano capsules was found to be 38 nm and 82 nm. This increase is probably due to the presence of nano-metric particles and therefore more reactivates, favouring coalescence [75] and eventually forming larger nanocapsules. Table 3.1 summarizes the morphology and particle size obtained at different calcination temperatures.

Table 3.1 Morphology and particle size obtained at different calcination temperatures

Temperature (°C)	**Morphology and Size**
300	Spherical nanoparticles-11 nm
500	Spherical nanoparticles-13 nm
700	Mixed morphology (Nanocapsules with mean width - 25nm, mean length - 41 nm)
900	Nanocapsules - mean width - 38 nm , mean length - 82 nm

3.1.2.3 Magnetic analysis

The magnetic analysis of all the samples was performed on VSM, as discussed below.

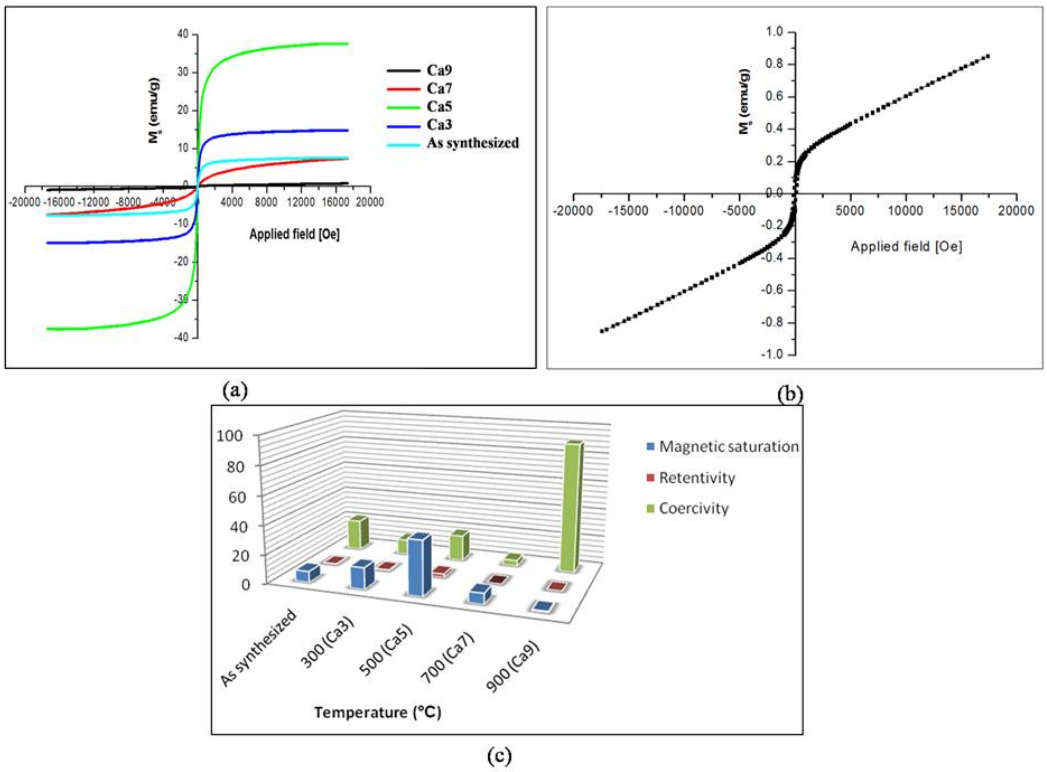

Figure 3.6 (a) M-H curves obtained for all the samples (b) M-H curve of Ca9 (c) Comparison of the hysteresis parameters for all the samples

Fig. 3.6(a) shows the M-H curve obtained for calcium ferrite nanoparticles at all the temperatures. The notable features have been observed at two temperatures wherein, the magnetic saturation was maximum for the nanoparticles calcined at 500ºC (Ca5) and minimum for the nanoparticles calcined at 900ºC (Ca9). The superparamagnetic behavior is reflected in the low M_R/M_S ratio and in the small H_C values [17]. The squareness value for non-interacting superparamagnetic particles is 0.5 [58], in the case of interacting superparamagnetic particles the dipolar interactions reduce both the magnetic squareness (M_R/M_S ratio) and coercivity (H_C)

values due to demagnetizing effect [58, 59]. Magnetic squareness value pertaining to superparamagnetic behaviour is 0.1, i.e. it loses greater than 90% of its magnetism when the applied magnetic field is removed [60, 128]. Ca5 possesses a magnetic squareness of 0.061, which is less than 0.10. Therefore, in the light of the above, it exhibits the characteristic feature of interacting superparamagnetic particles. The hysteresis loop of the nanoparticles calcined at 900ºC, as shown in fig. 3.6 (b) corresponds to be a mixture of ferrimagnetic and paramagnetic grains [129], producing hysteresis loop that is slope positive at low and high fields. The loop is slope positive for paramagnetic grains, in contrast to slopes for diamagnetic materials. The sudden drop in the magnetic saturation value in Ca9 can be possibly attributed to the dominance of paramagnetic grains. Fig. 3.6(c) compares the nagnetic saturation, retentivity and coercivity values, for as synthesized particles alongwith the values obtained at all the temperatures. It can be well observed that Ca5 sample has the highest magnetic saturation value as compared to the other samples and Ca9 has the highest coercivity value.

As observed, the desired features of superparamagnetism (with highest magnetic saturation) and nano size were obtained at 500°C. For further optimization, the sample was also calcined at 550°C and 600°C. The sample calcined at 600°C exhibited nanocapsules formation similar to Ca7 sample. The morphological, structural and magnetic properties of the nanoparticles calcined at 550°C were akin to Ca5; therefore further investigations were carried out on it. Following are the results obtained.

3.2 Results and discussion

3.2.1 Structural analysis

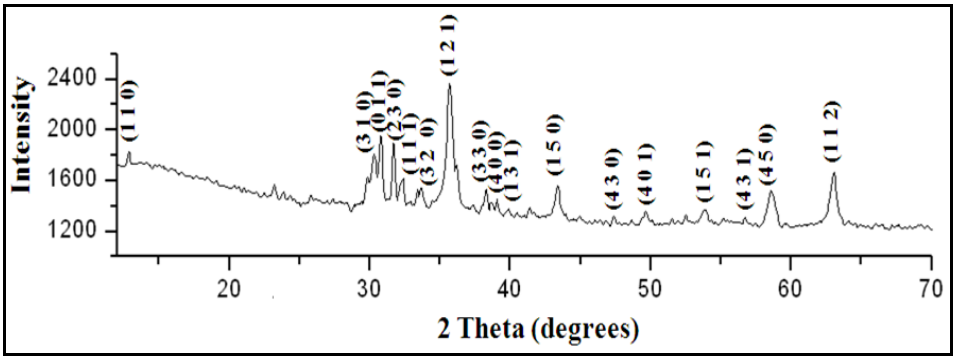

Figure 3.7 XRD pattern of calcium ferrite nanoparticles

Fig. 3.7 shows the XRD pattern of calcium ferrite nanoparticles; all the peaks are well matched to the orthorhombic structure (JCPDS Card No. 72-1199) of $CaFe_2O_4$. The broadening of the diffraction peaks depicts the formation of nanocrystallites. Table 3.2 shows the theoretical and calculated values of the unit cell parameters.

Table 3.2 Theoretical and calculated values of the unit cell parameters for calcium ferrite nanoparticles

$CaFe_2O_4$				
		Theoretical	Calculated	Difference
Unit cell parameters	A	9.228	9.862	0.634
	B	10.70	10.31	0.39
	C	3.018	3.033	0.014

3.2.2 Thermal analysis

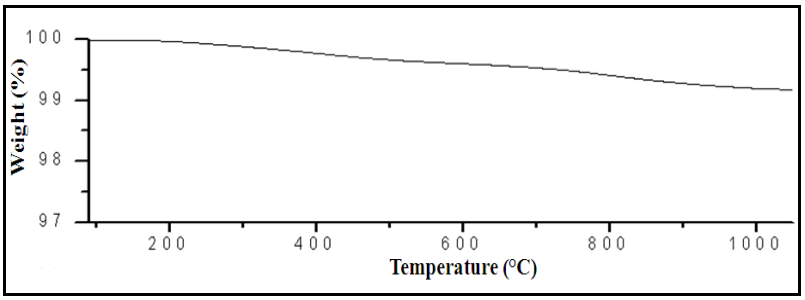

Figure 3.8 TGA pattern of calcium ferrite nanoparticles

The thermal graph of the synthesized calcium ferrite nanoparticles, fig. 3.8, reveals its thermal stability, as no significant weight loss has been observed with temperature. This ensures the purity of the synthesized nanoparticles as no mass loss and peak pertaining to any organic impurity is present. This also ascertains the completion of the synthesis process.

3.2.3 FTIR analysis

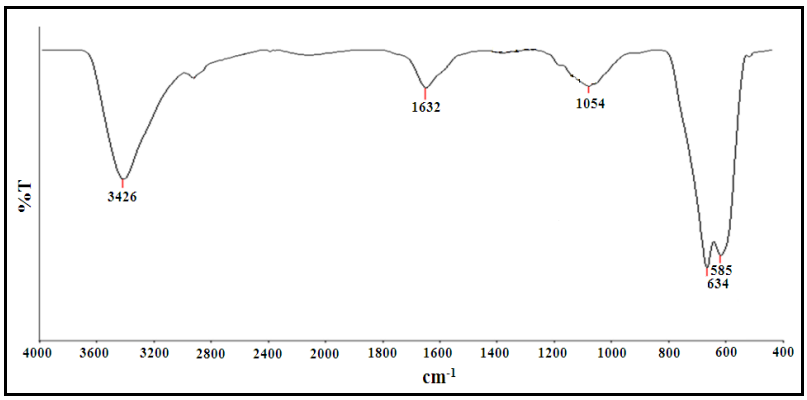

Figure 3.9 FTIR spectrum of calcium ferrite nanoparticles

FTIR spectrum of calcium ferrite nanoparticles in fig.3.9 exhibits a broad stretch at 3426 cm^{-1} and 1632 cm^{-1} due to O-H stretching and bending vibrations, respectively [116]. The band

at 1054 cm^{-1} corresponds to metal-alloy (Fe-Ca) [61] and bands at 634, 585 cm^{-1} are attributed to Fe-O bonds due to the prescence of ferrite skeleton [61]. No bands related to any impurity/unreacted precursor are present. Table 3.3 gives the description of the obtained bands.

Table 3.3 Description of FTIR spectrum of calcium ferrite nanoparticles

Calcium ferrite nanoparticles	IR band (cm^{-1})	Description
	3426	*v*(OH) stretching
	1632	*v*(OH) bending
	1054	*v* (Fe-Ca) stretching
	634	*v*(Fe-O) stretching
	585	*v*(Fe-O) stretching

In figs 3.8 and 3.9, no detection corresponding to traces of any organic impurity or unreacted precursors have been observed. This ensures the completion of the reaction process and ascertains that the obtained toxicity is solely due to synthesized nanoparticles. Toxicity is very sensitive to impurity and therefore it becomes imperative to ensure that the sample is free from any impurity.

3.2.4 Morphological analysis

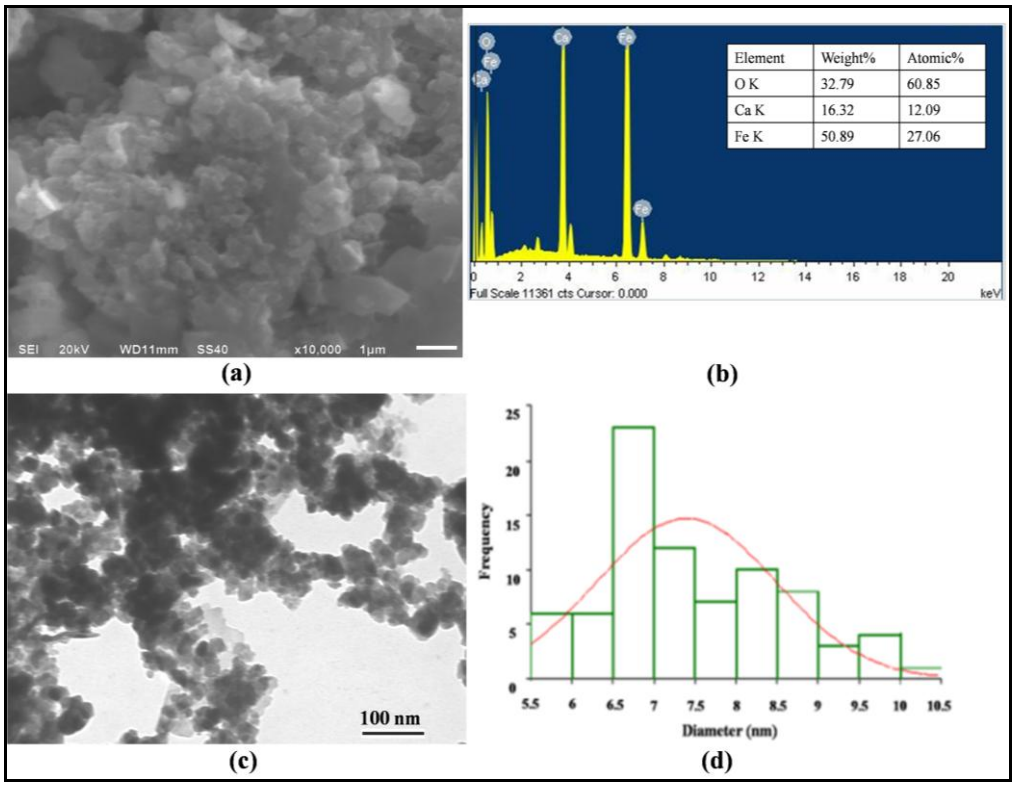

Figure 3.10 (a, b) SEM micrograph with EDAX spectrum (c, d) TEM micrograph along with histogram of calcium ferrite nanoparticles

SEM and TEM studies were performed to understand the details of the morphology of calcium ferrite nanoparticles. Fig. 3.10(a) shows the agglomerated form of synthesized calcium ferrite nanoparticles due to the magnetic interactions and high surface energy of the nanoparticles. Fig. 3.10(b) shows the EDAX spectrum, confirming the presence of Ca, Fe and O elements along with their observed atomic% and weight % values. TEM micrograph in fig. 3.10(c) reveals spherical formation of the nanoparticles with size distribution of ~ 5-11 nm, as depicted by the histogram in fig. 3.10(d).

3.2.5 Magnetic analysis

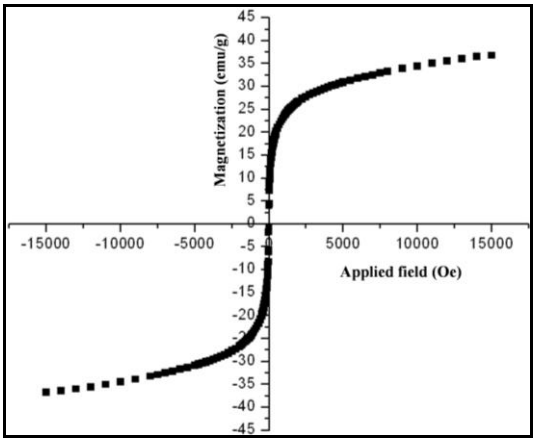

Figure 3.11 M-H curve of calcium ferrite nanoparticles

The magnetic response of calcium ferrite nanoparticles was studied by VSM, as shown in fig. 3.11. In the M-H curve, the synthesized nanoparticles exhibit superparamagnetic behaviour, with magnetic saturation (M_s), remanent magnetization (M_R) and squareness (M_R/M_S ratio) values of 36.76emu/g, 0.24emu/g and 0.006, respectively. Less squareness and coercivity values determine superparamagnetic behavior [17]. The squareness value for non-interacting superparamagnetic particles is 0.5 [58], in the case of interacting superparamagnetic particles the dipolar interactions reduce both the magnetic squareness (M_R/M_S ratio) and coercivity (H_C) values due to demagnetizing effect [58, 59]. Magnetic squareness value pertaining to superparamagnetic behaviour is 0.1, i.e. more than 90% of its magnetism is lost on removal of the applied magnetic field [60] and the squareness value of calcium ferrite nanoparticles is 0.006. Therefore, it exhibits superparamagnetism.

3.2.6 In vitro cytotoxicity analysis

3.2.6.1 Experimental procedure - MTT assay

To investigate the biocompatibility of the synthesized nanoparticles, in vitro test was conducted on Jurkat cells. Jurkat cells are well-established immortalized cancer cell-line of T lymphocyte cells which are used for studying acute T cell leukaemia, T cell signalling and expression of various receptors susceptible to viral entry. This cell-line has been widely used in cytotoxicity assays for determining toxic effect of magnetic nanoparticles on the cells [130-133]. The viability of T cell lines (Jurkat cells) incubated with calcium ferrite nanoparticles at different concentrations was investigated by MTT (3-(4, 5- Dimethylthiazol-2-yl)-2, 5-diphenyltetrazolium bromide, a tetrazole) colorimetric assay. Cells were cultured on tissue culture polystyrene falcon flasks in RPMI-1640 supplemented by 10% FCS (Fetal Calf Serum) at 37ºC in 5 % CO_2. This solution was then centrifuged at 1200 rpm at 4ºC for 5 minute to separate dead cells. The cells were trypsinized and counted on haemocytometer. After trypsinization, the cells in media were placed in 96-well tissue culture flat bottom plate at a density of 1.5 X 10^4 cells per well. Required concentration (5, 25, 50, 100, 250, 500 μg/ml) of nanoparticles was added to the wells. It was then incubated for 48 hour in CO_2 incubator at 37ºC in 5% CO_2. Controls were carried out consisting of growing cells without any treatment. After 48 hour, the cell suspension was removed from each well and 20 μl MTT solution was added; it was incubated for 4-5 hour. Viable cells have the ability to reduce yellow MTT to insoluble purple formazan, this reduction takes place only when mitochondrial reductase enzymes are active, and therefore conversion can be directly related to the number of viable (living) cells. Reaction was stopped by addition of stop lysis solution (20% SDS in 50%

dimethyl formamide + 50% distilled water). Plates were further incubated for 1 hour and absorbance was recorded at 570 nm on ELISA Plate Reader. Mean and Standard deviation was obtained from 5 replicates. Cell viability was calculated by the following formula, Eq. (3.2):

$$\text{Cell viability } (\%) = \frac{I_{sample}}{I_{control}} \text{ X } 100 \qquad (3.2)$$

I_{sample} is the absorbance of nanoparticles treated wells and $I_{control}$ is the absorbance of control wells without nanoparticles treatment [38]. The statistical analysis of the experimental data of the synthesized nanoparticles was done by student's paired t- test.

3.2.6.2 Cytotoxicity analysis

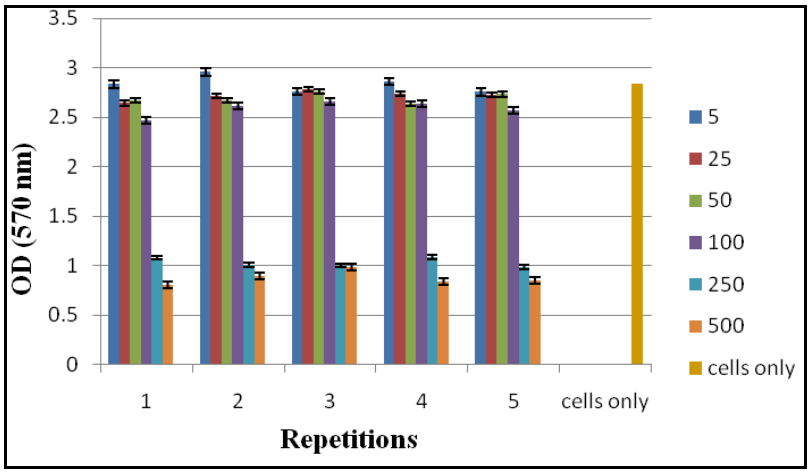

Figure 3.12 Optical Density (OD) at 570 nm of all repetitions at all concentrations

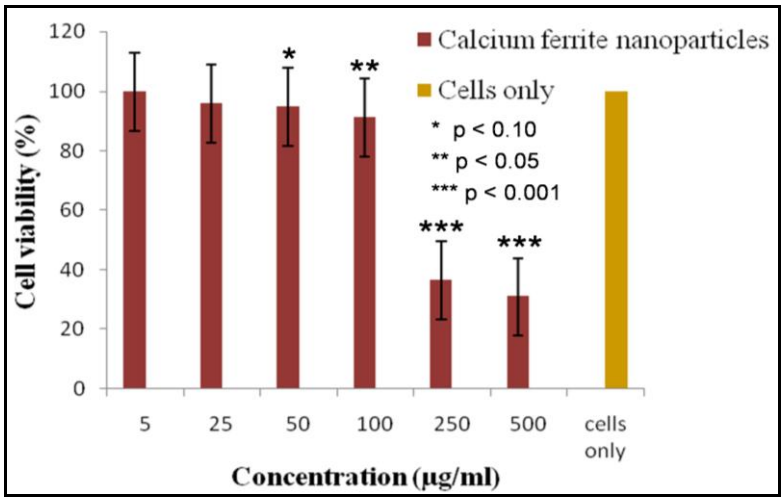

Figure 3.13 Mean cell viability (%) as determined by MTT assay, with values presented as *p<0.10, **p<0.05, ***p<0.001 compared with untreated cells (dependent student's t-test)

Fig. 3.12 exhibits the dose dependent reduction in cell viability of the synthesized calcium ferrite nanoparticles. The cell viabilities at 5, 25, 50, 100, 250, 500 µg/ml, calculated according to Eq. 3.2 are 99.7%, 95.7%, 94.7%, 91.1%, 36.3%, 30.8%, respectively. The statistical analysis using student's dependent t-test has also been calculated, fig. 3.13, in order to understand the effect of synthesized nanoparticles on the cells [134]. The cell viability is greater than 90% at concentration below 250µg/ml suggesting that the nanoparticles are non-toxic to the cells, but at a higher concentration, a significant toxicity causes cell death. It is important to understand the interaction of nanoparticles with the cell; the nanoparticles first adhere to the surface of the cells, then are internalized by endocytosis and finally get accumulated in digestive vacuoles [70]. The cytotoxicity at higher concentrations is therefore very likely caused by particle overload to the cells [70]. What the biological cell or barrier actually "sees" on interacting with magnetic nanoparticles is highly associated to the protein corona [135]. The nanoparticle-protein interaction is a key issue for defining the toxicity of magnetic nanoparticles;

the unfavourable changes in the protein configuration, the denaturation of the proteins on interaction could cause the exposure of new antigenic sites which may instigate a new immune response [135]. As observed in the FTIR spectrum and thermal analysis, the synthesized calcium ferrite nanoparticles are free from any organic impurity and unreacted precursors, therefore it can be ascertained that the toxicity exhibited is solely due to the synthesized nanoparticles.

3.3 PEG coated calcium ferrite nanoparticles

3.3.1 Experimental procedure

To synthesize PEG coated calcium ferrite nanoparticles, the calcined nanoparticles were mixed with the PEG-1500 solution with the concentration of 0.01g/ml, followed by addition of a certain amount of ammonia solution until the pH of the solution reached 11. After continuous stirring, a homogeneous mixture was obtained. The mixture was poured into a Teflon lined stainless-steel autoclave (50ml), kept at 140°C for 12 hour and then cooled to room temperature naturally [136]. The obtained product was washed several times with ethanol; finally it was dried overnight in a vacuum oven at 60°C. The dried powder was grinded in pestle and mortar to obtain uniform fine powder.

3.3.2 Results and discussion

3.3.2.1 Structural analysis

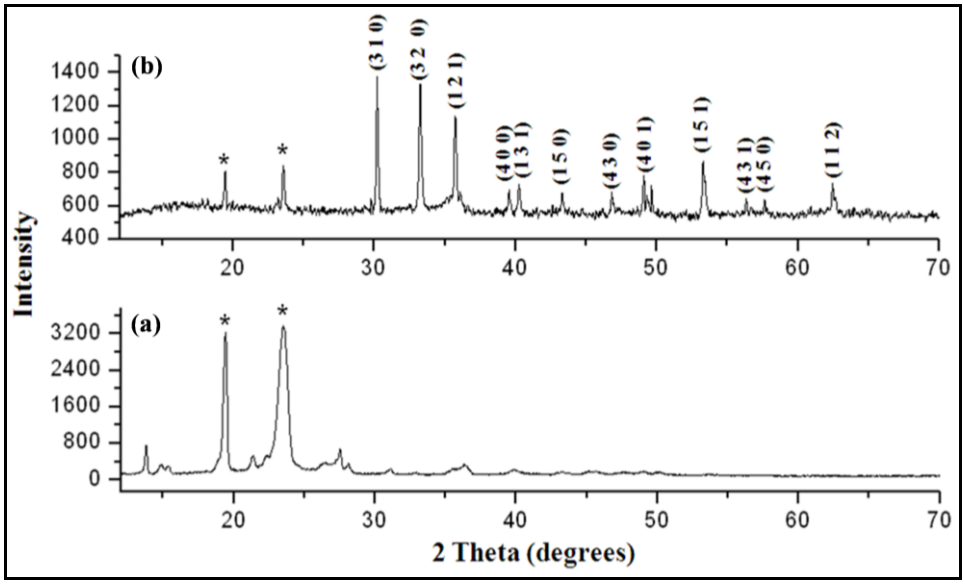

Figure 3.14 XRD patterns of (a) PEG and (b) PEG coated calcium ferrite nanoparticles

XRD pattern of PEG in fig. 3.14(a) reveals two distinct peaks at 19° and 23° (marked as *), characteristic of its crystalline nature. Fig. 3.14(b) shows the XRD pattern of PEG coated calcium ferrite nanoparticles, two peaks at 19° and 23°, characteristic of PEG have been observed (marked as *), confirming the presence of PEG. All the other peaks are attributed to the formation of orthorhombic structure (JCPDS Card No. 72-1199) of $CaFe_2O_4$. The sharpening of the peaks is due to the increase in the size after PEG coating, this is also confirmed by the TEM analysis. Table 3.4 gives the theoretical and calculated values of the unit cell parameters.

Table 3.4 Theoretical and calculated values of the unit cell parameters for PEG coated calcium ferrite nanoparticles

PEG coated $CaFe_2O_4$				
		Theoretical	Calculated	Difference
Unit cell parameters	a	9.228	9.483	0.225
	b	10.70	10.22	0.48
	c	3.018	3.024	0.006

3.3.2.2 Thermal analysis

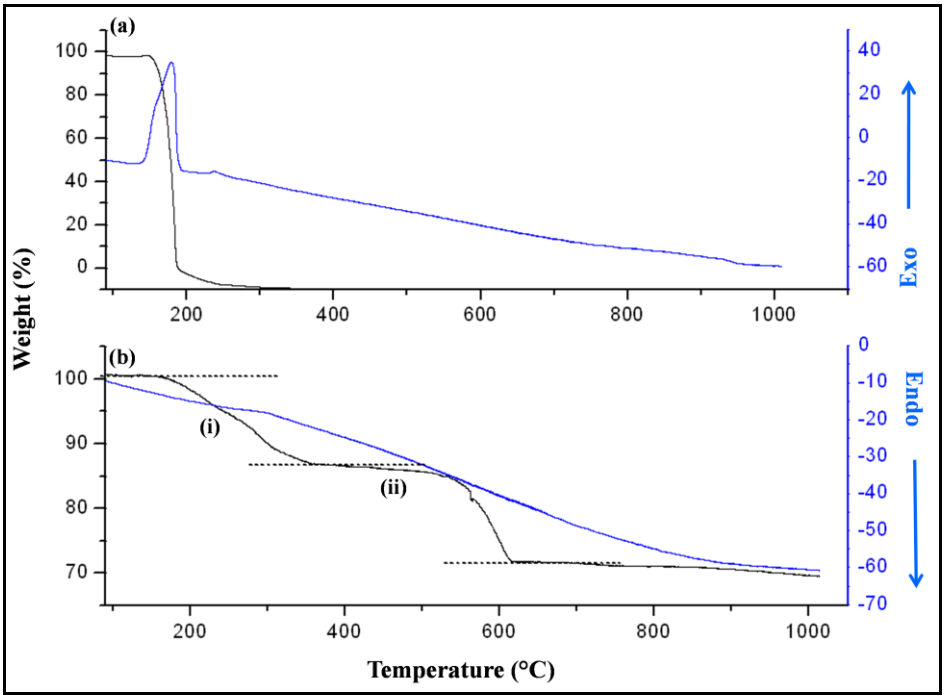

Figure 3.15 TGA and DTA patterns of (a) polymer PEG and (b) PEG coated calcium ferrite nanoparticles

Thermal stability of PEG polymer and its presence in the final product has been studied using thermal analysis results. In fig. 3.15(a), the thermal analysis of polymer PEG shows that the complete thermal decomposition is a one step process which starts at about 142°C and it gets

completely over by 184°C. In the DTA curve, peak at ~ 180°C denotes the exothermic event associated with this loss. The decomposition was more complex for PEG coated calcium ferrite nanoparticles. As shown in fig. 3.15(b), two distinct weight loss regions can be identified: i) 134-384 °C, ii) 384-618 °C, denoted by black dashed lines. It should be noted that the weight of the sample greater than 100% is the result of N_2 absorption during the measurement [137]. The first loss (~ 14%) corresponds to the release of the structural water and decomposition of part of the PEG molecules, possibly loss of organic hydrogen [138], while the second loss (~15%) is caused by the decomposition of the residual polymer. No significant peak has been observed in the DTA curve. It is well-evident that the temperature at which the weight of the PEG polymer drastically decreases is shifted to high temperature suggesting that the thermal stability of PEG is enhanced due to the formation of covalent bonds with calcium ferrite nanoparticles.

3.3.2.3 FTIR analysis

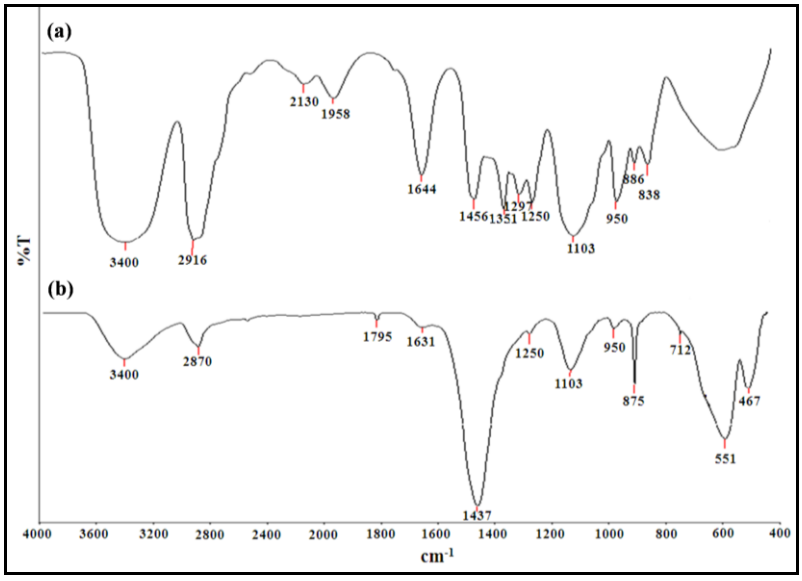

Figure 3.16 FTIR spectra of (a) PEG and (b) PEG coated calcium ferrite nanoparticles

In the FTIR spectrum of PEG polymer, fig. 3.16(a), the broad bands at 3400 cm^{-1} and 1644 cm^{-1} are assigned to the O-H stretching vibrations of the free or absorbed water and O-H bending vibrations, respectively [116, 138]. The bands at 2916, 1456, 1351 and 950 cm^{-1} correspond to vibrational modes of CH_2 group in PEG, i.e. asymmetrical stretching, in plane bending (scissoring), out of plane bending (wagging) and out of plane bending vibrations, respectively [30, 138]. The bands at 1297, 1250 cm^{-1} result from the bending vibrations of O-H bond and out of plane bending vibrations (twisting) of C-H bond of – CH_2-OH group of PEG [116]. A weak band at 2130 cm^{-1} is assigned to the combination frequency of (CH + CC) [139]. The small band at 1958 cm^{-1} is due to C-O bond [140]. The C-O-C ether stretch band at 1103 cm^{-1} is attributed to –CH_2-O-CH_2- group in PEG [32, 38]. The bands at 886 and 838 cm^{-1} are attributed to C-C stretching vibrations [141].

In the FTIR spectrum of PEG coated calcium ferrite nanoparticles, fig. 3.16(b), the broad stretch at 3400 cm^{-1} and 1631 cm^{-1} is due to O-H stretching and bending vibrations [116, 138]. The band relative to molecular water centered at 1644 cm^{-1} in PEG, is formed at a slighter lower wave number in PEG coated calcium ferrite nanoparticles, implying that PEG has led to partial loss of water molecules [138]. The sharp C-H symmetrical stretch at 2870 cm^{-1}, in plane bending (scissoring) C-H stretch at 1437 cm^{-1}, C-H out of plane bending vibration at 950 cm^{-1} , bending vibrations of O-H and C-H (twisting) stretch at 1250 cm^{-1} and a sharp C-O-C ether stretch at 1103 cm^{-1} clearly confirms the prescence of PEG on calcium ferrite nanoparticles. The bands due to C-H vibrational modes and bands due to water are strongly reudced in intensity due to dehydroxilation and oxidation of the organic moieties [138]. A new component at 1795 cm^{-1} appears, assignable to stretching vibration of carbonyl species due to thermo-oxidative degradation process [138, 142]. In the lower region, the bands at 875, 712 cm^{-1} are attributed to

O-Fe-O , Fe-OH bonds and bands at 551, 467 cm^{-1} correspond to Fe-O bond [61]. Table 3.5 shows the description of the bands for PEG and PEG coated calcium ferrite nanoparticles.

Table 3.5 Description of FTIR spectra of PEG and PEG coated calcium ferrite nanoparticles

Samples	IR band (cm^{-1})	Description
PEG	3400	ν(OH) stretching
	2916	ν_{as} (CH_2) stretching
	2130	ν (CH + CC)
	1958	ν(CO) stretching
	1644	ν(OH) bending
	1456	δ_s(CH_2) scissoring
	1351	w(CH_2) wagging
	1297, 1250	ν(OH) bending and τ(CH_2) twisting
	1103	ν(C-O-C) ether stretching
	950	ν (CH_2) out-of-plane bending
	886	ν(CC) stretching
	838	ν(CC) stretching
PEG coated calcium ferrite nanoparticles	3400	ν(OH) stretching
	2870	ν_s(CH_2) stretching
	1795	ν(C=O) stretching
	1631	ν(OH) bending
	1437	δ_s(CH_2) scissoring
	1250	ν(OH) bending and τ(CH_2) twisting
	1103	ν(C-O-C) ether stretching
	950	ν (CH_2) out-of-plane bending
	875	ν(O-Fe-O) stretching
	712	ν(Fe-OH) stretching
	551	ν(Fe-O) stretching
	467	ν(Fe-O) stretching

3.3.2.4 Morphological analysis

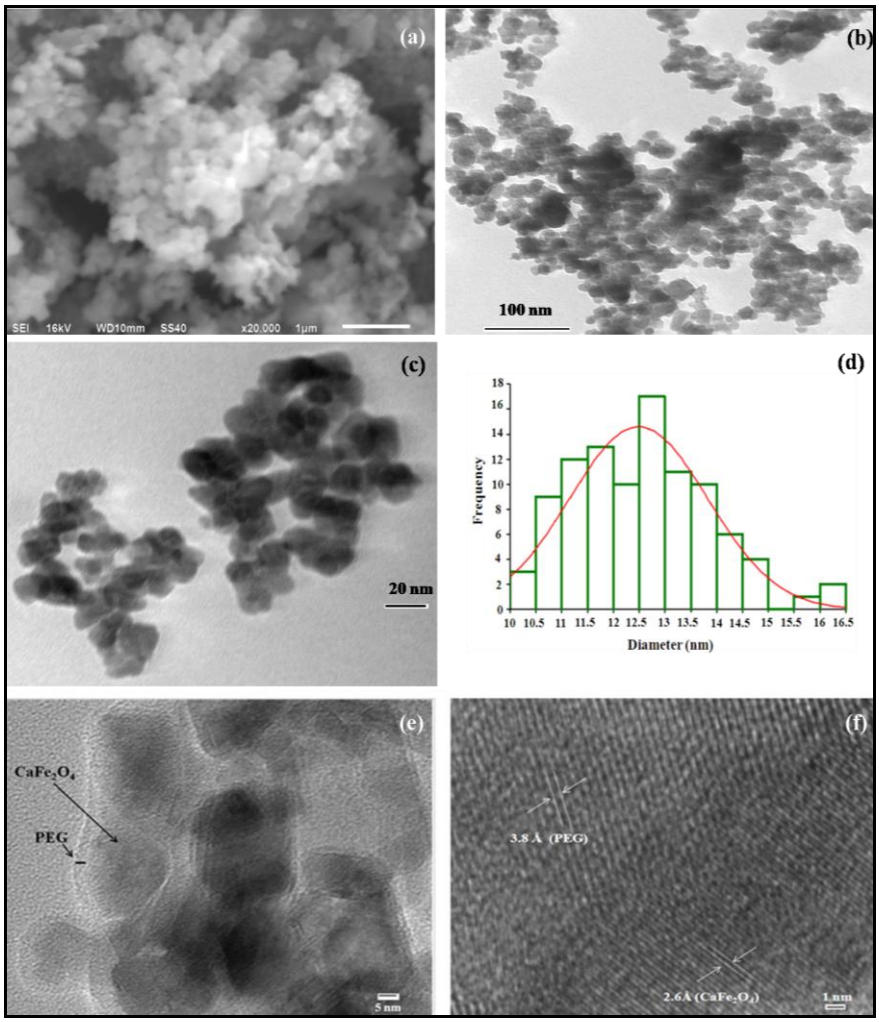

Figure 3.17 (a) SEM (b, c) TEM micrographs (d) histogram and (e, f) HRTEM images of PEG coated calcium ferrite nanoparticles

Fig. 3.17(a) and figs. 3.17(b-d) show the spherical formation of PEG coated calcium ferrite nanoparticles with a narrow size distribution of about 10.0-16.5 nm, as depicted by the histogram. The reduction in the agglomeration as compared to the bare nanoparticles (fig. 3.10(c)) can be well observed pertaining to the PEG coating on calcium ferrite nanoparticles. The HRTEM image in fig. 3.17(e) further confirms the PEG coating on calcium ferrite nanoparticles

and shows that there are multiple numbers of nanoparticles present as the core inside PEG coating. Several nanoparticles remain attached together as aggregates by mutual magnetic attractions to form the core [30]. In fig. 3.17(f), the lattice fringes corresponding to PEG and calcium ferrite nanoparticles can be well observed.

3.3.2.5 Magnetic analysis

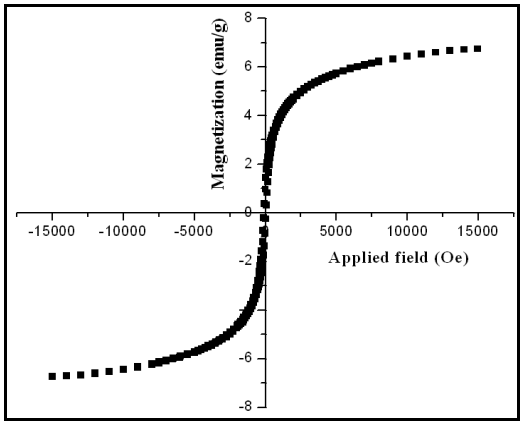

Figure 3.18 M-H curve of PEG coated calcium ferrite nanoparticles

The magnetic response of PEG coated calcium ferrite nanoparticles, as studied by VSM, in fig. 3.18, suggests its superparamagnetic behaviour. However, a drop in the magnetic saturation (M_s) value has been observed from 36.76emu/g for calcium ferrite nanoparticles to 6.74emu/g for PEG coated calcium ferrite nanoparticles. The remanent magnetization (M_R) and squareness value (M_R/M_S ratio), as obtained, are 0.89emu/g and 0.119, respectively. Superparamagnetic behavior is defined by less squareness value [17]. For non-interacting superparamagnetic particles, it is 0.5 [58], in case of interacting superparamagnetic particles the dipolar interactions reduce both the magnetic squareness (M_R/M_S ratio) and coercivity (H_C) values due to demagnetizing effect [58, 59]. Magnetic squareness value related to superparamagnetic behaviour is 0.1, i.e. it loses greater than 90% of its magnetism on removal of

the applied magnetic field [60]. The squareness value of PEG coated calcium ferrite nanoparticles is 0.119. Therefore, it exhibits the characteristic feature of superparamagnetism. The reduction in the magnetic saturation value is attributed to the chemical combination of non-magnetic layer of PEG and calcium ferrite nanoparticles. It is well known that the form of magnetization curve is sensitive to particle size and the size distribution, which in this case relates to the magnetic particle content. Thus, if there is a non-magnetic surface coating on the particle, the magnetic size measured will be smaller than the physical size [143]. The reaction results in the formation of magnetically dead layer which makes the magnetic diameter of the particles smaller than the physical size [144]. Hence, the magnetic saturation value decreases.

As observed in the TEM micrograph (figs. 3.17(b, c), the size of PEG coated calcium ferrite nanoparticles increases as compared to bare nanoparticles, this results in higher magneto-crystalline anisotropy for the nanocomposite. The magneto-crystalline anisotropy originates from the coupling between electron spins and the angular momentum of the electron orbital (L-S coupling). Therefore, the superparamagnetic behaviour of a particle, which is directly related to its magneto-crystalline anisotropy, can be correlated to its L-S coupling, as well [56, 57].The coating of PEG on calcium ferrite nanoparticles increased the overall size and this further increased its magneto-crystalline anisotropy, as it is directly proportional to the volume of particles ($EA = KV \sin^2\theta$), where, K is the magneto-crystalline anisotropy constant (related to the strength of the L-S coupling), V is the volume of the nanoparticle and θ is the angle between the magnetization direction and the easy axis of the nanoparticle. EA serves as an energy barrier for blocking the flips of magnetic moments [56, 57]. The total effective magnetic moment of PEG coated nanoparticles is found to decrease, which is most probably due to a non-collinear spin structure originating from the pinning of the surface spins and PEG coating at the interface of

nanoparticles [145]. The measured magnetic moment in PEG coated calcium ferrite nanoparticles decreases due to the contribution of the higher volume of the non-magnetic coating mass (PEG) to the total sample volume, which quenches the surface moment [28] and results in decrease in the magnetization value. However, coating of the nanoparticles with PEG did not affect the super paramagnetic nature of the synthesized calcium ferrite nanoparticles, as evidenced in fig. 3.18.

3.3.2.6 Cytotoxicity analysis

The experimental procedure is same as discussed in section 3.2.6.1. Following are the results obtained.

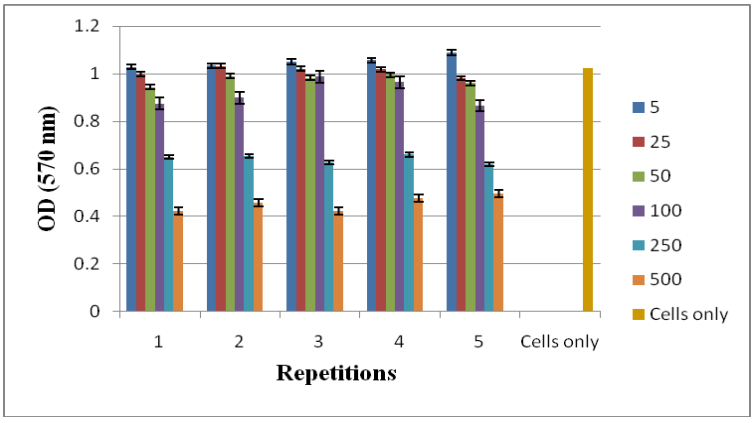

Figure 3.19 Optical Density (OD) at 570 nm of all repetitions at all concentrations

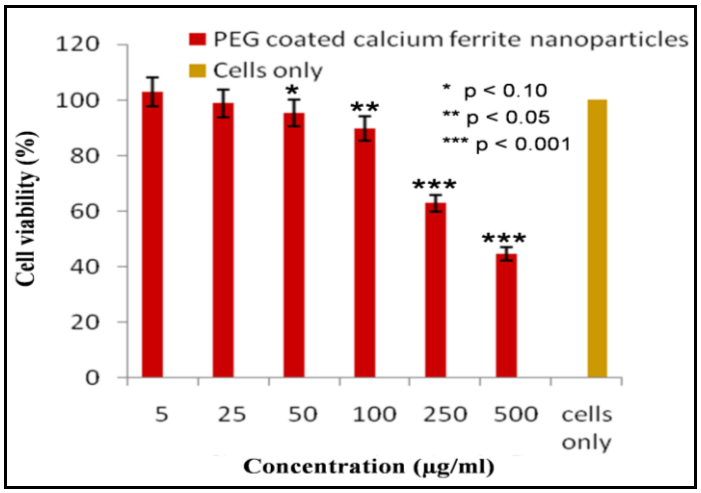

Figure 3.20 Mean cell viability (%) as determined by MTT assay, with values presented as *p<0.10, **p<0.05, ***p<0.001 compared with untreated cells (dependent student's t-test)

Fig. 3.19 exhibits the dose dependent reduction in cell viability of the PEG coated calcium ferrite nanoparticles. The cell viabilities at 5, 25, 50, 100, 250, 500 µg/ml, calculated according to Eq. 3.2 are 102.9%, 98.8%, 95.3%, 89.9%, 62.8%, 44.6%, respectively. The statistical analysis using student's dependent t-test has also been calculated, fig. 3.20, to determine the effect of synthesized nanocomposite on the cells [134]. For concentration below 250µg/ml, the cell viability is greater than 90%, suggesting that the nanoparticles are non-toxic to the cells, but at a higher concentration, a significant toxicity causing cell death has been observed. As compared to bare calcium ferrite nanoparticles, the PEG coated nanocomposite exhibits higher cell viability at all the concentrations. This is attributed to the reduced agglomeration and well-dispersion of the nanocomposite due to surface coating of PEG. The well-dispersion of nanocomposite results in their relatively less aggregation, thus facilitating their intracellular uptake and hampering the cellular damage [48]. The high surface energy and

magnetic interaction of bare nanoparticles result in their cellular uptake as enlarged agglomerates, leading to possible immune responses [48].

3.4 Silica coated calcium ferrite nanoparticles

3.4.1 Experimental procedure

Silica coating on calcium ferrite nanoparticles was done by modified stober process [50]. Briefly, 150 ml ethanol, 3 ml water, 5.1 ml ammonium hydroxide and 900µl TEOS were added in a beaker and kept at 40˚C, while stirring. After 20 min, 6 ml aqueous solution of calcium ferrite nanoparticles with the concentration of 4mg/ml was added and the reaction was allowed to proceed for 5 hour. The nanoparticles were magnetically separated by placing the solution on a magnetic slab of surface field 2T. The magnetic nanoparticles settled at the bottom and the solution was carefully removed. The obtained product was washed several times with ethanol and dried overnight in a vacuum oven at 60°C. Finally, silica coated calcium ferrite nanoparticles were obtained.

3.4.2 Results and discussion

3.4.2.1 Structural analysis

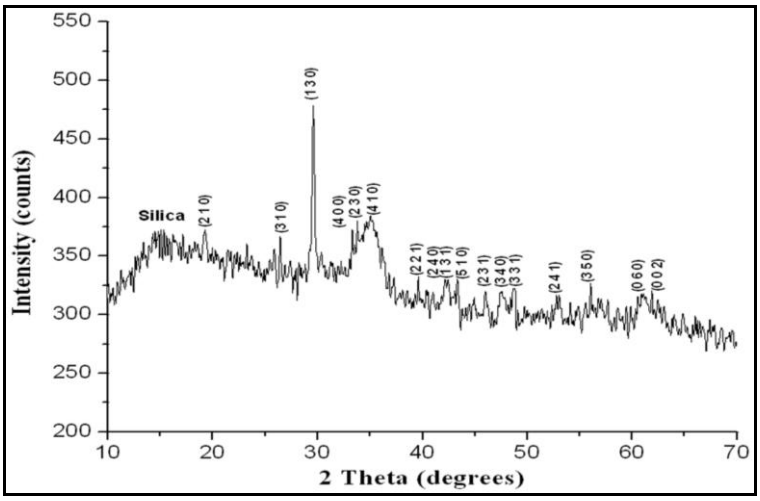

Figure 3.21 XRD pattern of silica coated calcium ferrite nanoparticles

Fig. 3.21 shows the XRD pattern, where all the peaks are indexed and well-matched to the orthorhombic structure (JCPDS Card No. 74-2136) of $CaFe_2O_4$. Less intensity of $CaFe_2O_4$ core is attributed to the silica coating which diminishes the peak intensities [146]. Also, the broad band near $2\theta \sim 15\text{-}20°$ corresponds to the amorphous silica surrounding calcium ferrite nanoparticles. Table 3.6 shows the theoretical and calculated values of the unit cell parameters.

Table 3.6 Theoretical and calculated values of the unit cell parameters of silica coated calcium ferrite nanoparticles

Silica coated $CaFe_2O_4$				
		Theoretical	Calculated	Difference
Unit cell parameters	a	10.66	10.82	0.166
	b	9.200	9.400	0.200
	c	3.010	2.843	0.166

3.4.2.2 Thermal analysis

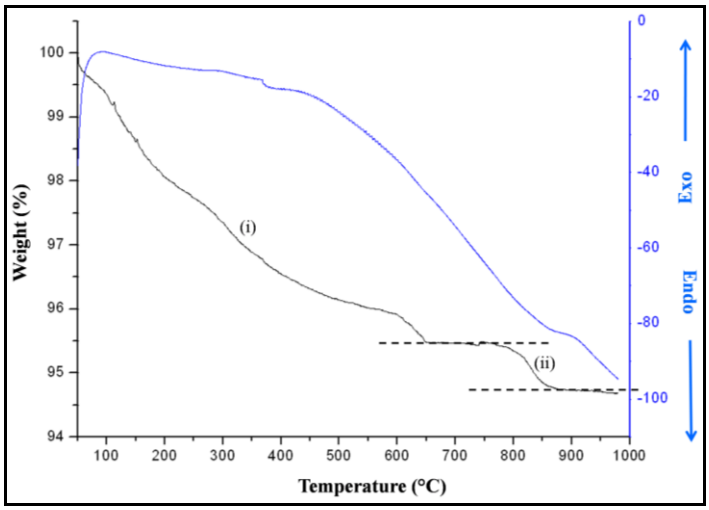

Figure 3.22 TGA and DTA patterns of silica coated calcium ferrite nanoparticles

The decomposition of the synthesized nanocomposite, fig. 3.22, comprises of two weight loss regions (i) ~50-650 ˚C (ii) ~650-850 ˚C. The broad weight loss in the first region can be attributed to loss of physically adsorbed water on the surface of the nanocomposite and possibly due to condensation of silanol [50, 147], where a broad exothermic peak corresponding to this region can be well observed. The loss at higher temperature can be attributed to the loss of structural water (dehydroxylation) [148, 149]. No weight loss is observed above that revealing the stability of the nanocomposite.

3.4.2.3 FTIR analysis

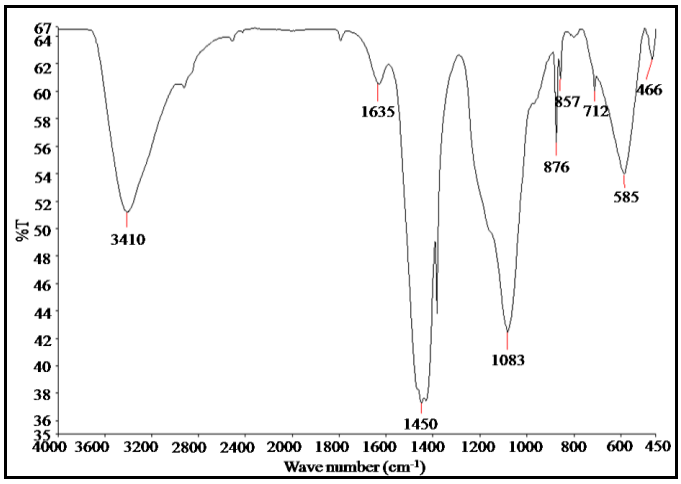

Figure 3.23 FTIR spectrum of silica coated calcium ferrite nanoparticles

FTIR spectrum of silica coated calcium ferrite nanoparticles in fig. 3.23, exhibits a broad stretch at 3410 cm^{-1} and 1635 cm^{-1} due to O-H stretching and O-H scissor bending vibrations, respectively [116, 138]. The band at 1450 cm^{-1} corresponds to Si-CH_2 scissoring vibrations [150]. The characteristic sharp absorption band at 1083 cm^{-1} is assigned to the asymmetric stretching vibration of Si-O-Si [51]. The bands at 876 cm^{-1} and 875 cm^{-1} correspond to bending vibrations of Fe-OH [151]. The bending vibrations of O–Si–O group appears at 466cm^{-1} confirming the presence of silica in the nanocomposite [50]. The band of silanol group (Si-OH) exists at the surface of the synthesized nanocomposite. The bands at 712 cm^{-1} and 585 cm^{-1} correspond to Fe-O bond due to the ferrite skeleton [61]. Description of the FTIR spectrum of silica coated calcium ferrite nanoparticles has been tabulated in table 3.7.

Table 3.7 Description of FTIR spectrum of silica coated calcium ferrite nanoparticles

Silica coated calcium ferrite nanoparticles	IR band (cm^{-1})	Description
	3410	ν(O-H) stretching
	1635	ν(O-H) scissor bending
	1450	ν (Si-CH_2) scissoring
	1083	ν_{as}(Si-O-Si) stretching
	876, 857	ν (Fe–O–H) bending
	712, 585,	ν(Fe-O) stretching
	466	ν(O-Si-O) bending

3.4.2.4 Morphological analysis

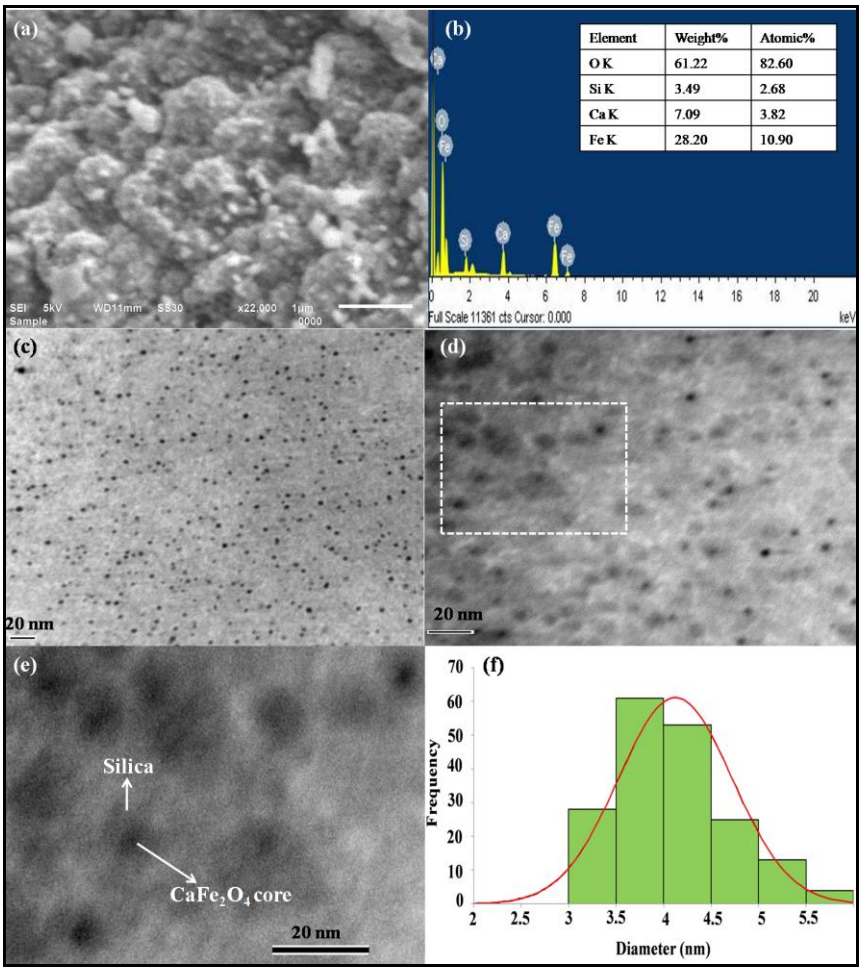

Figure 3.24 (a) SEM micrograph (b) EDAX spectrum (c, d) TEM micrographs at different magnifications (e) enlarged view of the dotted box (f) histogram of silica coated calcium ferrite nanoparticles

Fig. 3.24(a, b) shows the SEM micrograph and EDAX spectrum of the nanocomposite, confirming the presence of Ca, Fe, O and Si elements along with their observed atomic% and weight % values. TEM micrographs in figs. 3.24(c-e) reveal the spherical morphology of the synthesized nanocomposite. Fig. 3.24(e) represents the enlarged view of the dotted box in fig. 3.24(d); where the core-shell formation and the contrast of dark $CaFe_2O_4$ core and amorphous silica surrounding it, are well-observed. Formation of agglomeration-free nanocomposite is credited to the presence of silica shell. It stabilizes the high surface energy and also forms a magnetically dead layer that inhibits the magnetic and inter-particle interactions of the nanocrystallites, thus preventing their agglomeration. Fig. 3.24(f) shows the histogram, plotted by analyse-it software. It reveals that the particle size lies in the range of 3-6 nm with the highest frequency (diameter) falls in the size range of 3.5-4.0 nm.

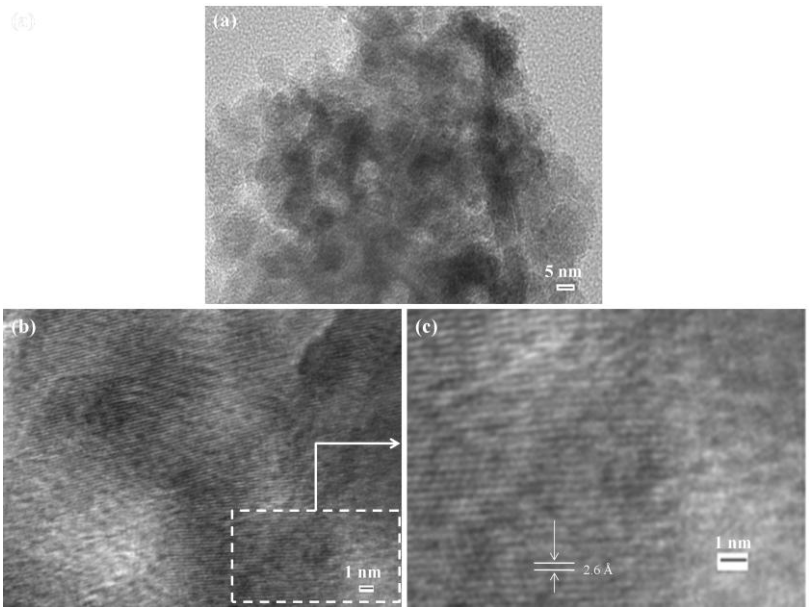

Figure 3.25 (a, b) HRTEM image of silica coated calcium ferrite nanoparticles at different scales (e) enlarged view of the dotted box

Fig. 3.25(a, b) represents the HRTEM image of the nanocomposite at different scales, signifying the amorphous nature of silica. It shows that there are multiple numbers of

nanoparticles present as the core inside silica coating. Fig. 3.25(c) shows the lattice fringes corresponding calcium ferrite nanoparticles.

3.4.2.5 Magnetic analysis

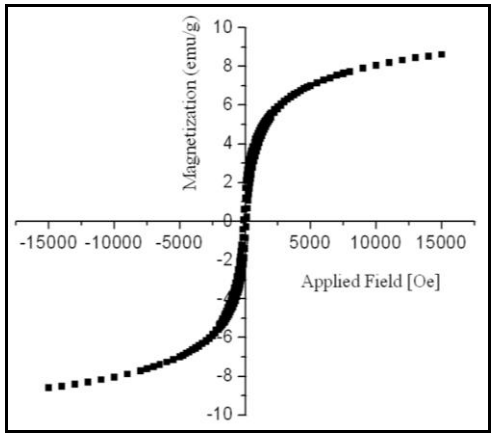

Figure 3.26 M-H curve of silica coated calcium ferrite nanoparticles

In the M-H curve, fig. 3.26, the nanocomposite exhibits superparamagnetic behaviour, with magnetic saturation (Ms), remanent magnetization (M_R) and squareness value (M_R/M_S ratio), 8.55emu/g, 1.05emu/g and 0.122, respectively. Squareness value is instrumental in determining superparamagnetic behaviour [17]. For non-interacting superparamagnetic particles, the squareness value is 0.5; in case of interacting superparamagnetic particles demagnetizing effects due to dipolar interactions reduce both the magnetic squareness (M_R/M_S ratio) and coercivity (H_C) values [17, 58, 59]. Magnetic squareness value ascribable to the above is 0.1; i.e. more than 90% of magnetism is lost on removal of the magnetic field [60]. As the obtained squareness value is 0.122, therefore, it can be comprehended that the nanocomposite exhibits superparamagnetism. Superparamagnetic behaviour of a particle is directly related to its magneto-crystalline anisotropy and is further correlated to L-S coupling, as the magneto-crystalline anisotropy originates from the coupling between electron spins and the angular

momentum of the electron orbital (L-S coupling) [56]. As the particle size decreases, a large percentage of the atoms become surface atoms, resulting in pronounced surface and interface effects leading to increase in the ratio of dead layer (non-magnetic silica) to magnetic core [144], thus diluting the magnetization value, as compared to the bare nanoparticles.

3.4.2.6 Cytotoxicity analysis

The experimental procedure is same as discussed in section 3.2.6.1. Following are the results obtained.

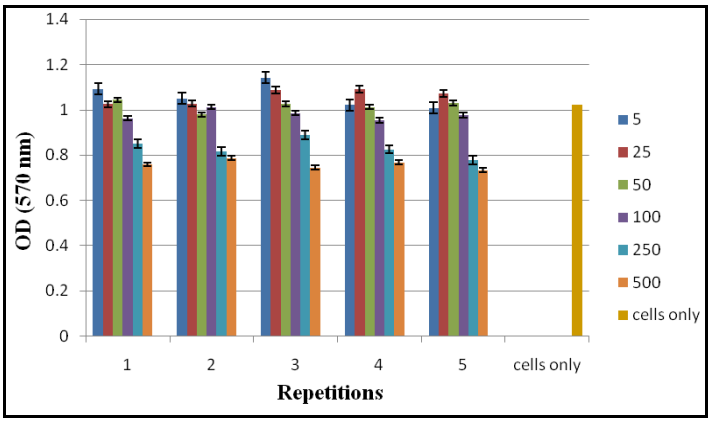

Figure 3.27 Optical Density (OD) at 570 nm of all repetitions at all concentrations

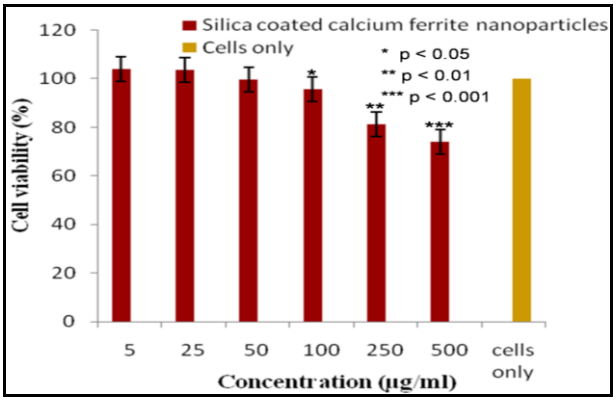

Figure 3.28 Mean cell viability (%) as determined by MTT assay, with values presented as *p<0.05, **p<0.01, ***p<0.001 compared with untreated cells (dependent student's t-test)

Dose-dependent cytotoxicity of the nanocomposite tested on T-cell lines (Jurkat cells) using MTT assay reveals their non-toxic behaviour. The cell viabilities at 5, 25, 50, 100, 250, 500 µg/ml, calculated according to Eq. 3.2 are 103.9%, 103.7%, 99.6%, 95.6%, 81.3%, 74.2%, respectively. Fig. 3.27 shows the optical density (OD) values of all repetitions at all concentrations. In fig. 3.28, the statistical analysis using paired t-test [134] has also been determined to comprehend the effect of synthesized nanocomposite on the cells. The enhanced cell viability is attributed to good dispersibilty of silica coated calcium ferrite nanoparticles in the medium. This results in their relatively less aggregation, thus encouraging their intracellular uptake and reducing cellular damage [48]. Silica protects MNPs from acidic erosion. Correspondingly, the particle stability converts into reduced cytotoxicity [45]. A significant cell viability has been observed below 500 µg/ml, and a fall occurs at 500µg/ml; this may be attributed to shortage of culture media required for the growth of the cells while running the assay, rather than any toxicity of the synthesized nanocomposite. On exposure, the nanocomposite first adhere to cells, then are internalized by endocytosis, finally get accummulated in digestive vacuoles [70]. Therefore, at higher concentration, the overloading of particles results in fatality of cells.

Chapter – 4

POTASSIUM FERRITE NANOCOMPOSITES

Chapter 4

The present chapter includes the experimental procedures for synthesizing potassium ferrite nanoparticles and their surface coating with PEG and silica. Their structural, morphological, thermal and magnetic properties along with cytotoxicity have been explained.

Following are the publications corresponding to potassium ferrite nanoparticles and nanocomposites. Some of the results have been discussed in the present chapter.

1. Lavanya Khanna, N. K. Verma, Silica/potassium ferrite nanocomposite: Structural, morphological, magnetic, thermal and in vitro cytotoxicity analysis, Materials Science and Engineering B, 178 (2013) 1230-1239.

2. Lavanya Khanna, N. K. Verma, Synthesis, characterization and biocompatibility of potassium ferrite nanoparticles, Journal of Materials Science and Technology 30(1) (2014) 30-36.

3. Lavanya Khanna, N. K. Verma, Study on novel, superparamagnetic and biocompatible PEG/$KFeO_2$ nanocomposite, Journal of Applied Biomedicine (10.1016/j.jab.2014.05.003).

4.1 Experimental procedure

4.1.1 Synthesis of potassium ferrite nanoparticles

The synthesis of potassium ferrite nanoparticles was done by sol-gel method as explained in section 3.1.1. Briefly, 1M solution of potassium nitrate and 2M solution of ferric nitrate were mixed. To this mixture, 2M citric acid solution was added along with 7ml of ethylene glycol. The solution was constantly magnetically stirred and was heated at 80-90ºC. The viscous gel began frothing after the removal of water molecules from the mixture. During heating, the solution became viscous and gradually formed a very viscous brown gel. On further heating dried gel was formed and it continued to burn in a self propagating combustion manner until all the gel was completely converted to a brown-coloured powder, which also indicated the completion of auto-ignition process. Until the whole citrate complex was consumed, the decomposition process would not stop. The formation of sol, gel, dried gel and finally powder, on heating and stirring was obtained. The obtained powder was thoroughly washed with ethanol by centrifugation at 2000 rpm; it was dried overnight in vacuum oven at 60ºC. The dried powder was grinded in pestle and mortar to obtain uniform and fine powder. The powder was further calcined at 500° C for 2 h. to obtain the final product. The chemical reaction of the synthesis process is as follows:

$$9KNO_3 + 9Fe(NO_3)_3.9H_2O + 10C_6H_8O_7.H_2O \rightarrow 9KFeO_2 + 131H_2O + 60CO_2(g) + 18N_2(g)$$

4.1.2 Results and discussion

4.1.2.1 Structural analysis

The X-ray diffractogram depicts the crystallinity of the synthesized nanoparticles. Fig. 4.1 shows the XRD diffractogram of potassium ferrite nanoparticles, where all the peaks are indexed and well-matched to the orthorhombic structure (File No. 83-2152, space group: Pbca) of $KFeO_2$. The lattice parameter values, as calculated have been tabulated in table 4.1.

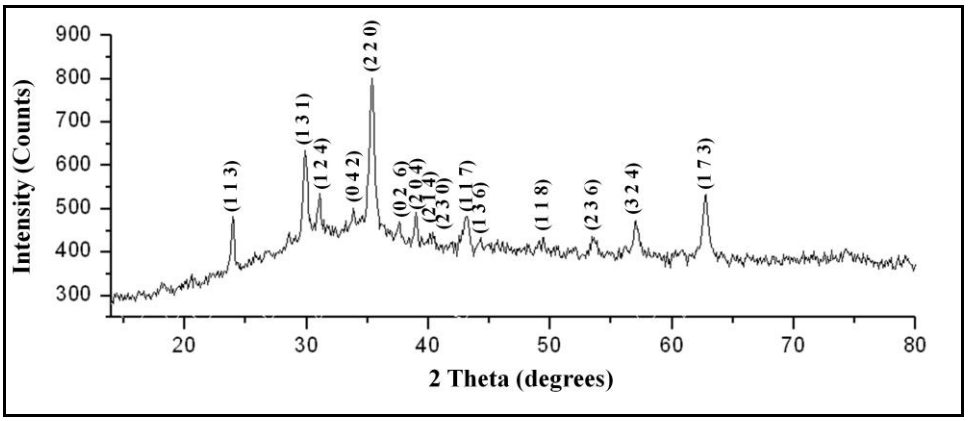

Figure 4.1 XRD pattern of potassium ferrite nanoparticles

Table 4.1 Theoretical and calculated values of the unit cell parameters for potassium ferrite nanoparticles

$KFeO_2$				
		Theoretical	Calculated	Difference
Unit cell parameters	a	5.577	5.577	0.000
	b	11.22	12.30	1.080
	c	15.89	16.20	0.310

4.1.2.2 Thermal analysis

The thermal decomposition of potassium ferrite compounds is strongly sensitive to water content. In fig. 4.2, the TG curve exhibits two weight loss regions, the first region of the weight loss (i) from room temperature to around 160°C, can be attributed to the loss of physically adsorbed water and gases on the surface of potassium ferrite nanoparticles [25], where the corresponding small endothermic peak can be well observed. Except that, there are no exothermic or endothermic peaks in the DTA curve.

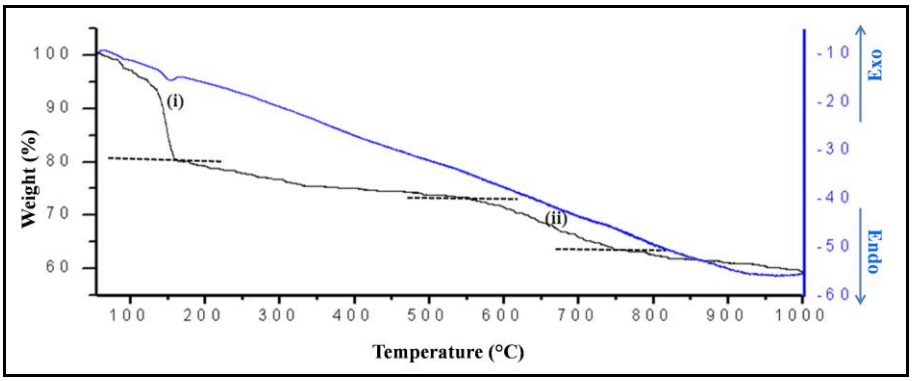

Figure 4.2 TGA and DTA patterns of potassium ferrite nanoparticles

There is a little weight loss in the TGA curve in the temperature range 160-550 °C. The second weight loss region (ii), at higher temperature (550-750°C) in TG curve can be attributed to the removal of structural water (dehydroxylation) from the surface of nanoparticles [148, 149]. This loss is marked with a weak and broad exothermic effect. Above 750°C there is no weight loss, depicting the thermal stability of potassium ferrite nanoparticles.

4.1.2.3 FTIR analysis

The FTIR spectrum of potassium ferrite nanoparticles, fig. 4.3, exhibits a broad stretch at 3398cm^{-1} and 1626cm^{-1} due to O-H stretching and bending vibrations, respectively, pertaining to adsorption of atmospheric water on the surface of the synthesized nanoparticles [116, 138]. The band at 1019 cm^{-1} corresponds to metal-alloy (Fe-K) vibration and bands at 694, 635, 584, 557, 480, 442 cm^{-1} are attributed to Fe-O bonds due to the presence of ferrite skeleton [61]. Table 4.2 gives the description of all the observed bands.

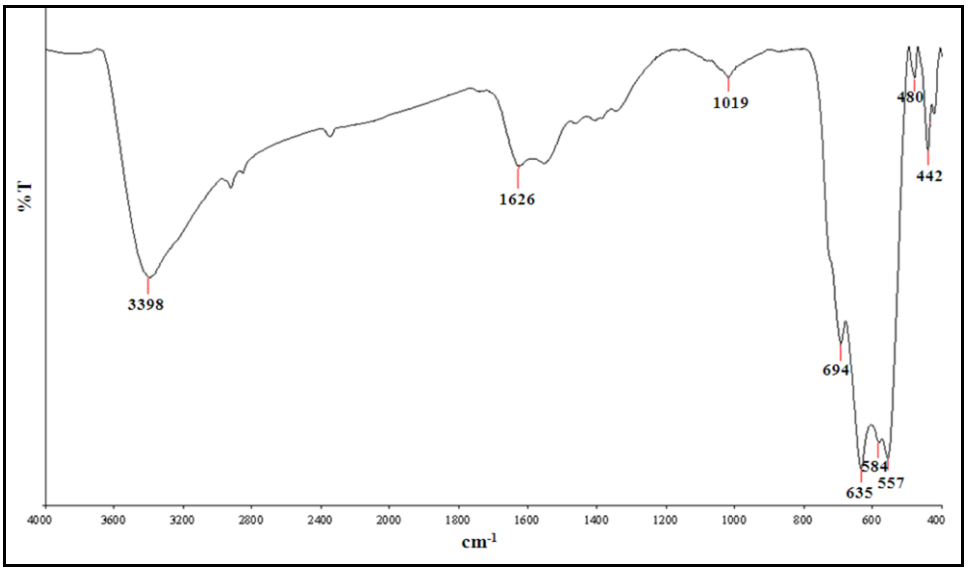

Figure 4.3 FTIR spectrum of potassium ferrite nanoparticles

Table 4.2 Description of FTIR spectrum of potassium ferrite nanoparticles

Potassium ferrite nanoparticles	IR band (cm^{-1})	Description
	3398	*v*(OH) stretching
	1626	*v*(OH) bending
	1019	*v*(Fe-K) stretching
	694, 653, 584, 557, 480, 442	*v*(Fe-O) stretching

In figs 4.2 and 4.3, no detection corresponding to traces of any organic impurity or unreacted precursors have been observed. This ensures the completion of the reaction process and ascertains that the obtained toxicity is solely due to synthesized nanoparticles. Toxicity is very sensitive to impurity and therefore it becomes imperative to ensure that the sample is free from any impurity.

4.1.2.4 Morphological analysis

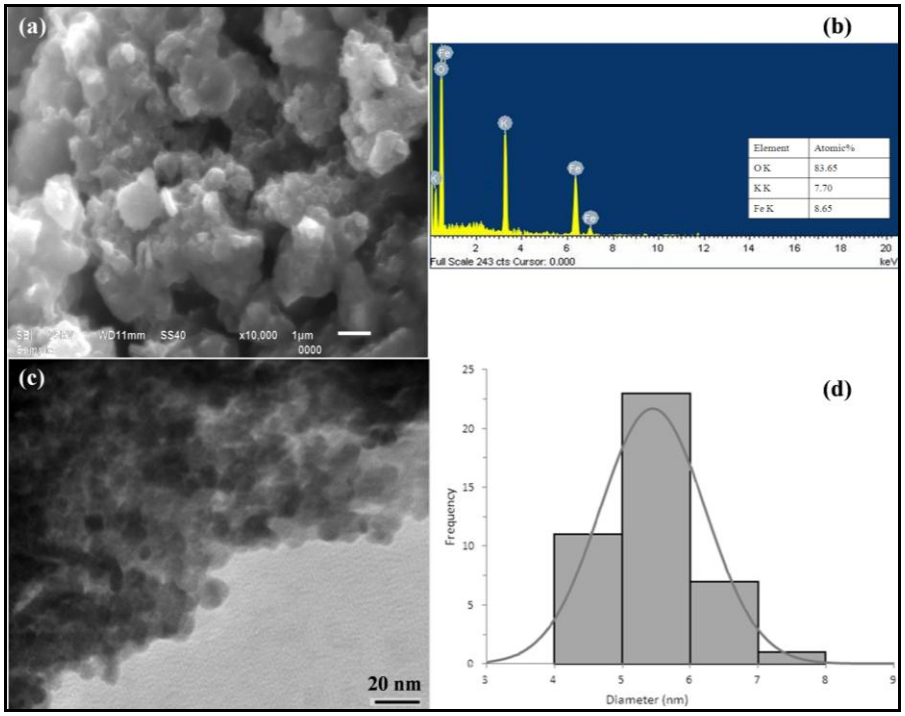

Figure 4.4 (a, b) SEM micrograph with EDAX spectrum (c, d) TEM micrograph along with histogram of potassium ferrite nanoparticles

Figs. 4.4(a, b) show the SEM micrograph and EDAX pattern of potassium ferrite nanoparticles, along with the table depicting the atomic% values of the elements observed i.e. K, Fe and O. Their agglomerated form in SEM (fig. 4.4(a)) as well as TEM (fig. 4.4(c)) micrographs is attributed to high surface energy and magnetic interactions. TEM micrograph

also reveals their spherical formation with a narrow size distribution of about 4-8 nm, as depicted by the histogram in fig. 4.4(d).

4.1.2.5 Magnetic analysis

The magnetic response of potassium ferrite nanoparticles was studied by VSM, as shown in fig. 4.5.

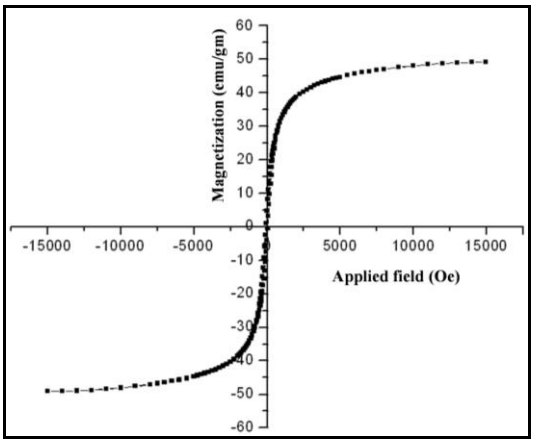

Figure 4.5 M-H curve of potassium ferrite nanoparticles

In the M-H curve, potassium ferrite nanoparticles exhibit superparamagnetic behaviour with magnetic saturation (M_S) value, remanent magnetization (M_R) and squareness value (M_R/M_S ratio) of 49.01emu/g, 4.34emu/g and 0.08, respectively. The squareness value obtained from the M-H curve determines the magnetic behaviour; high value denotes ferromagnetism and small value denotes superparamagnetism [17, 152]. Small squareness value obtained from the M-H curve reflects the superparamagnetic behavior of the synthesized nanoparticles. For non-interacting superparamagnetic particles, the squareness value is 0.5, while in the case of interacting superparamagnetic particles, demagnetizing effects prevail due to the reduction in dipolar interactions, which further reduce both the magnetic squareness (M_R/M_S ratio) and

coercivity (H_C) values [58, 59]. Magnetic squareness value ascribable to superparamagnetic behaviour is 0.1, i.e. it loses greater than 90% of its magnetism on removal of the applied magnetic field [60]. The squareness value, as obtained is 0.08. Therefore, it can be comprehended that potassium ferrite nanoparticles exhibits the characteristic feature of superparamagnetism.

4.1.2.6 Cytotoxicity analysis

The experimental procedure is same as discussed in section 3.2.6.1 with 4 replicates. Following are the results obtained.

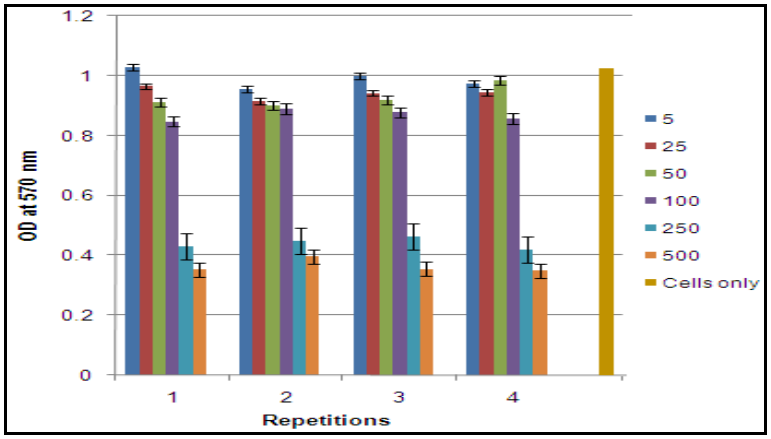

Figure 4.6 Optical Density (OD) at 570 nm of all repetitions at all concentrations

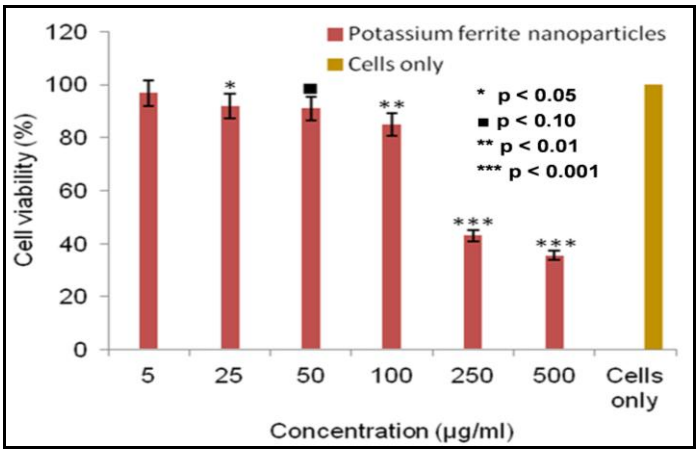

Figure 4.7 Mean cell viability (%) as determined by MTT assay, with values presented as *p < 0.05, ■ p < 0.10, **p < 0.01, ***p < 0.001 compared with untreated cells (dependent student's t-test)

Fig. 4.6 exhibits the dose dependent reduction in the cell viability for potassium ferrite nanoparticles at all concentrations for all repetitions. The cell viabilities at 5, 25, 50, 100, 250, 500µg/ml, calculated according to Eq. 3.2 are 96.7%, 92%, 90.9%, 84.8%, 43.1%, 35.5%. Each data point in fig. 4.7 was obtained by averaging that of four wells. The untreated cells were used as control *(marked as 'cells only'),* depicting a good cell viability at concentration below 250µg/ml, but at higher concentrations, a significant loss of viability is observed, indicating that higher concentration of potassium ferrite nanoparticles show more cytotoxicity. The interaction of nanoparticles with cells begins with their adherence to the surface of the cell, which is followed by internalization by endocytosis, further leading to accumulation in digestive vacuoles [70]. The nanoparticle-protein interaction is a key issue for defining and understanding the toxicity of the MNPs ; the unfavourable changes in the protein configuration, the denaturation of the proteins on interaction could cause the exposure of new antigenic sites which may commence a new immune response [135]. The statistical analysis using paired t- test

[134] has also been calculated. MTT-assay results indicate that $KFeO_2$ nanoparticles supported continuous growth of the cells on their surface. Even though at 250 and 500µg/ml, the viability drops down to significant values, it might have been caused due to shortage of culture media required for the growth of the cells, rather than any toxicity of the synthesized nanoparticles. At higher concentrations, the overloading of particles occurs and this consequently results in fatality of cells.

4.2 PEG coated potassium ferrite nanoparticles

4.2.1 Experimental procedure

To synthesize PEG coated potassium ferrite nanoparticles, the calcined nanoparticles were mixed with the PEG-1500 solution with the concentration of 0.01g/ml, followed by addition of a certain amount of ammonia solution until the pH of the solution reached 11. After continuous stirring, a homogeneous mixture was obtained. The mixture was poured into a Teflon lined stainless-steel autoclave (50ml), kept at 140°C for 12 hour and then cooled to room temperature naturally [136]. The obtained product was washed several times with ethanol; finally it was dried overnight in a vacuum oven at 60°C. The dried powder was grinded in pestle and mortar to obtain uniform fine powder.

4.2.2 Results and discussion

4.2.2.1 Structural analysis

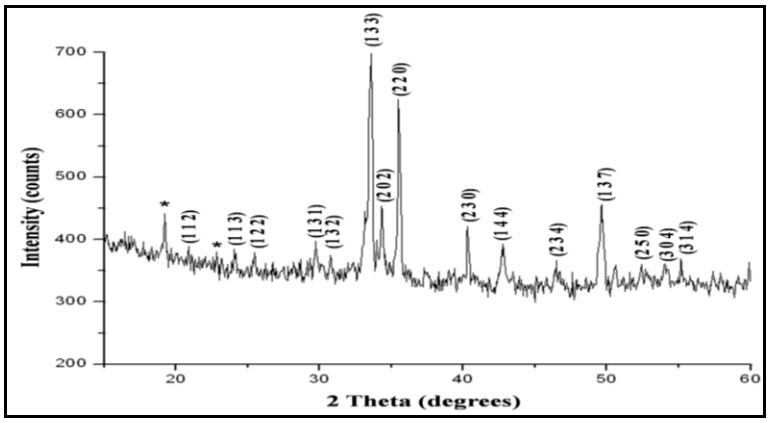

Figure 4.8 XRD pattern of PEG coated potassium ferrite nanoparticles

Fig. 4.8 shows the XRD pattern of PEG coated potassium ferrite nanoparticles, two peaks at ~19° and 23°, characteristic of PEG have been observed (marked as *), confirming the presence of PEG. All the other peaks are attributed to the formation of orthorhombic structure (File No. 83-2152, space group: Pbca) of $KFeO_2$. The sharpening of the peaks is due to the increase in the size after PEG coating, this is also confirmed by the TEM analysis. Table 4.3 gives the theoretical and calculated values of the unit cell parameters.

Table 4.3 Theoretical and calculated values of the unit cell parameters of PEG coated potassium ferrite nanoparticles

PEG coated $KFeO_2$				
		Theoretical	Calculated	Difference
Unit cell parameters	a	5.577	5.706	0.129
	b	11.22	10.94	0.279
	c	15.89	15.91	0.024

4.2.2.2 Thermal analysis

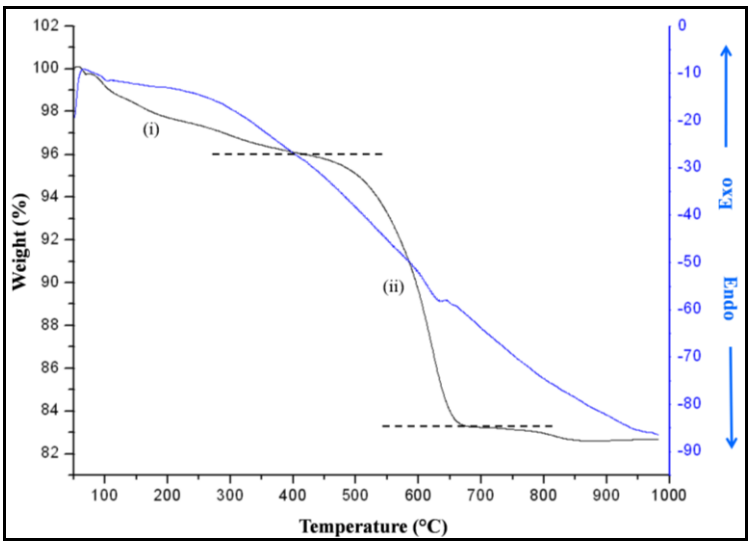

Figure 4.9 TGA and DTA curves of PEG coated potassium ferrite nanoparticles

The decomposition of PEG coated potassium ferrite nanoparticles, fig. 4.9, comprises of two distinct weight losses regions i) ~50-400 °C, ii) ~400-660 °C, denoted by black dashed lines. The first loss (~4%) corresponds to the release of the adsorbed water on the surface of the nanocomposite. The second weight loss (~14%) corresponds to the decomposition of PEG molecules, possibly loss of organic hydrogen [138]. No significant peak has been observed in the DTA curve. Temperature at which the weight of the PEG polymer significantly decreases is shifted to high temperature indicating the enhanced thermal stability of PEG due to the formation of covalent bonds with potassium ferrite nanoparticles.

4.2.2.3 FTIR analysis

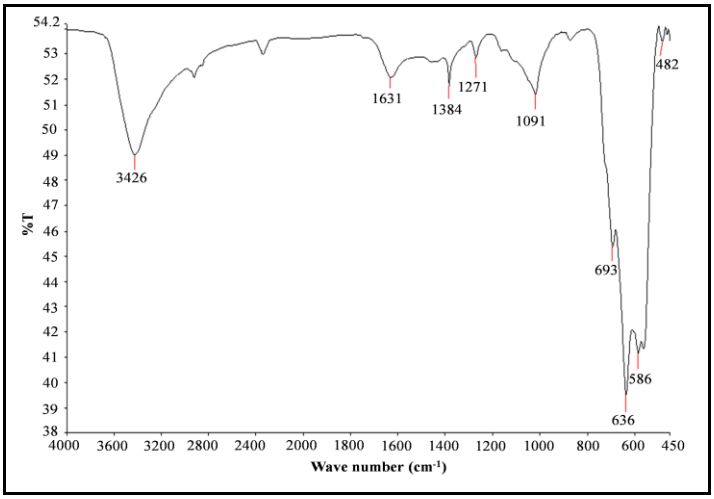

Figure 4.10 FTIR spectrum of PEG coated potassium ferrite nanoparticles

In the FTIR spectrum of PEG coated potassium ferrite nanoparticles, fig. 4.10, the broad stretch at 3426 cm^{-1} and 1631 cm^{-1} is due to O-H stretching and O-H bending vibrations, respectively [116,138]. The band relative to molecular water in PEG is usually centered at 1644 cm^{-1}, but in the synthesized nanocomposite it is formed at a slighter lower wave number, indicating that surface coating of PEG has led to partial loss of water molecules [138]. The vibrations of C-H (wagging) at 1384 cm^{-1} [30, 138], the bending vibrations of O-H and C-H (twisting) stretch at 1271 cm^{-1} [116] and a sharp C-O-C ether stretch at 1091 cm^{-1} [32, 38] clearly confirms the presence of PEG on potassium ferrite nanoparticles. The bands due to C-H vibrational modes and bands due to water are strongly reudced in intensity due to dehydroxilation and oxidation of the organic moieties [138]. The observed bands at 693, 636, 586, 482 cm^{-1} correspond to Fe-O stretching bond [61]. Table 4.4 shows the description of the bands for PEG coated potassium ferrite nanoparticles.

Table 4.4 Description of FTIR spectrum of PEG coated potassium ferrite nanoparticles

Potassium ferrite nanoparticles	IR band (cm^{-1})	Description
	3426	ν(OH) stretching
	1631	ν(OH) bending
	1384	$w(CH_2)$ wagging
	1271	ν(OH) bending and $\tau(CH_2)$ twisting
	1091	ν(C-O-C) ether stretching
	693, 636, 586, 482	ν(Fe-O) stretching

4.2.2.4 Morphological analysis

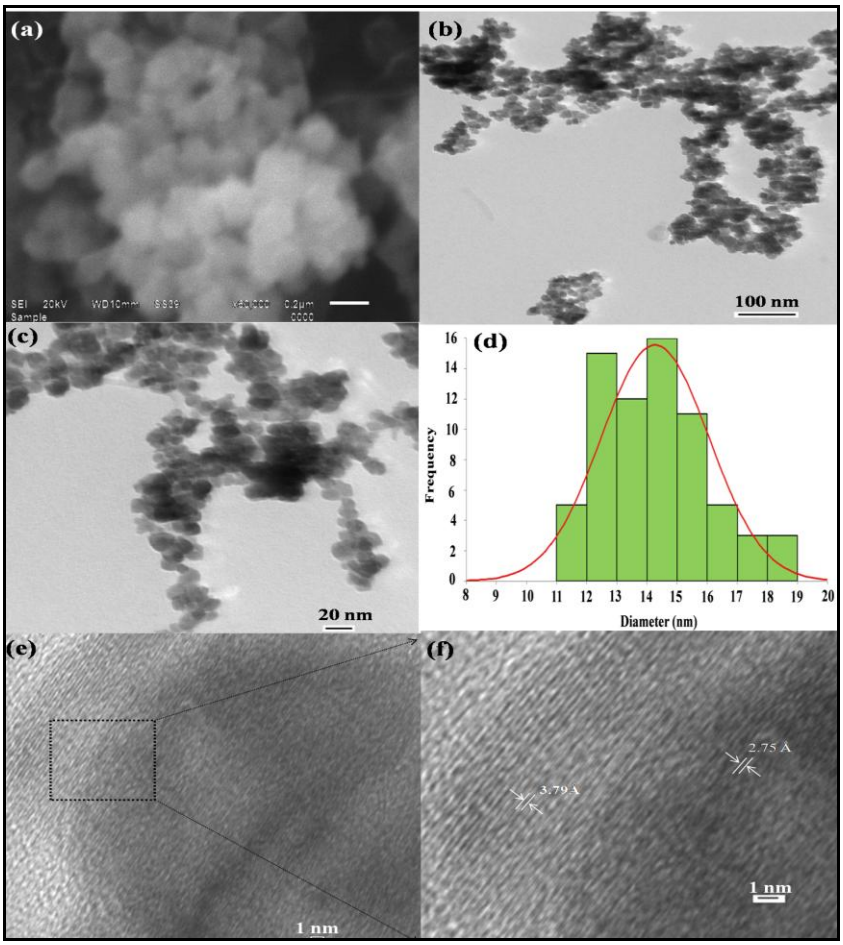

Figure 4.11 (a) SEM (b, c) TEM micrographs (d) histogram and (e, f) HRTEM images of PEG coated potassium ferrite nanoparticles

The spherical formation with reduced agglomeration of the synthesized nanocomposite is well-evident from figs. 4.11(a-c). The size distribution ranges from 11-19 nm and the

maximum frequency (diameter of the nanocomposite) lie in the range 14-15 nm, as depicted by the histogram in fig. 4.11(d). The lattice fringes corresponding to PEG and potassium ferrite nanoparticles have been well-observed in fig. 4.11(f).

4.2.2.5 Magnetic analysis

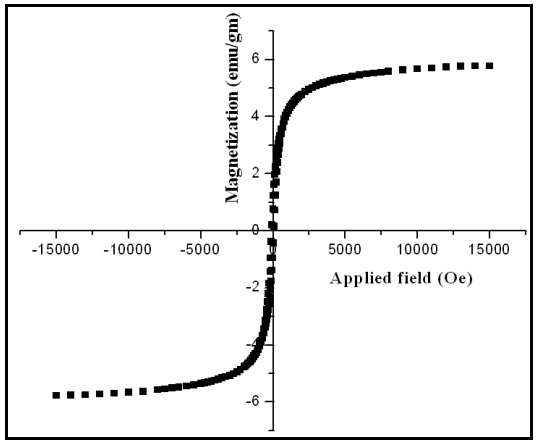

Figure 4.12 M-H curve of PEG coated potassium ferrite nanoparticles

M-H curve of PEG coated potassium ferrite nanoparticles, as studied by VSM, in fig. 4.12, suggests its superparamagnetic behaviour. The magnetic saturation (M_S), remanent magnetization (M_R) and squareness value (M_R/M_S ratio) for potassium ferrite nanoparticles, as obtained, are 5.78 emu/g, 0.74emu/g and 0.12, respectively. Superparamagnetic behavior is characterized by less squareness value [17]. For non-interacting superparamagnetic particles, it is 0.5 [58], in case of interacting superparamagnetic particles the dipolar interactions reduce both the magnetic squareness (M_R/M_S ratio) and coercivity (H_C) values due to demagnetizing effect [58, 59]. Magnetic squareness value related to superparamagnetic behaviour is 0.1, i.e. it loses greater than 90% of its magnetism on removal of the applied magnetic field [60]. The squareness value of PEG coated potassium ferrite nanoparticles is 0.12. Therefore, it exhibits the

characteristic feature of superparamagnetism. The reduction in the magnetic saturation value (as compared to the bare potassium ferrite nanoparticles, fig. 4.5) is attributed to the chemical combination of non-magnetic layer of PEG on the surface of potassium ferrite nanoparticles. The particle size and its distribution decide the form of magnetization curve, which is further related to the magnetic particle content. Therefore, a non-magnetic surface coating on the particle results in the reduction of the magnetic size as compared to its physical size [143, 144], thus, diminishing the magnetic saturation value. The larger size of the nanocomposite results in higher magneto-crystalline anisotropy for the nanocomposite. The magneto-crystalline anisotropy originates from the coupling between electron spins and the angular momentum of the electron orbital (L-S coupling). Superparamagnetic behaviour of a particle, which is directly related to its magneto-crystalline anisotropy, is correlated to its L-S coupling, as well [56, 57].This is directly proportional to the volume of particles ($EA = KV \sin^2\theta$), where, K is the magneto-crystalline anisotropy constant (related to the strength of the L-S coupling), V is the volume of the nanoparticle and θ is the angle between the magnetization direction and the easy axis of the nanoparticle. EA serves as an energy barrier for blocking the flips of magnetic moments [56, 57]. The total effective magnetic moment of PEG coated nanoparticles is found to decrease, which is most probably due to a non-collinear spin structure originating from the pinning of the surface spins and PEG coating at the interface of nanoparticles [145]. However, coating of the nanoparticles with PEG did not affect the super paramagnetic nature of the synthesized potassium ferrite nanoparticles, as evidenced in fig. 4.12.

4.2.2.6 Cytotoxicity analysis

The experimental procedure is same as discussed in section 3.2.6.1. Following are the results obtained.

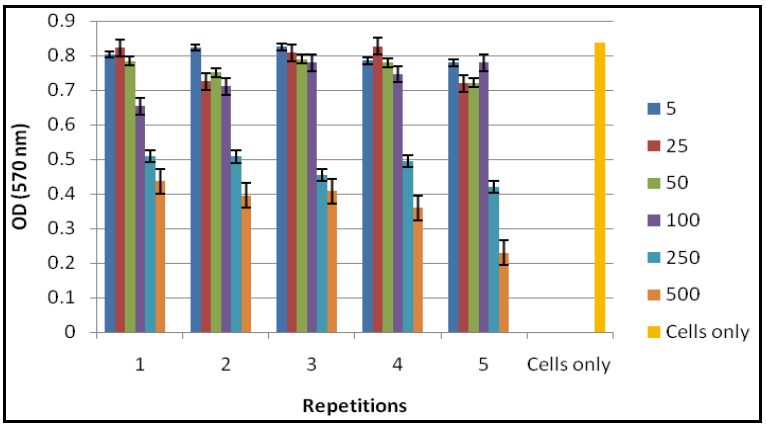

Figure 4.13 Optical Density (OD) at 570 nm of all repetitions at all concentrations

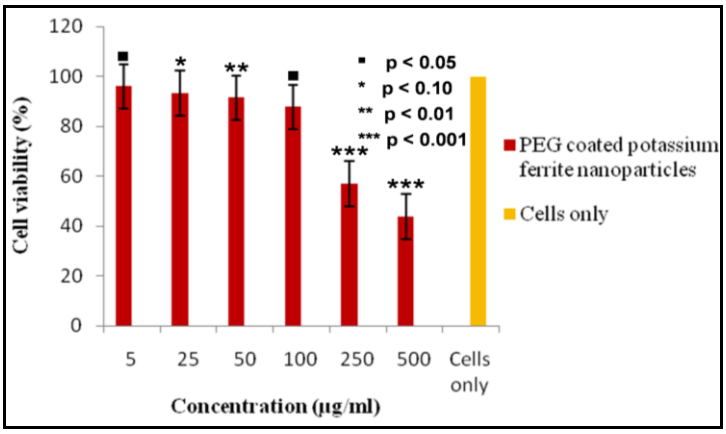

Figure 4.14 Mean cell viability (%) as determined by MTT assay, with values presented as ▪ p < 0.05 *p < 0.10, **p < 0.01, ***p < 0.001, compared with untreated cells (dependent student's t-test)

Dose-dependent cytotoxicity of the nanocomposite tested on T-cell lines (Jurkat cells) using MTT assay reveals their non-toxic behaviour. Fig. 4.13 shows the optical density (OD) values of all repetitions at all concentrations. The cell viabilities at 5, 25, 50, 100, 250, 500µg/ml, calculated according to Eq. 3.2 are 95.9%, 93.1%, 91.3%, 87.6%, 57%, 43.6%. In fig. 4.14, the statistical analysis using paired t-test [134] has been determined to scrutinize the effect of

synthesized nanocomposite on the cells. PEG is a well known biocompatible material and it leads to reduced agglomeration. Therefore, the enhanced cell viability is attributed to these two factors which encourages their intracellular uptake and reduced cellular damage [48]. A significant cell viability has been observed below 500 µg/ml, and a fall occurs at 500µg/ml; this may be attributed to scarcity of culture media during the growth of the cells while running the assay, rather than any toxicity of the synthesized nanocomposite. On interaction, the nanocomposite first attaches to cells, then is internalized by endocytosis, finally gets accummulated in digestive vacuoles [70]. Therefore, at higher concentration, the overloading of particles possibly resulted in cell death.

4.3 Silica coated potassium ferrite nanoparticles

4.3.1 Experimental procedure

To synthesize silica coated potassium ferrite nanoparticles, stober process was used with some modifications [43]. Briefly, 2.0g of the calcined nanoparticles were mixed with ethanol and water ($V_{E/W} = 4$) as well as ammonia solution. The mixture was ultrasonically mixed and to this required amount of TEOS solution was added. The hydrolysis of the alkoxy groups of the silica precursor (TEOS) leads to the formation of silanol groups (Si-OH), as shown in eq. 4.1 and fig. 4.15. Ammonia solution neutralizes the pH of the mixture, shifting the reaction to basic conditions where the hydroxide anions play the role of basic catalysts for poly-condensation. This step leads to the formation of oxo-bridged Si-O-Si groups and therefore to the interconnectivity of the silica network [153], as shown in Eqs. 4.2, 4.3 and fig. 4.15. The solution was mechanically stirred for 12 hour, resulting in formation of silica coated potassium ferrite nanoparticles. After 12 hour stirring, the nanoparticles were magnetically separated by

placing the solution on a magnetic slab of surface field 2T. The magnetic nanoparticles settled at the bottom and the solution was carefully removed by a syringe. The obtained product was washed several times with ethanol by centrifugation at 2000 rpm. It was dried overnight in a vacuum oven at 60°C. Finally, silica coated potassium ferrite nanoparticles were obtained.

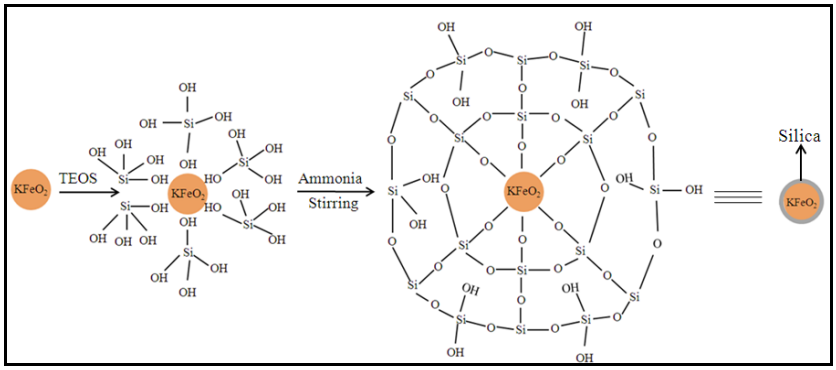

Figure 4.15 Schematic representation of synthesis of silica coated potassium ferrite nanoparticles

In general, the hydrolysis reaction of TEOS on the surface of potassium ferrite nanoparticles produces the singly-hydrolyzed monomer - $(OR)_3Si(OH)$, Eq. 4.1 [89].

$$Si(OR)_4 + xH_2O + NH_3 \rightarrow (\overset{-}{O})_xSi(OR)_{4-x} + xROH + NH_4^+ \quad (4.1)$$

These intermediate reaction products participate in the condensation reactions (Eqs. (4.2) and (4.3)), and finally silica coated nanocomposite is formed [89].

$$Si(OR)_4 + (OH)Si(OR)_3 \rightarrow (OR)_3Si\text{-}O\text{-}Si(OR)_3 + ROH \quad (4.2)$$

$$(OR)_3Si(OH) + (OH)Si(OR)_3 \rightarrow (OR)_3Si\text{-}O\text{-}Si(OR)_3 + H_2O \quad (4.3)$$

4.3.2 Results and discussion

4.3.2.1 Structural analysis

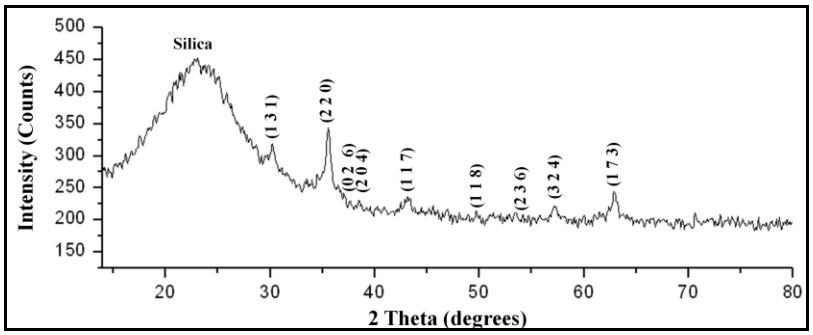

Figure 4.16 XRD pattern of silica coated potassium ferrite nanoparticles

Fig. 4.16 shows the XRD diffractogram of silica coated potassium ferrite nanoparticles, where all the peaks are indexed and well-matched to the orthorhombic structure (File No. 83-2152, space group: *Pbca*) of $KFeO_2$, a broad band near 2θ ~ 20-25° has been observed pertaining to silica coating on potassium ferrite nanoparticles; this broad band demonstrates the existence of amorphous silica shell on the nanoparticles. Less intensity of $KFeO_2$ core is attributed to the silica coating which diminishes the peak intensities [146]. It also indicates that the crystallinity of the magnetic nanoparticles is retained after the silica coating. The calculated lattice parameter values have been tabulated in table 4.5.

Table 4.5 Theoretical and calculated values of unit cell parameters of silica coated potassium ferrite nanoparticles

Silica coated $KFeO_2$				
		Theoretical	Calculated	Difference
Unit cell parameters	a	5.577	5.724	0.147
	b	11.22	10.62	0.600
	c	15.89	14.52	1.370

4.3.2.2 Thermal analysis

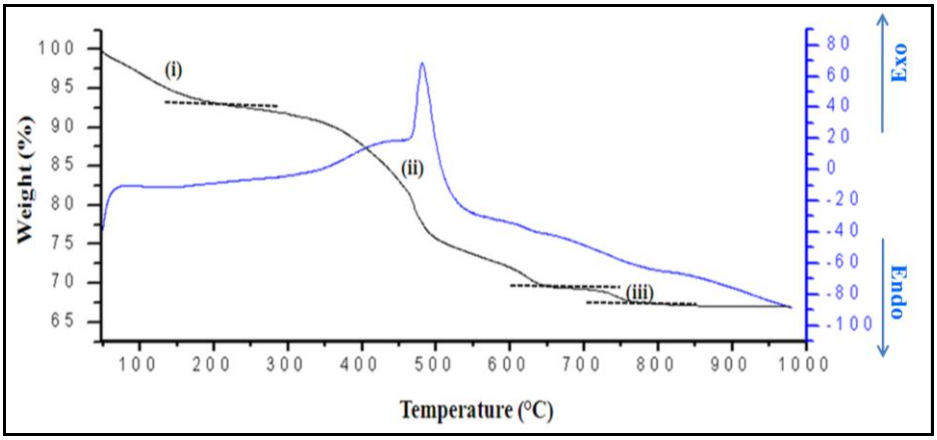

Figure 4.17 TGA and DTA curves of silica coated potassium ferrite nanoparticles

In fig. 4.17, the TG curve exhibits a broad continuous weight loss in three regions. The first region (i) of the weight loss from room temperature to around 200° C can be attributed to the loss of physically adsorbed water and gases on the surface of silica coated potassium ferrite nanoparticles [25]. The broad weight loss in the second region, (ii), comprises of two steps; the initial weight loss (200-350°C) is possibly due to decomposition/combustion of TEOS and the weight loss at higher temperature (350-650°C) is associated with the condensation of silanol in the silica shell [50, 147], where the corresponding exothermic peak at 481°C can be well observed. The small weight loss (650-760°C) in TGA and broad exothermic curve in DTA, in third region (iii), can be attributed to the removal of structural water (dehydroxylation) [148, 149]. There is no loss of weight in the TGA curves above 760°C; showing that the silica coated potassium ferrite nanoparticles are stable in this temperature range.

4.3.2.3 FTIR analysis

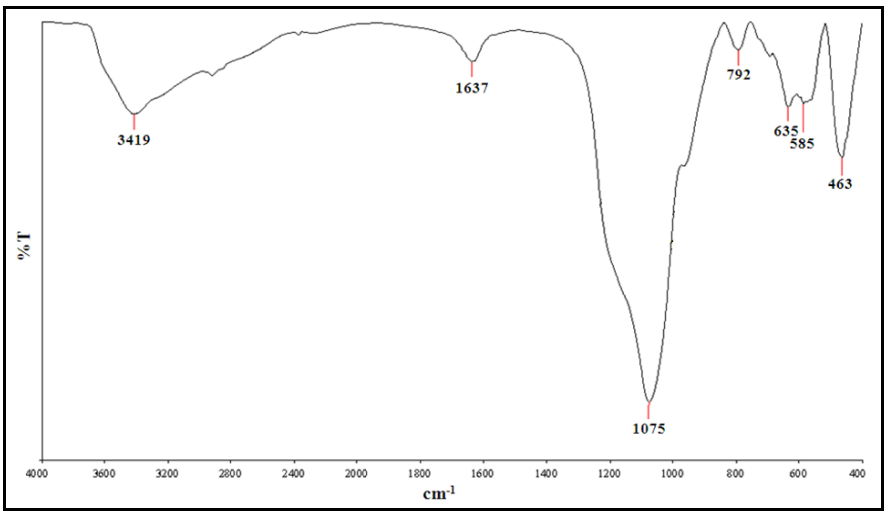

Figure 4.18 FTIR spectrum of silica coated potassium ferrite nanoparticles

In the FTIR spectrum, fig. 4.18, of silica coated potassium ferrite nanoparticles, the broad stretch at 3419cm^{-1} and 1637cm^{-1} is due to O-H stretching and bending vibrations, respectively, pertaining to adsorbtion of atmospheric water on the surface of the synthesized nanoparticles [116, 138]. The characteristic sharp absorption band at 1075cm^{-1} is assigned to the asymmetric stretching vibration of Si-O-Si [51, 154]. The bending vibration of O–Si–O group appears at 463cm^{-1} and the band at 792cm^{-1} depicts the characteristic vibration of Si–OH, hence confirming the presence of silica in the nanocomposite [50]. The band of silanol group (Si-OH) exists at the surface of the synthesized nanocomposite. The bands at 635cm^{-1} and 585cm^{-1} correspond to Fe-O bond due to the ferrite skeleton [61]. The description of the FT-IR spectrum of silica coated potassium ferrite nanoparticles has been tabulated in table 4.6.

Table 4.6 Description of FTIR spectrum of silica coated potassium ferrite nanoparticles

Silica coated potassium ferrite nanoparticles	IR band (cm^{-1})	Description
	3419	ν(OH) stretching
	1637	ν(OH) bending
	1075	ν_{as}(Si-O-Si) stretching
	792	ν(Si-OH) stretching
	635, 585	ν(Fe-O) stretching
	463	ν(O-Si-O) bending

4.3.2.4 Morphological analysis

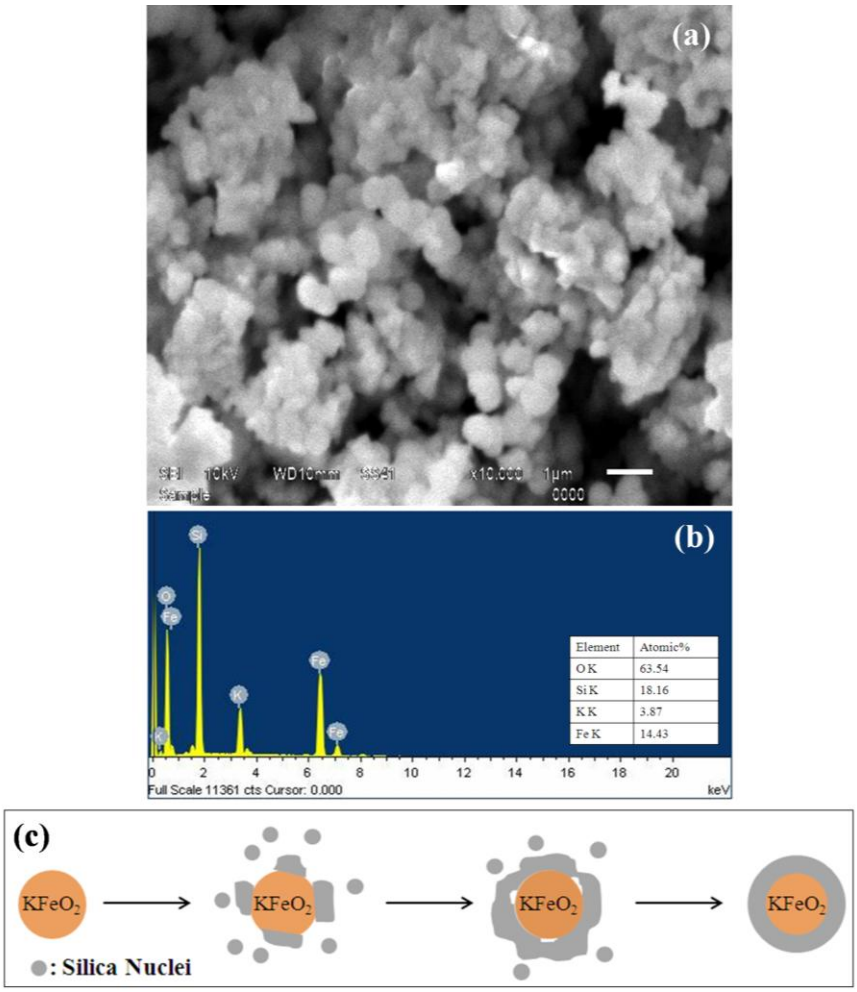

Figure 4.19 (a, b) SEM and EDAX of silica coated potassium ferrite nanoparticles (c) schematic representation of the proposed mechanism of silica growth on potassium ferrite nanoparticles

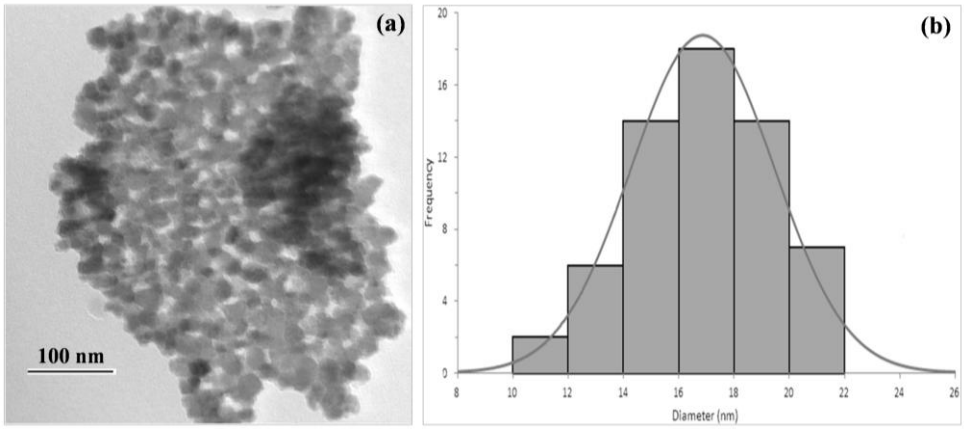

Figure 4.20 (a) TEM micrograph, (b) histogram of silica coated potassium ferrite nanoparticles

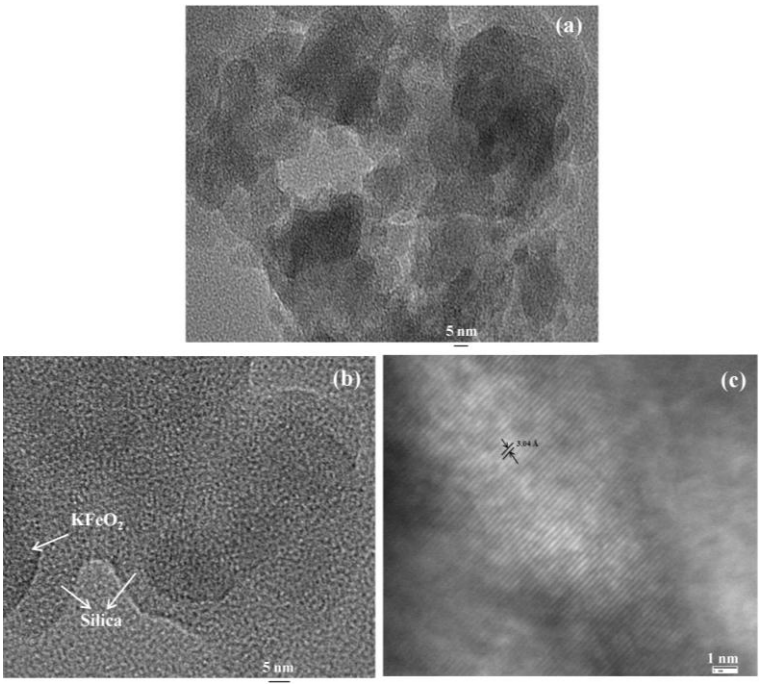

Figure 4.21 HRTEM image of silica coated potassium ferrite nanoparticles at scale of (a, b) 5 nm (c) 1 nm

Fig. 4.19(a) shows the SEM micrograph depicting the spherical formation of the silica coated potassium ferrite nanoparticles with reduced agglomeration. EDAX pattern (fig. 4.19(b)) along with the table depicting the atomic% values of the elements observed is also shown. These features have also been observed in the TEM micrograph (fig. 4.20(a)), with a size distribution of

about 10-22 nm, as depicted by the histogram (fig. 4.20(b)). The reduction in the agglomeration can be well observed pertaining to the silica coating on potassium ferrite nanoparticles.

HRTEM images in fig. 4.21 further confirm the presence of silica coating on potassium ferrite nanoparticles, depicting the amorphous nature of silica. In fig. 4.21(b), the presence of silica layer on potassium ferrite nanoparticles is well-evident from the contrast of dark $KFeO_2$ core and amorphous silica surrounding it. In fig. 4.21(c), the lattice fringes corresponding to potassium ferrite nanoparticles can be well observed. The lattice spacing between the two adjacent planes is 3.04 Å, which corresponds very well to the d-spacing for (1 3 1) lattice plane of potassium ferrite nanoparticles ($KFeO_2$ NPs).

4.3.2.4.1 Mechanism of silica coating on potassium ferrite nanoparticles

The formation of pure silica colloids has been explained by the aggregation model and the monomer addition model [155-157]. In the aggregation model, both nucleation and aggregation processes proceed simultaneously in the solution. As soon as TEOS precursor is added, the nucleation process begins, but pertaining to its instability it tends to aggregate depending on the experimental conditions such as ammonia, water and silane concentration [155, 156]. Whereas in the monomer addition model, the nucleation begins with the condensation of two hydrolyzed TEOS monomers and nuclei grow by monomer addition depending on the reaction rates and particle size [155, 157]. In the FTIR spectrum (fig. 4.18), no bands related to unreacted TEOS or pure silica has been observed. Also, in SEM, TEM and HRTEM micrographs (figs. 4.19-4.21), we rarely observed the existence of pure silica particles. These observations imply that the coating mechanism did not follow the monomer addition model, since consecutive monomer addition would have produced pure silica particles.

Therefore, the mechanism of silica coating on potassium ferrite nanoparticles and their morphological changes observed in the SEM micrograph (fig. 4.19 (a), can be well-explained by the aggregation model. At the early stage of the reaction (fig. 4.19 (c)), the aggregation event becomes dominant, because $KFeO_2$ core is already present in the solution and when TEOS precursor is added, silica nuclei start aggregating on some parts of its surface, to form an island-like structure. The islands keep touching each other and keep growing slowly. During the growth process, fresh nuclei keep filling the unfilled spaces for a smoother surface. As the possibility of nuclei aggregation during the growth process is statistically equal in all directions, it becomes more and more spherical in shape. This accounts for the radical change in morphological characteristics on silica coating, leading to spherical formation of the nanocomposite.

4.3.2.5 Magnetic analysis

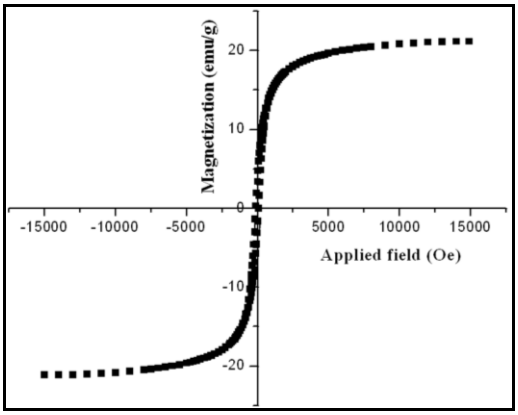

Figure 4.22 M-H curve of silica coated potassium ferrite nanoparticles

The magnetic response of silica coated potassium ferrite nanoparticles, as shown in fig. 4.22, suggests it superparamagnetic behaviour. The magnetic saturation (M_S) value, remanent

magnetization (M_R) and squareness value (M_R/M_S ratio) of 21.17emu/g, 3.25emu/g and 0.15, respectively. The squareness value obtained from the M-H curve determines the magnetic behaviour; high value denotes ferromagnetism and small value denotes superparamagnetism [17, 152]. Small squareness value obtained from the M-H curve reflects the superparamagnetic behavior of the coated nanoparticles [17]. For non-interacting superparamagnetic particles, the squareness value is 0.5, while in the case of interacting superparamagnetic particles, demagnetizing effects prevail due to the reduction in dipolar interactions, which further reduce both the magnetic squareness (M_R/M_S ratio) and coercivity (H_C) values [58, 59]. Magnetic squareness value ascribable to superparamagnetic behaviour is 0.1, i.e. it loses greater than 90% of its magnetism on removal of the applied magnetic field [60]. The squareness value, as obtained for silica coated potassium ferrite nanoparticles is 0.15. Therefore, it can be comprehended that it exhibits the characteristic feature of superparamagnetism. The magnetic behaviour of nanocomposite and magnetic dynamics, using core-shell model, strongly relates the competitive magnetic ordering between core and shell (surface) spins to surface spin configuration and inter-particle (dipole-dipole) interactions [158]. Considering the above, in $KFeO_2$-silica nanocomposite, the magnetic ordering of the core spins dominates that of the silica shell, thus maintaining the superparamagnetic character of $KFeO_2$ core. But, a reduction in the magnetic saturation value has been observed for silica coated potassium ferrite nanoparticles; this is credited to the chemical combination of nonmagnetic layer of silica on potassium ferrite nanoparticles. It is well known that the form of magnetization curve is dependent to particle size and size distribution, which in this case is connected to the magnetic particle content. Thus, if there is a non-magnetic surface coating on the magnetic particle, the magnetic size measured will be smaller than the physical size [143, 144]. The magnetically dead

layer of silica coating makes the magnetic diameter of the particles smaller than its physical size, thereby resulting in reduction in magnetic saturation, Ms value [143, 144]. The total effective magnetic moment of silica coated nanoparticles is found to decrease, this occurs due to a non-collinear spin structure originating from the pinning of the surface spins and silica coating, at the interface of nanoparticles [145]. The measured magnetization in silica coated potassium ferrite nanoparticles decreases due to the higher contribution of the non-magnetic coating mass (silica) to the total sample volume, which quenches the surface moment [28].

4.3.2.6 Cytotoxicity analysis

The experimental procedure is same as discussed in section 3.2.6.1 with 4 replicates. Following are the results obtained.

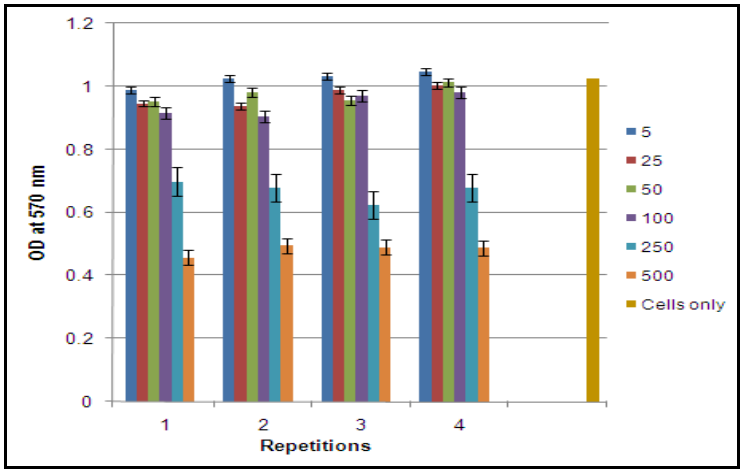

Figure 4.23 Optical Density (OD) at 570 nm of all repetitions at all concentrations

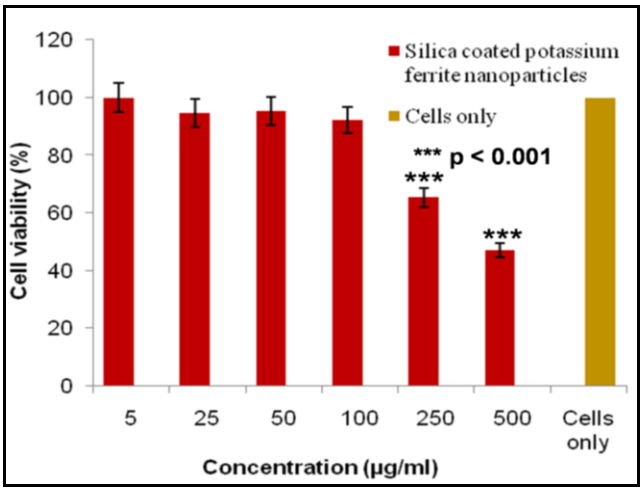

Figure 4.24 Mean cell viability (%) as determined by MTT assay, with values presented as ***$p < 0.001$ compared with untreated cells (dependent student's t-test)

The cell viabilities at 5, 25, 50, 100, 250, 500µg/ml, calculated according to Eq. 3.2 are 100%, 94.7%, 95.3%, 92.1%, 65.4%, 47.1 %, respectively. Fig. 4.23 shows the optical density (OD) values of all repetitions (n = 4) at all concentrations. The effect of synthesized nanocomposite on the cells has been studied by the statistical analysis using paired t-test [134], as shown in fig. 4.24. It is well observed that the silica coated potassium ferrite nanoparticles exhibit enhanced cell viability at all concentrations as compared to bare potassium ferrite nanoparticles. This is attributed to good dispersibilty of silica coated potassium ferrite nanoparticles in the medium. Silica protects nanoparticles from acidic erosion. Correspondingly, the particle stability converts into reduced cytotoxicity [45]. The well-dispersion of nanoparticles results in their relatively less aggregation, this facilitates their intracellular uptake and hampers cellular damage [48]. A significant cell viability has been observed below 100 µg/ml, and a considerable fall in the viability occurs at the concentration of 250 and 500µg/ml; this may be attributed to shortage of culture media required for the growth of the cells while running the assay, rather than any toxicity of the synthesized nanocomposite. Mostly, on exposure the

nanoparticles first get adhered to cells, then owing to endocytosis are internalized and are accummulated in digestive vacuoles [70]. At higher concentrations, the overloading of particles occurs and this consequently results in fatality of cells. The silica layer on potassium ferrite nanoparticles reduces the cellular toxicity, enhancing their possible biomedicinal applications.

Chapter – 5

CONCLUSIONS

AND

FUTURE PLAN

Chapter 5

This chapter includes the conclusions and summary of the thesis, along with an insight into the future possibilities of the present research work.

5.1 Conclusions

In the present thesis, two materials viz. calcium ferrite nanoparticles ($CaFe_2O_4$ NPs) and potassium ferrite nanoparticles ($KFeO_2$ NPs) have been studied. Both these materials have been further coated with polyethylene glycol (PEG) and silica. The structural, morphological, thermal, FTIR, magnetic and cytotoxicity analyses of all the combinations mentioned above have been studied. The research work presented comprises of two sections with three combinations each, as follows.

I. Calcium ferrite nanocomposites

1. Calcium ferrite nanoparticles

» The synthesis of calcium ferrite nanoparticles was done by sol-gel method.

» XRD pattern showed the formation of orthorhombic structure of $CaFe_2O_4$.

» The thermal and FTIR analyses confirmed the nanoparticles to be free from any impurity and unreacted precursors.

» SEM and EDAX analyses revealed their agglomerated formation with the required elemental composition. In the TEM micrograph, spherical morphology with size distribution in the range ~5-11 nm was observed.

» In the magnetic analysis by VSM, superparamagnetic behaviour with magnetic saturation (M_s), remanent magnetization (M_R) and squareness (M_R/M_S ratio) values of 36.76emu/g, 0.24emu/g and 0.006, respectively was observed.

» In vitro cytotoxicity test on T cell lines (Jurkat cells), using MTT assay, exhibited their dose-dependent cytotoxicity, wherein the nanoparticles were biocompatible at a particle concentration below 250µg/ml.

2. PEG coated calcium ferrite nanoparticles

» Hydrothermal method was used for the synthesis of PEG coated calcium ferrite nanoparticles.

» XRD pattern showed the formation of orthorhombic structure of $CaFe_2O_4$ with additional characteristic peaks of PEG at 2θ ~19° and 23°.

» The delayed decomposition of the nanocomposite in the thermal analysis was attributed to the covalent formation of PEG with calcium ferrite nanoparticles.

» The characteristic bands of PEG in the FTIR spectrum further confirmed its coating.

» SEM and TEM micrographs revealed the reduced agglomerated formation with spherical morphology in the size range 10.0-16.5 nm. Lattice fringes corresponding to

PEG and calcium ferrite nanoparticles, as obtained in the HRTEM image, corroborated the PEG coating.

» In the magnetic analysis by VSM, superparamagnetic behaviour with magnetic saturation (M_s), remanent magnetization (M_R) and squareness (M_R/M_S ratio) values of 6.74emu/g, 0.89emu/g and 0.119, respectively was observed. The reduction in the M_S value, as compared to bare nanoparticles is attributed to the magnetically dead layer of polymer PEG on the surface of the nanoparticles.

» In vitro cytotoxicity test on T cell lines (Jurkat cells), using MTT assay, exhibited their dose-dependent cytotoxicity, wherein the nanoparticles were biocompatible at a particle concentration below 250µg/ml. The nanocomposite exhibited greater cellular viability at all concentrations compared to the bare calcium ferrite nanoparticles owing to relatively less agglomeration and biocompatibility of polymer PEG.

3. Silica coated calcium ferrite nanoparticles

» The synthesis of silica coated calcium ferrite nanoparticles was done by modified stober method.

» The XRD pattern showed the formation of orthorhombic structure of $CaFe_2O_4$ with a broad band near $2\theta \sim 15\text{-}20°$ corresponding to amorphous silica. Silica coating diminished the peak intensities of the $CaFe_2O_4$ core.

» In the FTIR and thermal analyses, detection of characteristic bands of silanol and condensation of silanol group, respectively, confirmed its coating in the nanocomposite.

» SEM and EDAX analyses revealed their spherical formation with the required elemental composition.

» In the TEM micrograph, spherical morphology with size distribution in the range ~3-6 nm was observed. The amorphous nature of silica and lattice fringes corresponding to calcium ferrite nanoparticles was obtained in the HRTEM image.

» In the magnetic analysis by VSM, superparamagnetic behaviour with magnetic saturation (M_s), remanent magnetization (M_R) and squareness (M_R/M_S ratio) values of 8.55emu/g, 1.05emu/g and 0.122, respectively was observed. The reduction in the M_S value, as compared to bare nanoparticles is attributed to the magnetically dead layer of silica on the surface of the nanoparticles, while it is greater as compared to PEG coated calcium ferrite nanoparticles.

» In vitro cytotoxicity test on T cell lines (Jurkat cells), using MTT assay, exhibited their dose-dependent cytotoxicity, wherein the nanoparticles were biocompatible at a particle concentration below 500µg/ml. The nanocomposite exhibited greater cellular viability at all concentrations compared to the bare and PEG coated calcium ferrite nanoparticles owing to its agglomeration-free formation which led to good dispersion in the medium and biocompatibility of silica.

Table 5.1 summarises the various parameters obtained for the bare, PEG coated and silica coated calcium ferrite nanoparticles ($CaFe_2O_4$ NPs).

Table 5.1 A comparison of the various parameters obtained for bare, PEG coated and silica coated calcium ferrite nanoparticles ($CaFe_2O_4$ NPs)

	Structure and particle size range (nm)	*Magnetic behaviour and parameters*			*Cell-viability (%) Concentration (µg/ml)*					
					5	25	50	100	250	500
$CaFe_2O_4$ NPs	Orthorhombic ~5-11	Superparamagnetic			99.7	95.7	94.7	91.1	36.3	30.8
		M_S (emu/g)	M_R (emu/g)	M_R/M_S						
		36.76	0.24	0.006						
PEG coated $CaFe_2O_4$ NPs	Orthorhombic with PEG peaks at ~ 19° and 23° ~10.0-16.5	Superparamagnetic			102.9	98.8	95.3	89.9	62.8	44.6
		M_S (emu/g)	M_R (emu/g)	M_R/M_S						
		6.74	0.89	0.119						
Silica coated $CaFe_2O_4$ NPs	Orthorhombic with silica broad band at ~ 15- 20° ~3-6	Superparamagnetic			103.9	103.7	99.6	95.6	81.3	74.2
		M_S (emu/g)	M_R (emu/g)	M_R/M_S						
		8.55	1.05	0.122						

II. Potassium ferrite nanocomposites

1. Potassium ferrite nanoparticles

» The synthesis of potassium ferrite nanoparticles was done by sol-gel method.

» XRD pattern showed the formation of orthorhombic structure of $KFeO_2$.

» The thermal and FTIR analyses confirmed the nanoparticles to be free from any impurity and unreacted precursors.

» SEM and EDAX analyses revealed their agglomerated formation with the required elemental composition. In the TEM micrograph, spherical morphology with size distribution in the range ~4-8 nm was observed.

» In the magnetic analysis by VSM, superparamagnetic behaviour with magnetic saturation (M_s), remanent magnetization (M_R) and squareness (M_R/M_S ratio) values of 49.01emu/g, 4.34emu/g and 0.08, respectively was observed.

» In vitro cytotoxicity test on T cell lines (Jurkat cells), using MTT assay, exhibited their dose-dependent cytotoxicity, wherein the nanoparticles were biocompatible at a particle concentration below 250µg/ml.

2. PEG coated potassium ferrite nanoparticles

» The synthesis of PEG coated potassium ferrite nanoparticles was done by hydrothermal method.

» XRD pattern showed the formation of orthorhombic structure of $KFeO_2$ with additional characteristic peaks of PEG at 2θ ~19° and 23°.

» The delayed decomposition of the nanocomposite in the thermal analysis was attributed to the covalent formation of PEG with potassium ferrite nanoparticles.

» The characteristic bands of PEG in the FTIR spectrum further confirmed its coating.

» SEM and TEM micrographs revealed the reduced agglomerated formation with spherical morphology in the size range 11-19 nm. Lattice fringes corresponding to PEG and potassium ferrite nanoparticles, as obtained in the HRTEM image, corroborated the PEG coating.

» In the magnetic analysis by VSM, superparamagnetic behaviour with magnetic saturation (M_s), remanent magnetization (M_R) and squareness (M_R/M_S ratio) values of 5.78emu/g, 0.74emu/g and 0.12, respectively was observed. The reduction in the M_S value, as compared to bare nanoparticles is attributed to the magnetically dead layer of polymer PEG on the surface of the nanoparticles.

» In vitro cytotoxicity test on T cell lines (Jurkat cells), using MTT assay, exhibited their dose-dependent cytotoxicity, wherein the nanoparticles were biocompatible at a particle concentration below 250µg/ml. The nanocomposite exhibited greater cellular viability at all concentrations compared to the bare potassium ferrite nanoparticles owing to relatively less agglomeration and biocompatibility of polymer PEG.

3. Silica coated potassium ferrite nanoparticles

» The synthesis of silica coated potassium ferrite nanoparticles was done by stober method.

» XRD pattern showed the formation of orthorhombic structure of $KFeO_2$ with a broad band near $2\theta \sim 20\text{-}25°$ corresponding to amorphous silica. Silica coating diminished the peak intensities of the $KFeO_2$ core.

» In the FTIR and thermal analyses, detection of characteristic bands of silanol and condensation of silanol group, respectively, confirmed its coating in the nanocomposite.

» SEM and EDAX analyses revealed their spherical formation with the required elemental composition.

» In the TEM micrograph, spherical morphology with size distribution in the range ~10-22 nm was observed. The amorphous nature of silica and lattice fringes corresponding to potassium ferrite nanoparticles was obtained in the HRTEM image.

» In the magnetic analysis by VSM, superparamagnetic behaviour with magnetic saturation (M_s), remanent magnetization (M_R) and squareness (M_R/M_S ratio) values of 21.17emu/g, 3.25emu/g and 0.15, respectively was observed. The reduction in the M_S value, as compared to bare nanoparticles is attributed to the magnetically dead layer of silica on the surface of the nanoparticles, while it is greater as compared to PEG coated potassium ferrite nanoparticles.

» In vitro cytotoxicity test on T cell lines (Jurkat cells), using MTT assay, exhibited their dose-dependent cytotoxicity, wherein the nanoparticles were biocompatible at a particle concentration below 500µg/ml. The nanocomposite exhibited greater cellular viability at all concentrations compared to the bare and PEG coated potassium ferrite nanoparticles owing to good dispersion in the medium and biocompatibility of silica.

Table 5.2 summarises the various parameters obtained for the bare, PEG coated and silica coated potassium ferrite nanoparticles ($KFeO_2$ NPs).

Table 5.2 A comparison of the various parameters obtained for bare, PEG coated and silica coated potassium ferrite nanoparticles ($KFeO_2$ NPs)

	Structure and particle size range (nm)	*Magnetic behaviour and parameters*			*Cell-viability (%) Concentration (µg/ml)*					
					5	25	50	100	250	500
$KFeO_2$ NPs	Orthorhombic ~4-8	Superparamagnetic			96.7	92	90.9	84.8	43.1	35.5
		M_S (emu/g)	M_R (emu/g)	M_R/M_S						
		49.01	4.34	0.08						
PEG coated $KFeO_2$ NPs	Orthorhombic with PEG peaks at ~ 19° and 23° ~11-19	Superparamagnetic			95.9	93.1	91.3	87.6	57	43.6
		M_S (emu/g)	M_R (emu/g)	M_R/M_S						
		5.78	0.74	0.12						
Silica coated $KFeO_2$ NPs	Orthorhombic with silica broad band at ~ 20- 25° ~10-22	Superparamagnetic			100	94.7	95.3	92.1	65.4	47.1
		M_S (emu/g)	M_R (emu/g)	M_R/M_S						
		21.17	3.25	0.15						

5.2 Future plan

The further work can be extended to the concentration dependent cellular viability and superparamagnetism of the synthesized nanocomposites. The formation of drug conjugates with the synthesized nanocomposites and studying their drug release kinetics is another possibility that can be studied, as well. Generally, drug release is an intricate process and is assumed to

include several considerations, such as (i) diffusion through the coating matrix (ii) release by coating degradation (iii) solubilization and diffusion of the drug in the fine pores of the polymer due to polymer erosion. All these parameters need to be comprehensively analysed. Also, drug release not only depends on the molecular weight of the polymer but also on the interfacial properties of the nanoparticles. Their further investigations as hyperthermia agent, contrast enhancement agent in magnetic resonance imaging can also be carried out.

References

[1] J. Mongillo, Nanotechnology 101, Greenwood Press, London, 2007.

[2] M. Hosokawa, K. Nogi, M. Naito, T. Yokoyama, Nanoparticle Technology Handbook, Elsevier, Linacre House, Jordan Hill, UK, 2007.

[3] K. D. Sattler, Handbook of Nanophysics: Nanoparticles and Quantum Dots, CRC Press, Taylor & Francis Group, 2011.

[4] S. P. Gubin, Magnetic nanoparticles, WILEY-VCH Verlag GmbH & Co. KGaA, Weinheim, 2009.

[5] G. Cao, Nanostructures & Nanomaterials - Synthesis, Properties & Applications, Imperial College Press, London, 2004.

[6] S. Kumar, V. Kundu, A. Vohra, S. K. Chakarvarti, J. Mater. Sci.: Mater. Electron. 22 (2011) 995–999.

[7] S. R. Das, S. B. Majumder, R.S. Katiyar, J. Power Sources 139 (2005) 261–268.

[8] N. Ortega, A. Kumar, P. Bhattacharya, S. B. Majumder, R. S. Katiyar, Phy. Rev. B 77 014111 (2008) 1-10.

[9] V. Rotello, Nanoparticles: building blocks for nanotechnology, Springer Science + Business Media, USA, 2004

[10] S. Singh, R. Kaur, J. Chahal, P. Devi, D. V. S. Jain, M. L. Singla, J. Luminescence 141 (2013) 53–59.

[11] P. S. Kohli, P. Devi, P. Reddy, K. K. Raina, M. L. Singla, J. Mater. Sci.: Mater. Electron. 23 (2012) 1891–1897.

[12] N. Singh, A. Agarwal, S. Sanghi, P. Singh, J. Magn. Magn. Mater. 323 (2011) 486–492.

[13] N. Singh, A. Agarwal, S. Sanghi, Curr. Appl. Phys. 11 (2011) 783-789.

[14] P. Yadoji, R. Peelamedu, D. Agrawal, R. Roy, Mater. Sci. Eng. B 98 (2003) 269-278.

[15] B. Roy, S. Das, J. Appl. Phys. 104 (2008) 103915 1-11.

[16] A. Akbarzadeh, M. Samiei, S. Davaran, Nanoscale Res. Lett. 7:144 (2012) 1-13.

[17] W. Zheng, F. Gao, H. Gu, J. Magn. Magn. Mater. 288 (2005) 403–410.

References

[18] M. Arruebo, R. F. Pacheco, M. R. Ibarra, J. Santamaria, Nano Today 2 (2007) 22-32.

[19] A. Ito, M. Shinkai, H. Honda and T. Kobayashi, J. Biosci. Bioeng. 100 (1) (2005) 1-11.

[20] R. Gupta, U. B. Kompella, Nanoparticle Technology for Drug Delivery, Taylor and Francis, London, 2006.

[21] Q. A. Pankhurst, J. Connolly, S. K. Jones, J. Dobson, J. Phys. D: Appl. Phys. 36 (2003) R167-R181.

[22] S. C. McBain, H. H. P. Yiu, J. Dobson, Int. J. Nanomed. 3(2) (2008) 169–180.

[23] Â. Andrade, R. Ferreira, J. Fabris, R. Domingues, in: R. Fazel Rezai (ed.), Biomedical Engineering - Frontiers and Challenges, InTech, Croatia, 2011.

[24] Y. Sun, L. Duan, Z. Guo, Y. DuanMu, M. Ma, L. Xu, Y. Zhang, N. Gu, J. Magn. Magn. Mater. 285 (2005) 65–70.

[25] S. Čampelj, D. Makovec, M. Drofenik, J. Magn. Magn. Mater. 321 (2009) 1346–1350.

[26] H. Yin, H. P. Too, G. M. Chow, Biomater. 26 (2005) 5818–5826.

[27] O. M. Koo, I. Rubinstein, H. Onyuksel, Nanomedicine: Nanotechnol., Biol., Med. 1 (2005) 193-212.

[28] S. Rana, A. Gallo, R. S. Srivastva, R. D. K. Misra, Acta Biomater. 3 (2007) 233-242.

[29] S. Laurent, D. Forge, M. Port, A. Roch, C. Robic, L. V. Elst, R. N. Muller, Chem. Rev. 108 (2008) 2064-2110.

[30] J. Zhang, S. Rana, R. S. Srivastava, R. D. K. Misra, Acta Biomater. 4 (2008) 40–48.

[31] A. S. Karakoti, S. Das, S. Thevuthasan, S. Seal, Angew. Chem. Int. Ed. 50 (2011) 1980 – 1994.

[32] A. Mukhopadhyay, N. Joshi, K. Chattopadhyay, G. De, Appl. Mater. Interfaces 4 (2012) 142-149.

[33] O. Veiseh, J. W. Gunn, M. Zhang, Adv. Drug Deliv. Rev. 62 (2010) 284-304.

[34] M. A. Ahmed, N. Okasha, S. F. Mansour, S. I. El-dek , J. Alloy. Compd. 496 (1-2) (2010) 345–350.

[35] B. Feng, R.Y. Hong, L. S.Wang, L. Guo, H. Z. Li, J. Ding, Y. Zheng, D.G.Wei, Colloids Surf. A: Physicochem. Eng. Asp. 328 (2008) 52–59.

[36] A. K. Gupta, S. Walls, IEEE Trans. Nano Biosci. 3 (1) (2004) 66-73.

[37] Y. Zhang, N. Kohler, M. Zhang, Biomater. 23 (2002) 1553–1561.

References

[38] R. Rastogi, N. Gulati, R. K. Kotnala, U. Sharma, R. Jayasundar, V. Koul, Colloids Surf. B: Biointerfaces 82 (2011) 160-167.

[39] F. Ma, J. Lu, Z. Wang, J. Sun, Q. Gong, B. Song, H. Ai, Z. Gu, Int. J. Magn. Reson. Imaging 2 (2010) 50-55.

[40] M. R. Phadatare, V. M. Khot, A. B. Salunkhe, N. D. Thorat, S. H. Pawar, J. Magn. Magn. Mater. 324 (2012) 770-772.

[41] J. Lee, Y. H. Choa, J. Kim, K. H. Kim, IEEE Trans. Magn. 47(10) (2011) 2874-2877.

[42] Y. P. He, S. Q. Wang, C. R. Li, Y. M. Miao, Z. Y. Wu, B. S. Zou, J. Phys. D: Appl. Phys. 38 (2005) 1342–1350.

[43] Y. H. Deng, C. C. Wang, J. H. Hu, W. L. Yang, S. K. Fu, Colloids Surf. A: Physiochem. Eng. Asp. 262 (2005) 87-93.

[44] J. Lee, Y. Lee, J. K. Youn, H. B. Na, T. Yu, H. Kim, S. M. Lee, Y. M. Koo, J. H. Kwak, H. G. Park, H. N. Chang, M. Hwang, J. G. Park, J. Kim, T. Hyeon, Small 4 (1) (2008) 143-152.

[45] O. Baber, M. Jang, D. Barber, K. Powers, Inhal. Toxicol. 23(9) (2011) 532– 543.

[46] D. Chen, M. Jiang, N. Li, H. Gu, Q. Xu, J. Ge, X. Xia, J. Lu, J. Mater. Chem. 20 (2010) 6422-6429.

[47] L. Sun, Y. Zang, M. Sun, H. Wang, X. Zhu, S. Xu, Q. Yang, Y. Li, Y. Shan, J. Colloid Interface Sci. 350 (2010) 90–98.

[48] R. K. Singh, T. H. Kim, K. D. Patel, J. C. Knowles, H. W. Kim, J. Biomed. Mater. Res. Part A 100A (2012) 1734-1742.

[49] M. Gharagozlou, Chem. Cent. J. 5:19 (2011) 1-7.

[50] H. Wang, J. Huang, L. Ding, D. P. Li, Y. Han, Appl. Surf. Sci. 257 (2011) 7107–7112.

[51] R. Y. Hong, J. H. Li, S. Z. Zhang, H. Z. Li,Y. Zheng, J. M. Ding, D. G. Wei, Appl. Surf. Sci. 255 (2009) 3485-3492.

[52] S. Laureti, G. Varvaro, A. M. Testa, D. Fiorani, E. Agostinelli, G. Piccaluga, A. Musinu, A. Ardu, D. Peddis, Nanotechnol. 21 (2010) 315701 1-6.

[53] S. Larumbe, J. I. P. Landazabal, J. M. Pastor, C. G. Polo, J. Appl. Phys. 111 (2012) 103911 1-8.

References

[54] P. Tartaj, M. D. P. Morales, S. V. Verdaguer, T. G. Carreno, C. J. Serna, J. Phys. D: Appl. Phys. 36 (2003) R182-R197.

[55] D. Vollath, Nanomaterials: An introduction to synthesis, properties and applications, Wiley-VCH Verlag GmbH & Co. KGaA, Weinheim, 2008.

[56] S. Gubbala, H. Nathani, K. Koizol, R. D. K. Misra, Physica B 348 (2004) 317-328.

[57] R. D. K. Misra, S. Gubbala, A. Kale, W.F. Egelhoff Jr., Mater. Sci. Eng. B 111 (2004) 164–174.

[58] K. W. Lee, C. E. Lee, J. Korean Phys. Soc. 59 (2011) L1-L5.

[59] V. Franco, C. F. Conde, A. Conde, L. F. Kiss, Phys. Rev. B 72 (2005) 174424 1-10.

[60] E. V. Groman, L. Josephson, J. M. Lewis, U. S. Patent No. 4951675 (1990).

[61] S. Rana, J. Philip, B. Raj, Mater. Chem. Phys. 124 (2010) 264–269.

[62] R. A. Jalil, Y. Zhang, Biomater. 29 (2008) 4122–4128.

[63] J. Ruan, K. Wang, H. Song, X. Xu, J. Ji, D. Cui, Nanoscale Res. Lett. 6:299 (2011) 1-13.

[64] T. K. Jain, M. A. Morales, S. K. Sahoo, D. L. Leslie-Pelecky, V. Labhasetwar, Mol. Pharm. 2 (3) (2005) 194-205.

[65] A. Jaszczyszyn, K. Gąsiorowski, Adv. Clin. Exp. Med. 17(5) (2008) 525–529.

[66] F. M. Freimoser, C.A. Jakob, M. Aebi, U. Tuor, Appl. Environ. Microbiol. 65(8) (1999) 3727-3729.

[67] H. Yang, C. Zhang, X. Shi, H. Hu, X. Du, Y. Fang, Y. Ma, H. Wu, S.Yang, Biomater. 31 (2010) 3667-3673.

[68] A. M. Alkilany, C. J. Murphy, J. Nanopart. Res. 12 (2010) 2313–2333.

[69] C. Sun, J. S. H Lee and M. Zhang, Adv. Drug Deliv. Rev. 60 (2008) 1252- 1265.

[70] A. Tomitaka, A. Hirukawa, T. Yamada, S. Morishita, Y. Takemura, J. Magn. Magn. Mater. 321 (2009) 1482-1484.

[71] K. C. F. Leung, Y. X. J. Wang, in: Nicoleta Lupu (ed.), Nanowires Science and Technology, Croatia: INTECH, 2010.

[72] S. Mohapatra, S. R. Rout, S. Maiti, T. K. Maiti, A. B. Panda, J. Mater. Chem. 21 (2011) 9185–9193.

[73] G. Baldi, D. Bonacchi, M. C. Franchini, D. Gentili, G. Lorenzi, A. Ricci, C. Ravagli, Langmuir 23 (2007) 4026-4028.

References

[74] H. I. Saleh, J. Mater. Sci. Technol. 20(5) (2004) 530-534.calcium cmpd

[75] R. A. Candeia, M. I. B. Bernardi, E. Longo, I. M. G. Santos, A.G. Souza, Mater. Lett. 58 (2004) 569–572.

[76] J. W. Jeon, S. M. Jung, Y. Sasaki, ISIJ Int. 50(8) (2010) 1064-1070.

[77] D. Hirabayashi, Y. Sakai, T. Yoshikawa, K. Mochizuki, Y. Kojima, K. Suzuki, K. Ohshita, Y. Watanabe, Hyperfine Interact. 167 (2006) 809-813.

[78] I. Ciabatti, F. Tognotti, L. Lombardi, Desalination 250 (2010) 222–228.

[79] J. Q. Jiang, S. Wang, A. Panagoulopoulos, Desalination 210 (2007) 266–273

[80] J. Q. Jiang, A. Panagoulopoulos, M. Bauer, P. Pearce, J. Environ. Manage. 79 (2006) 215–220.

[81] M. Lim, M. J. Kim, Water Air Soil Pollut. 211 (2010) 313–322.

[82] S. Sakka, Handbook of sol-gel science and technology, Volume III: Applications of sol-gel technology, Kluwer academic publishers, USA, 2005.

[83] A. Ulatowska-Jarza, D. Andrzejewski, K. Maruszewski, H. Podbielska, W. Strek, Advantages of sol-gel technologies for biomedical applications, Proc. SPIE 3567, 1999.

[84] M. Niederberger, N. Pinna, Metal oxide nanoparticles in organic solvents-Synthesis, formation, assembly and application, Springer-Verlag London Ltd., 2009.

[85] http://www.centexbel.be/solgel-treatment (last accessed 23-12-13)

[86] K. S. Rao, K. El-Hami, T. Kodaki, K. Matsushige, K. Makino, J. Colloid Interface Sci. 289 (2005) 125–131.

[87] D. A. S. Razo, L. Pallavidino, E. Garrone, F. Geobaldo, E. Descrovi, A. Chiodoni, F. Giorgis, J. Nanopart. Res. 10 (2008) 1225–1229.

[88] I. A. M. Ibrahim, A. A. F. Zikry, M. A. Sharaf, J. Am. Sci. 6 (11) (2010) 985-989.

[89] A. Beganskienė, V.Sirutkaitis, M. Kurtinaitienė, R. Juškėnas, A. Kareiva, Mater. Sci. 10 (4) (2004) 287-290.

[90] M. Frisch, Controlling the hydrothermal conditions to synthesize novel uranium-based heterometallic coordination polymers and their subsequent fluorescence investigations, ProQuest LLC, 2008.

[91] B. Lee, S. Komarneni, Chemical Processing of Ceramics, Second Edition, CRC press, Taylor & Francis group, 2005.

References

[92] M. Birkholz, Thin Film Analysis by X-Ray Scattering, WILEY-VCH Verlag GmbH & Co. KGaA, Weinheim, 2006.

[93] http://www.scienceinschool.org/print/3380 (last accessed 23-12-13)

[94] http://chemwiki.ucdavis.edu/Analytical_Chemistry/Instrumental_Analysis/Diffraction/Powder_X-ray_Diffraction (last accessed 23-12-13)

[95] http://serc.carleton.edu/research_education/geochemsheets/techniques/XRD.html (last accessed 23-12-13)

[96] http://www.intechopen.com/download/get/type/pdfs/id/30948 (last accessed 23-12-13)

[97] https://imf.ucmerced.edu/downloads/semmanual.pdf (last accessed 23-12-13)

[98] B. L. Gabriel, SEM: A user's manual for materials science, American society for metals, USA, 1985.

[99] http://www.nanotechftm.tmf.bg.ac.rs/images/stories/dokumenti/lecture_book_em_school/tamara%20radetic.pdf (last accessed 28-12-13).

[100] http://www.hht-eu.com/cms/5405.html (last accessed 23-12-13)

[101] http://www.microscopemaster.com/scanning-electron-microscope.html (last accessed 23-12-13)

[102] http://micron.ucr.edu/public/manuals/Tem-intro.pdf (last accessed 23-12-13)

[103] http://www.hk-phy.org/atomic_world/tem/tem02_e.html (last accessed 23-12-13)

[104] http://www.jeolusa.com/PRODUCTS/ElectronOptics/TransmissionElectronMicroscopes(TEM)/200kV/JEM2100LaB6/tabid/207/Default.aspx (last accessed 23-12-13)

[105] http://www.globalsino.com/micro/1/micro9999.html (last accessed 23-12-13)

[106] http://web.pdx.edu/~jiaoj/phy451/Lect6.pdf (last accessed 23-12-13)

[107] http://micron.ucr.edu/public/manuals/EDS-intro.pdf (last accessed 23-12-13)

[108] http://w3.salemstate.edu/~pkelly/sem/ (last accessed 23-12-13)

[109] http://www.eaglabs.com/mc/thermogravimetric-differential-thermal-analysis.html (last accessed 23-12-13)

[110] S. R. Sandler, W. Karo, J. Bonesteel, E. M. Pearce, Polymer Synthesis and Characterization: A Laboratory Manual, Academic press, USA, 1998.

[111] http://www.globalspec.com/reference/36940/203279/chapter-3-thermogravimetry-tg (last accessed 23-12-13)

References

[112] https://sites.google.com/site/mate453mse553tgalab/background (last accessed 23-12-13)

[113] http://share.pdfonline.com/ed99e69c7eaa4a16bc2b3c5951f73a24/tga.htm (last accessed 23-12-13)

[114] http://web.abo.fi/instut/biofuelsGS-2/kursen/%C3%85A/lectures/Lectrure_Thermal%20Analysis.pdf (last accessed 23-12-13)

[115] http://www.shimadzu.com/an/thermal/dtg60.html (last accessed 23-12-13)

[116] R. M. Silverstein, F. X. Webster, D. J. Kiemle, Spectrometric identification of organic compounds, Seventh edition, John Wiley & Sons, USA, 2005

[117] http://orgchem.colorado.edu/Spectroscopy/irtutor/IRtheory.pdf (last accessed 23-12-13)

[118] B. Stuart, Infrared Spectroscopy: Fundamentals and Applications, John Wiley & Sons, Ltd, 2004.

[119] D. L. Pavia, G. M. Lampman, G. S. Kriz, J. R. Vyvyan, Infrared spectroscopy in Introduction to spectroscopy, Fourth edition, Cengage Learning, USA, 2009.

[120] http://chemwiki.ucdavis.edu/Physical_Chemistry/Spectroscopy/Vibrational_Spectroscopy/Infrared_Spectroscopy/How_an_FTIR_Spectrometer_Operates (last accessed 23-12-13)

[121] http://gato-docs.its.txstate.edu/cos-department-of-physics/manuals/VSM/vsm.pdf (last accessed 23-12-13)

[122] E. du Trémolet de Lacheisserie, D. Gignoux, M. Schlenker, Magnetism: Materials and Applications, Springer Science + Business media, Inc, USA, 2005.

[123] http://www.magnetomachinery.com/vibration-sample-magnetometer.htm (last accessed 23-12-13)

[124] http://www.aleralabs.com/Latest/cell-death-assays-for-drug-discovery-part-3.html (last accessed 23-12-13)

[125] A. A. Thant, S. Srimala, P. Kaung, M. Itoh, O. Radzali, M. N. Ahmad Fauzi, J. Aust. Ceram. Soc., 46(1) (2010) 11-14.

[126] D. Wyrzykowski, E. Hebanowska, G. N. Wiczk, M. Makowski, L. Chmurzynski, J. Therm. Anal. Calorim. 104 (2011) 731–735.

References

[127] J. Sengupta, R. K. Sahoob K. K. Bardhana, C. D. Mukherjee, Mater. Lett. 65 (2011) 2572–2574.

[128] E. V. Groman, J. M. Lewis, L. Josephson, European Patent EP 0275 285 B1 (1996).

[129] http://scholar.lib.vt.edu/theses/available/etd-04262006-+181958/unrestricted/AppendixA.pdf (last accessed 23-12-13)

[130] A. P. Khandhar, R. M. Ferguson, J. A. Simon, K. M. Krishnan, J. Biomed. Mater. Res. Part A 100A (2012) 728-737.

[131] A. Singh, F. Dilnawaz, S. K. Sahoo, Plos one 6 (2011) 1-18.

[132] C. Janko, S. Dürr, L. E. Munoz, S. Lyer, R. Chaurio, R. Tietze, S. von Löhneysen, C. Schorn, M. Herrmann, C. Alexiou, Int. J. Mol. Sci. 14 (2013) 7341-7355.

[133] K. M. Krishnan, R. M. Ferguson, A. P. Khandhar, U. S. Patent No. 20130149539 A1 (2013).

[134] https://statistics.laerd.com/calculators/dependent-t-test-paired-samples-calculator.php (last accessed 23-12-13)

[135] M. Mahmoudi, S. Sant, B. Wang, S. Laurent, T. Sen, Adv. Drug Deliv. Rev. 63 (2011) 24-46.

[136] F. Gozuak, Y. Koseoglu, A. Baykal, H. Kavas, J. Magn. Magn. Mater. 321 (2009) 2170–2177.

[137] L. Kou, H. He, C. Gao, Nano-Micro Lett. 2(3) (2010) 177-183.

[138] L. Zampori, G. Dotelli, P. G. Stampino, C. Cristiani, F. Zorzi, E. Finocchio, Appl. Clay Sci. 59-60 (2012) 140-147.

[139] J. Dutta, Am. J. Chem. 2(2) (2012) 6-11.

[140] G. Davidson, Spectroscopic Properties of Inorganic and Organometallic Compounds, The royal society of chemistry, 2006.

[141] J. McMurry, Organic chemistry with biological applications, Cengage learning, Inc., 2010.

[142] W. C. Laia, W. B. Liau, Polym. 44 (2003) 8103–8109.

[143] J. Popplewell, L. Sakhnini, J. Magn. Magn. Mater. 149 (1995) 72-78.

[144] R. W. Chantrell, J. Popplewell and S. W. Charles, IEEE Trans. Magn. 14 (5) (1978) 975-977.

References

[145] D. K. Kim, Y. Zhang, W. Voit, K. V. Rao, M. Muhammed, J. Magn. Magn. Mater. 225 (2001) 30-36.

[146] Y. Wang, X. Peng, J. Shi, X. Tang, J. Jiang, W. Liu, Nanoscale Res. Lett. 7:86 (2012) 1-13.

[147] L. Zhao, H. Zhang, Y. Xing, S. Song, S. Yu, W. Shi, X. Guo, J. Yang, Y. Lei, F. Cao, J. Solid State Chem. 181 (2008) 245–252.

[148] L. T. Zhuravlev, Colloids Surf. A Physicochem. Eng. Asp. 173 (2008) 1–38.

[149] L. G. Schultz, Clays Clay Miner. 17 (1969) 115-149.

[150] R. Bywalez, H. Karacuban, H. Nienhaus, C. Schulz, H. Wiggers, Nanoscale Res. Lett. 7:76 (2012) 1- 7.

[151] A. Saric S. Music, K. Nomura, S. Popovic, J. Mol. Struct. 480-481 (1999) 633-636.

[152] S. I Dezawa, Y. Tamai, U. S. Patent No. 4016057 (1977).

[153] H. Ramadan, T. Coradin, S. Masse, H. El-Rassy, Silicon 3 (2011) 63–75.

[154] A. Narita, K. Naka, Y. Chujo, Colloids Surf. A Physicochem. Eng. Asp. 336 (2009) 46–56.

[155] J. Ye, B. Van de Broek, R. De Palma,W. Libaers, K. Clays,W. Van Roy, G. Borghs, G. Maes, Colloids Surf. A: Physicochem. Eng. Asp. 322 (2008) 225–233.

[156] K. Lee, A. N. Sathyagal, A. V. McCormick , Colloids Surf. A: Physicochem. Eng. Asp. 144 (1998) 115–125.

[157] X. D. Wang, Z. X. Shen, T. Sang, X. B. Cheng, M. F. Li, L. Y. Chen, Z. S. Wang, J. Colloid Interface Sci. 341 (2010) 23–29.

[158] A. Poddar, R. N. Bhowmik, A. De, P. Sen, J. Magn. Magn. Mater. 321 (2009) 2015-2020.